Dissertation

Quantum Dot Clusters as Single-molecules: Deciphering Collective Fluorescence and Energy Transfer Signatures

Submitted by

Duncan P. Ryan

Department of Physics

In partial fulfillment of the requirements

For the Degree of Doctor of Philosophy

Colorado State University

Fort Collins, Colorado

Fall 2016

Doctoral Committee:

Advisor: Martin P. Gelfand
Co-Advisor: Alan Van Orden

Jacob L. Roberts
Amy L. Prieto

Abstract

Quantum Dot Clusters as Single-molecules: Deciphering Collective Fluorescence and Energy Transfer Signatures

Applications of quantum dot nanocrystals span from the individual single-molecule use to large, densely-packed bulk solids. Already, the fluorescence behavior of individual particles is complex and nuanced, particularly involving the blinking phenomenon. When particles are combined into higher-order structures where interaction may occur, a complete description becomes intractable. However, clusters—between two and ten particles—can be effective model systems to explore the local behaviors that occur in larger networks. A benefit of small clusters is the viability of using single-molecule spectroscopic techniques, which are often more informative than bulk measurements. In this work we combine fluorescence microscopy with structure-probing electron microscopy to elucidate the fluorescence dynamics clusters of semiconductor nanocrystals. The spectral characteristics of clusters are explored in the context of an energy transfer model showing low-intensity emission is blue-shifted, corresponding to the weaker emission from donor particles with a larger band gap. Because energy transfer depends intimately on the specific topographical structure of the cluster, the inter-particle spacing, and relative alignment, characterization of specific cluster behavior is better informed by correlated measurements. Next, we present the mapping results from super-resolution microscopy where the spatial distributions of fluorescence in the sub-10 nanometer realm is clearly correlated with scanning electron microscopy imaging of the same clusters. Stochastic blinking events enable such observations. The enhanced blinking associated with energy transfer has practical implications for donor and acceptor roles in clusters. Finally, the dynamic evolution of the emission dipole orientation for single nanocrystals and

nanocrystal clusters is measured. The orientation signature suggests coupling strengths and constitutes a first-step towards determining corrections to Förster resonant energy transfer theory involving nanocrystals.

Acknowledgements

Many people throughout my graduate career deserve special thanks and recognition for the support they provided over the years. My mother, Marie-Laure, and sister, Caitlin, have been the greatest sources of praise, admiration, criticism, and joy in my life since well before graduate school, constantly providing needed perspective on both academics and life. My climbing partners—especially Neil Wachowski, Matt Heine, and Douglas Shepherd—have been there to create the exhausting and fulfilling moments on top of high peaks, and to each one I owe a great deal of gratitude for keeping me balanced. Douglas Shepherd has been an enduring friend and mentor whom I cannot thank enough for pushing me on so many aspects of graduate life. The members of the Van Orden group, particularly Kevin Whitcomb and Farshad Adbollah-Nia, have been there to correct my path when I got lost in the trees of my research. Alan Van Orden took me under his wing and gave me the freedom to explore without bounds and provided the perfect atmosphere for me to grow as a researcher. Martin Gelfand took especially keen interest in my progress, understanding during the times my work regressed, and finally providing the needed suggestions to move forward again. The other members of my committee, Jacob Roberts and Amy Prieto, have been instrumental in so many key decisions in my graduate career and providing supportive conversations. Roy Geiss provided TEM imaging and the thoughtful observations about the samples. None of this work would have been possible without Peter Goodwin and Chris Sheehan, who, in addition to being wonderful collaborators, worked hard and gave their valuable time to assist with many experiments.

Finally, I would not be the person or scientist I am without my dad, who may not have watched me throughout the process, but was my inspiration at every step.

Dedication

To my father, Philip W. Ryan

Table of Contents

List of Tables

List of Figures

CHAPTER 1

Introduction

Semiconductor nanocrystals (NCs) are unique particles that are attractive for many scientific and commercial uses because of their optical properties and small size. Manufacturing simplicity, fluorescence tunability and stability, and high single-particle quantum yeilds (QYs) have propelled the adoption of NCs into devices from photovoltaics to display technologies. As research tools, NCs enable the measurement of features smaller than conventional microscopy can achieve.

Applications of NCs generally fall into two categories: single-molecule and bulk. NCs as single-molecules are treated as point-like emitters that act in isolation or as sensors of their immediate environment. The behaviors of individual emitters report information unique to a specific location, such as the absolution position of the particle to very high precision, or the proximity of the emitter to objects that may interact with it and effect altered dynamics from the particle. Because of their small size and limited sphere of interaction, on the order of a few to tens of nanometers, NCs are ideal probes for measurements below the resolution limit of light. A variety of experimental techniques, collectively referred to by the term single-molecule spectroscopy, are specifically designed to be sensitive to the small signals that are produced by individual emitters such as NCs.

Bulk use of NCs is intended to take advantage of large quantities of particles to amplify their individual properties. For example, films of NCs are used to enhance the collection characteristics of the particles over large areas, and concentrated solutions of NCs generate bright emission that is easily detected without sensitive devices. However, in bulk systems, hundreds to billions of NCs participate and individual behavior cannot be sorted out from

the background signals to which the other particles contribute. While individual interactions between NCs may occur in bulk, they cannot be specifically observed because most measurement strategies sample too many NCs simultaneously to show behavior unique to a subset of the particles.

Some collective dynamics are not present unless NCs form into larger groups. Energy transfer (ET), in particular, requires NCs to be in close proximity, typically less than ~ 10 nm. Other electronic interactions between NCs must occur at similar distance scales because of the magnitude of intrinsic dipole moments or the finite extent of wave functions. While bulk samples typically obscure some types of dynamics, the large number of particles creates the conditions for collective behavior. Small clusters of NCs, 2–10 particles, are ideal model systems for the collective dynamics that can occur in bulk. Such limited numbers of participating NCs means that single-molecule approaches can be used to examine the dynamics without generating signals that merely represent averaged effects. From this perspective, clusters can be prepared and separated to such low densities that signals from individual clusters can be measured and the clusters may be treated experimentally as pseudo single-molecules.

Understanding how energy moves within larger systems is important for engineering devices with specific purposes. NC-based LEDs, photosensors, and photovoltaics have different energy transport requirements than lasers which make use of NCs as gain material, or NCs that tag specific bio-structures, both of which generally aim to suppress transport. NC photoexcitation generates an exciton—an electron-hole pair. Two types of transport may occur for the exciton: (1) the electron and hole may dissociate and diffuse independently in the material, often aided by external electric fields, or (2) the exciton as a whole may transfer to neighboring NCs via an ET mechanism like Förster resonant energy transfer. Energy

transfer pathways can exist for clusters as small as dimers, and as the number of NCs in a cluster increases, so too does the complexity of pathways. Suppression or enhancement of either energy transport form may be accomplished by engineering the local environment of the NCs or the method of contact.

A variety of higher-order structures can be formed using NCs as fundamental building blocks. Linked or attached dimers[1], wire-like "chains"[2–5], aggregates[6, 7], ordered arrays[8, 9], monolayers[10, 11], and films[12–15] are common structures. These higher-ordered formations can also place NCs in such close proximity that interaction between neighboring NCs occurs, resulting in collective behavior, such as enhanced blinking[16].

While fluorescence is an indicator of collective dynamics in higher-ordered NC structures like clusters, it typically cannot provide specific information about the structure. Independent structural measurements can be provided by electron microscopy (EM). Experiments that correlate fluorescence behavior with nanoscale structure have hitherto been focused on single NCs to study their crystalline characteristics[17–20]. However, EM methods can also be used to obtain topographical information about NC clusters and provide context for fluorescence measurements about the possible ET pathways.

The following chapters are an extensive interrogation of CdSe/ZnS NCs and clusters using fluorescence microscopy and EM imaging. EM characterization of clusters uncover orientation factors that are typically overlooked, yet have important ET implications for higher-order structures. Single-molecule confocal studies of the clusters expand on previous works[21, 22] to measure the spectral dynamics of clusters and show that collective behavior beyond enhanced blinking is present. Towards of the goal of identifying ET pathways, super-resolution microscopy correlated with EM imaging is used to match the structure implied by fluorescence measurements with the true geometry of specific clusters and applied to

determine individual donor/acceptor roles in the clusters. Finally, extending super-resolution techniques to extract orientation information provides a measure of an important parameter in determining ET coupling efficiency and demonstration of such measurements is given.

This dissertation is structured to (1) provide background information about NCs and the current state of the field, Chapter 2, (2) detail the various investigative techniques and methodologies used to study NCs, Chapter 3 through Chapter 4, and finally (3) present new work that extends the understanding of NC behavior in clusters, Chapter 5 through Chapter 7. Additional details about the sample preparation methods, excitation calculations, and super-resolution artifacts are provided in Appendix A through Appendix D. A full list of the abbreviations used throughout is given in Figure D.

CHAPTER 2

Quantum Dot Nanocrystals

A unique category of nano-sized particles, colloidal semiconductor nanocrystals, or quantum dots, exploit the properties of bulk semiconductor materials, such as band gaps in the optical wavelengths, to produce stable fluorescent particles with high QYs and strong absorption across a broad color spectrum. Due to the finite size of the semiconductor material, confinement of excitons (an electron-hole pair) to distances smaller than the Bohr radius results in a size-dependent emission wavelength that differs from that of the bulk material band gap. Control over the size during synthesis allows fine-tuning the emission wavelength. The phenomenon of fluorescence intermittency, mechanistically different from the triplet blinking of fluorphors (dyes and proteins), gives these particles dynamic fluorescence behavior. NCs can also form higher-order structures where energy transfer is possible, further affecting the emission characteristics of the particles.

Presented in this chapter are some of the fundamental properties and characteristics of NCs that affect fluorescence and energy transfer. Section 2.1 and Section 2.2 describe the fluorescence of single NCs and the current state of the field explaining fluorescence intermittency. New analysis of blinking statistics using change-point detection is briefly given. Section 2.3 describes the basic synthesis process of constructing the higher-order structures of NCs used to form clusters in this work. Finally, Section 2.4 summarizes the mechanisms that have been used in literature to describe energy transfer between NCs in higher-order structures.

2.1. General Characterization

2.1.1. Physical Structure. The term quantum dot generalizes many types of quasi-spherical nano-sized particles. This work focuses on colloidal semiconductor nanocrystals, many realizations of which fall under the category of quantum dots. Fundamentally, quantum dot NCs are a core of crystalline semiconductor material with a diameter in the 0.5–10 nm range. Common core materials include CdSe, CdS, Si, InP, PbSe, and PbS. Charge carriers in these materials experience the periodic electrostatic fields of the atoms arranged in a regular crystal lattice. However, the material occupies a finite space, leading to confinement effects. The periodic potentials give rise to band structures as solid state theory describes, but the finite extent of the material influences the energies of the bands conceptually similar to a particle-in-a-box, where allowable energy solutions are inversely related to the volume of the confinement region.

The exciton Bohr radius provides a measure of the scaling to compare confinement effects:

$$a_0 = \frac{\hbar^2 \epsilon}{e^2} \left(\frac{1}{m_e^*} + \frac{1}{m_h^*} \right)$$

where m_e^* and m_h^* are the effective masses of the electron and hole in the semiconductor material, respectively, ϵ is the bulk optical dielectric constant, $\hbar$ is the reduced Plank constant, and e the charge of the electron. The exciton Bohr radius represents the average physical separation of an electron-hole pair. Strong confinement is the situation where the physical extent of the semiconductor material is smaller than the exciton Bohr radius and the size of the NC greatly influences resulting the band gap. Smaller NCs will have larger band gaps with bluer emission compared to larger NCs because of the confinement. Weak confinement occurs when the NC size is comparable to or larger than the exciton Bohr radius, and the

band gap resembles that of the bulk material. Interestingly, materials with larger bulk band gaps have smaller exciton Bohr radii: 0.26 eV/46 nm for PdSe, 1.75 eV/4.9 nm for CdSe, and 3.7 eV/1.5 nm for ZnS.

It is common to have a core/shell structure where an outer coating of different semiconductor material (such as CdSe, CdS, or ZnS) is grown around a NC. The main advantages of engineering these structures are (1) to control the distributions and overlap of the electron and hole wave functions and (2) to provide a sacrificial layer to oxidation that maintains the fluorescence properties of the core. Depending on the dispersion relations of each material, the conduction band and valance band at the core/shell interface can take two forms. Type-I core/shell heterostructures confine both the electron and hole to the same region, either the core or shell, because the energy change across the interface is in opposite directions between the conduction and valance bands (see Figure 2.1B). On the other hand, type-II structures localize the electron and hole to different regions, resulting in a smaller overlap between the wave functions, which has ramifications on recombination dynamics. In addition to the band structure, the interface between the core and shell can take on several forms: sharp transition, thin transition shell followed by the final shell, and alloyed[23]. While each of these interface types slightly modify the band structure, their use is typically to release lattice strain generated by the dissimilar lattice constants of the heterojunction materials. Lattice strain can create trap states and at the core/shell interface such traps can be particularly undesirable. Larger NC structures including core/shell/shell have also been created in attempts to control the electron and hole localizations for specific applications.

Ligands are the final component of a NC and are attached at the outer surface, the selection of which depends on a variety of design features[24]. They can be attached to core-only NCs or core/shell structures. The ligand type may be chosen to make NCs soluble

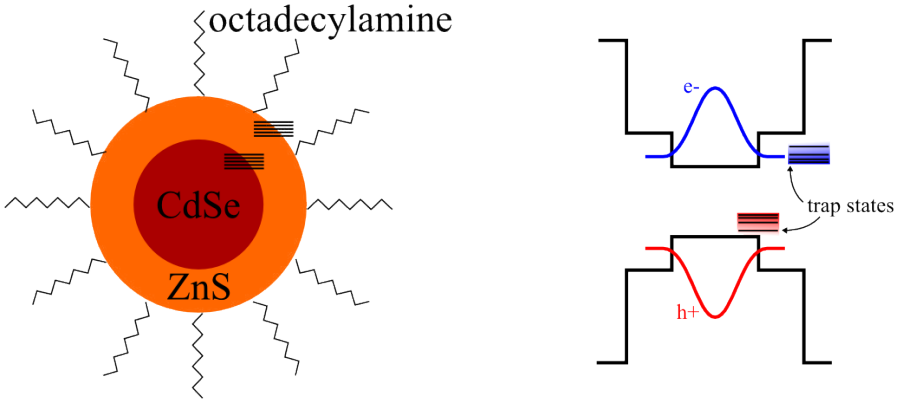

(A) Structure (B) Energy-levels

FIGURE 2.1. Structure of a CdSe/ZnS core/shell NC and the energy level diagram for such a system.

in a particular solvent to enable a desired processing method, or selected to engineer larger or smaller separation distances between particles in bulk solids or films. Some ligands can also be used to inject specific charges into the NCs, depending on which atoms they bond to on the surface[25]. Futhermore, ligands are dynamic, desorbing and attaching to the surface of NCs when in high enough concentration in the suspension solution[25, 26]. The octadecylamine ligands of the NCs used in this work are known to be L-type and are strong displacers of other ligand types that may be used during synthesis[27].

Figure 2.1 diagrams the structure of the NCs used in this work: CdSe/ZnS core/shell NCs with octadecylamine ligand. The CdSe and ZnS materials ideally have a wurtzite crystalline structure; however, polytypism with zinc-blend crystal structure has been reported for CdSe cores[28]. These NCs are type-I heterostructures that confine the electron and hole primarily to the CdSe core. Figure 2.1B suggests a possible arrangement of trap states in such a NC system: located at the core/shell interface and on the surface. Traps are discussed in detail later, owing to the ramifications they have on the fluorescence properties.

2.1.2. Absorption and Emission. The absorption spectrum of NCs is distinctly different from those of fluorophores. While dyes and proteins have relatively narrow absorption peaks, NCs have broad absorption deep into the blue and UV. The absorption, excitation, and emission spectra from a batch of nominally monodisperse CdSe/ZnS NCs at room temperature is shown in Figure 2.2. Various features of the absorption and emission spectra from NCs have been modeled and such methods demonstrate good agreement with measured spectra[29, 30]. The emission spectrum consists of a single peak at 560 nm, just above the $1S_{3/2}$–$1S_e$ transition corresponding to the first absorption peak. Below a local absorption minimum at the $2S_{3/2}$–$1S_e$ transition, the absorption and excitation spectra increase for shorter wavelengths. This behavior makes it efficient to excite a variety of NCs with widely differing emission wavelengths simultaneously and without requiring a specific excitation source for each NC type. The excitation spectrum, measured at the peak emission wavelength, levels off below 500 nm while the overall absorption continues to increase. This feature is due to the fact that higher energy transitions become accessible with lower excitation wavelengths. The two excitation laser lines used in this work are labeled to illustrate that the $1P_{3/2}$–$1P_e$ transition falls between the 488 nm and 450 nm sources. Different fluorescence features appear for these NCs depending on the excitation source and is discussed later.

While a specific batch of NCs can be produced that are nearly monodisperse, a distribution of core sizes is always present and will give rise to a broadening of the bulk emission peak due to particle variability. Furthermore, single NC spectral signatures at room temperature have reported spectral diffusion/drift indicating the emission from a NCs responds to internal or environmental perturbations. These spectral features may occur as sudden emission jumps on the order of 100 meV[31, 32] or as slow, evolving drifts as the NC reacts to its

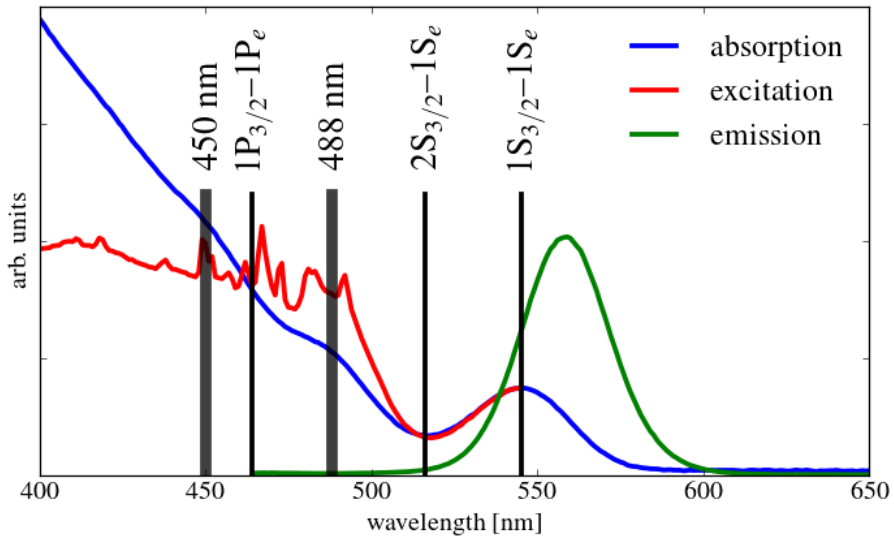

FIGURE 2.2. Absorption, excitation, and emission spectra of 560 nm QDs. The laser excitation lines used in this work are also indicated.

environment[33, 34]. Hence, beneath the single emission feature in Figure 2.2 are nuanced spectral dynamics at both the bulk and individual NC levels.

2.2. FLUORESCENCE INTERMITTENCY—BLINKING

Fluorescent intermittency is a phenomenon that occurs in many NC systems. Often referred to as blinking, it is the random switching of a NC between states of high fluorescence (on) and negligible emission (off). First reported by Nirmal *et al.*[35, 36] at a single-molecule level, blinking has been the focus of many publications about NCs. Additional states with intermediate intensity form a third category, called grey states, that share several characteristics and mechanistic sources as pure on/off blinking.

Figure 2.3 and Figure 2.4 illustrate the appearance of blinking in two different single-molecule measurements. Only under single-molecule investigation does blinking present itself because bulk measurements average over independent blinking events from a large number of emitters. Prominent in Figure 2.3 are the on- and off-states and the sudden

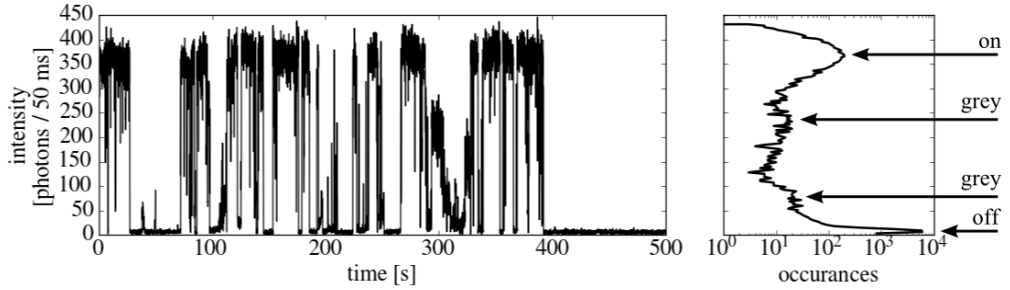

FIGURE 2.3. Fluorescence blinking with 450 nm pulsed excitation.

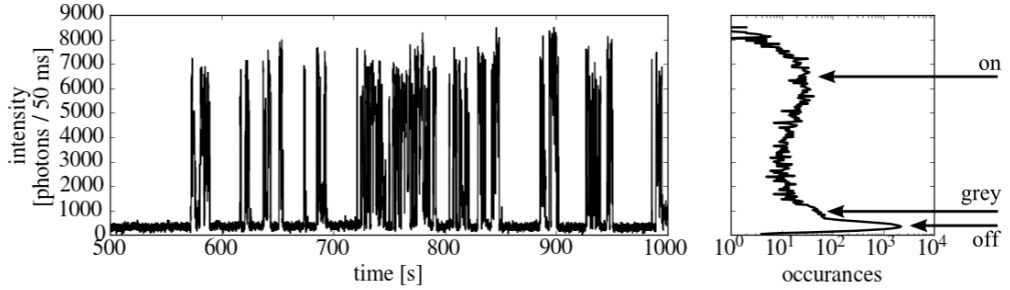

FIGURE 2.4. Fluorescence blinking with 488 nm CW excitation.

transitions between them. Two grey states also appear—well-defined peaks between the on/off intensities in the histogram on the right—with relatively significant intensity levels. Under different experimental conditions, the same batch of NCs may also exhibit the blinking shown in Figure 2.4. While similar in appearance, this fluorescence trajectory is produced with 488 nm excitation and exhibits a less substantial grey state, only slightly above the off-state intensity level. However, even this low QY grey state is distinct from the completely off-state where only detector noise contributes to the signal.

2.2.1. DISTRIBUTION OF EVENT DURATIONS. The duration of an on- or off-state in NCs can span from microseconds, to minutes, and longer. Three types of distributions are

commonly used to describe these durations:

$$P(\tau) \propto e^{-\tau/\tau_c} \qquad \text{exponential}$$

$$P(\tau) \propto \tau^{-\alpha} \qquad \text{power-law}$$

$$P(\tau) \propto \tau^{-\alpha} e^{-\tau/\tau_c} \qquad \text{truncated power-law.}$$

Exponential distributions typically apply to single trap states or triplet blinking in organic fluorophors. Power-law is usually the best model for off-duration distributions in semiconductor NCs and the truncated power-law for the on-durations. The blinking statistics for a single NC are shown in Figure 2.5 and Table 2.1 summarizes the parameters α and τ_c for sixteen NCs from the same batch. The parameters are consistent with other reports for the same CdSe/ZnS NC system[37–40]. The work of Sher *et al.*[41] interestingly connects the long lifetime decay dynamics of time-resolved measurements to the distribution of off-durations by accounting for the relative detection efficiencies, and demonstrates that power-law behavior holds over the extended range from nanoseconds to minutes with a fixed distribution exponent[42]. However, other analysis approaches challenge the power-law distribution altogether[43]. Numerous studies have investigated the dependencies of the distribution type and parameters on NC composition, shell thickness[40], ligands[44, 45], temperature[46], environment[47–49], excitation conditions[50, 51], and selection of analysis modes[38, 52, 53]. While a full description of the trends is beyond the scope of this chapter, discrepancies introduced through analysis methods are particularly unfortunate and worth further discussion. Amecke *et al.* undertook a robust analysis of the binning and thresholding method and concluded that the the choices of thresholds often found in the literature

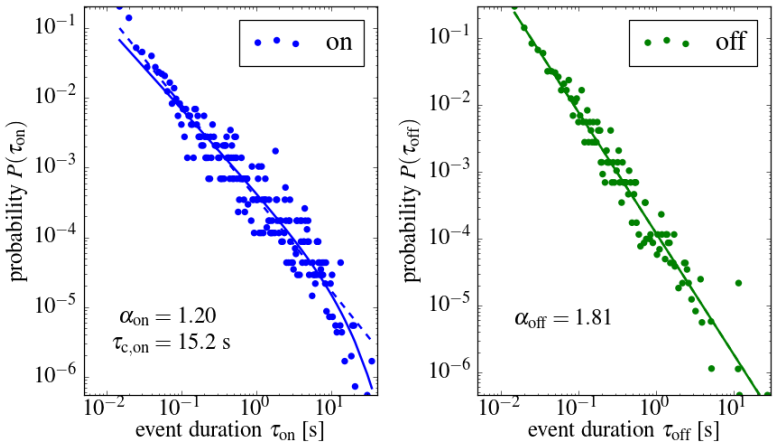

(A) Binning and thresholding

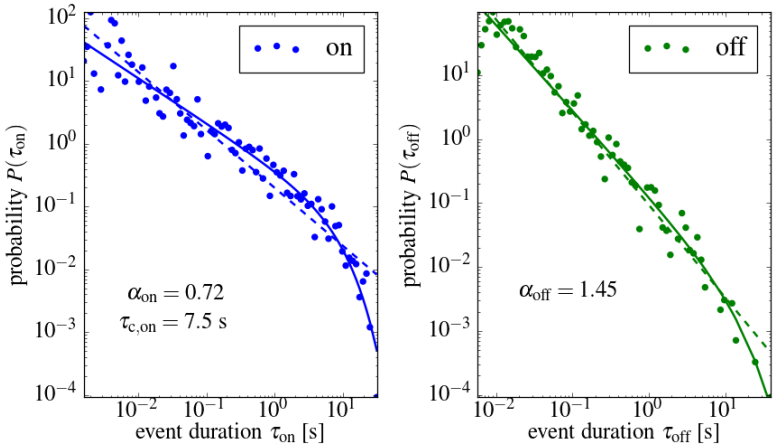

(B) Change-point detection

FIGURE 2.5. The on- and off-duration distributions for a single NC from 5 ms binned data (Figure 2.5A) and from change-point detection (Figure 2.5B). Because long durations occur with such low probability in power-law distributions, it is necessary to weight the single occurrences according to the span of the neighboring empty histogram bins[38]. This extends the range of $P(\tau)$ where the roll-off of the truncated power-law is observed. Note that the thresholding approach produces discrete data and CP detection produces nearly-continuous data. Proper analysis should reflect such categorical differences[54].

"renders most of the data especially on *on*-state power law distributions highly questionable." Only when the onset of the underlying power-law statistics is near the experimental binning time can accurate distributions be obtained.

TABLE 2.1. Summary of single NC blinking statistics parameters using the binning and thresholding analysis approach.

	$\bar{\alpha}$	$\bar{\tau_c}$ [s]	range τ_c [s]
$P(\tau_{on})$	1.4(2)	26.5	3–105
$P(\tau_{off})$	1.8(14)		

TABLE 2.2. Summary of single NC blinking statistics parameters using CP analysis. *Only one NC had a large cutoff time τ_c, the others having a narrower range of 1.5–9.3 ns.

	$\bar{\alpha}$	$\bar{\tau_c}$ [s]	range τ_c [s]
$P(\tau_{on})$	0.8(12)	8.6	1.5–49.4*
$P(\tau_{off})$	1.4(10)		

The first step in determining state-duration distributions is separating intensity traces into defined intensity levels, a task that is common to other analyses that may be of interest. This is typically accomplished by setting threshold levels on binned photon streams. The number and location of thresholds as well as the bin width must be selected in some fashion. While logical choices for these analysis parameters exist, approaches that aim to remove selection bias from analysis methods have become increasingly popular. Power-spectrum analysis[55, 56], auto-correlation analysis[56, 57], and change-point detection[58–63] are among the most commonly applied to NC blinking. Power-spectrum analysis calculates the Fourier transform of the fluorescence intensity trace and auto-correlation analysis examines the shape of the correlation curve as well as the Fourier transform of the correlation curve. Both methods use binned data (either the intensity trace or the correlation function) and, more restrictively, do not determine independent distributions for the on- or off-states. Change-point (CP) detection based on inter-photon arrival times performs the task of breaking a fluorescence trajectory into unique intensity levels without binning the data, thresholding, nor specifying the number of levels present by following a likelihood-based approach

that accounts for photon counting statistics[64]. Therefore, multi-level blinking (such as grey states where thresholding may overlap closely-spaced intensity levels) can be accommodated and the distribution of state-durations calculated in a statistically unbiased manner. More recently, change-point detection based on Bayesian inference and hidden Markov models has been the preferred approach to eliminate selection bias from pre-binned data streams (as in the case of data from experiments involving cameras limited by integration time)[60–62]. While power-law blinking does not strictly fall into the category where Markov models apply, progress using explicit state duration (semi-Markov processes)[63] offers a solution that can be utilized for blinking duration distributions and other analyses.

Analyzing the on- and off-duration distributions using inter-photon CP detection on the same photon stream as shown in Figure 2.5A results in the slightly different distributions depicted in Figure 2.5B. Table 2.2 summarizes the distribution parameters using CP results for the same batch of NCs as Table 2.1. Examination of the associated CP time-trace shows excellent reconstruction of the intensity trace—as far as visual inspection, both methods appear to capture the correct transitions. However, the power-law exponents α are smaller for CP than from threshold-based analysis, and an order of magnitude smaller time-scales are identified. These effects are understood by recognizing that the thresholding approach is more likely to register an invalid transition between on/off intensities due to noise. Thus, in thresholding analysis longer durations will be broken into smaller segments by noise, resulting in fewer long events and increased numbers of short events, which favors a larger power-law exponent α and, by the limiting effects of the bin size, does not simply shift the distribution to shorter time scales. Terentyeva *et al.*[65] compared binning and CP methods in enzyme smFRET experiments and found that, for exponential distributions, binning overestimated the number of short durations while CP underestimated. Because the overwhelming majority

of published studies on power-law analysis are based on thresholding, and no study has taken direct aim at the application of CP to blinking statistic, discussion about these discrepancies with CP analysis is lacking. However, while much attention is given to the on-durations, the off-duration exponents from CP are consistent with the $\alpha \sim 1.5$ that Sher *et al.*[41] use to connect the vastly differing time scales of long decay dynamics with the off-duration power-law behavior, and are more consistent with the off-duration statistics from many of the blinking theories.

As pointed out by Kuno *et al.*[37, 38], and reconsidered later by Schmidt *et al.*[59], power-law distributions are well approximated by the sum of only a few exponential distributions with cutoff times distributed between the resolution of the measurement and the length of the measurement. The work of Schmidt *et al.*[59] calculated the decay-time of on-durations from each intensity level identified by CP analysis and observed spikes at specific time-scales. They showed that distributions of these identified decay-times effectively reproduces the power-law distribution for on-durations for the given NC. It is from this perspective that NC blinking statistics are understood to represent a distribution of transition rates, which has led the discussion about the physical mechanisms responsible for fluorescence intermittency.

2.2.2. Blinking Mechanisms. Having discussed the observed manifestations of blinking without directly addressing the mechanisms responsible, we present a summery of the proposed models for fluorescence intermittency. Excellent reviews of blinking have been published by Cichos *et al.*[39], Frantsuzov *et al.*[66], and Cordones and Leone[67], where the interested reader can find more detailed discussions in the context of the experimental findings that led to the proposed models. Theories behind the fluorescent intermittency of NCs are divided into two categories: (1) type-A blinking stems from charging and is accompanied

by a fluorescence lifetime change due to Auger recombination and (2) type-B blinking is the result of fluctuating recombination pathways that do not compete directly with band edge recombination rate such that no lifetime change occurs, only a decrease in fluorescence intensity.

Type-A blinking: A transition from an on-state to an off-state is associated with the capturing of a charge-carrier at a trap site located away from the core of the NC—at the core/shell interface, on the surface of the NC, or even on a ligand or in the local environment[68]. The other charge-carrier from the original exciton remains in the core. Any new excitons participate in three-body interaction due to the presence of the untrapped charge in the core. The Auger effect is responsible for new excitons recombining without producing emission by transferring the energy to the untrapped charge and exciting it to a higher energy level where it can decay back to the band-edge by coupling to phonon modes in the crystal lattice. However, normal radiative recombination can still occur and is a competing process. The resulting reduced fluorescence has a shorter lifetime than the intrinsic lifetime of the excited state due to the presence of the alternative Auger pathway. The transition from an off-state to an on-state is the process of releasing the trapped charge-carrier which returns the core to a neutral state and normal radiative recombination resumes unimpeded by the Auger process. Theories that describe type-A blinking are referred to as charging-models.

A single trap state involves unique, but single trapping and de-trapping rates that result in exponential distributions, not the power-law blinking observed in NCs. Verberk *et al.*[69, 70] introduced the first model to explain power-law arising from a distribution of multiple trap states, each with exponential behavior, that collectively produce power-law distributions and Kuno *et al.*[71] expanded the theoretical framework to accommodate general charging

mechanisms. Other charging theories have been proposed that explain features which are not addressed by the basic charging model. Collectively referred to as diffusion models, these models considered traps to be dynamic, with either fluctuating tunneling widths or barriers heights for a charge-carrier to become trapped[38], or fluctuating trap energies that come into resonance with the band-edge[46, 72, 73].

Type-B blinking: Because type-A models rely on long-lived charged states of the NC—the existence of which has been challenged—and detailed measurements of charged NC QYs are found to be more emissive than the off-state[74, 75], additional models have been proposed that do not attribute an off-state to charging, but rather to processes that open up non-radiative recombination pathways. The Auger-assisted relaxation model of Frantsuzov and Marcus[76] couples spectral drift of the $1S_e$ and $1P_e$ states with deep surface trap states for the hole. As the energy difference between the two levels comes into resonance with deep trap states, the hole trapping rate increases, opening an efficient non-radiative recombination pathway. Fast phonon-assisted de-excitation returns the electron to the $1S_e$ level and non-radiative recombination with the hole occurs on the microsecond time-scale. The spectral diffusion of the $1S_e$ and $1P_e$ levels produces power-law distributions in an analogous manner as the type-A trap state energy diffusion blinking model. More recently, Frantsuzov *et al.*[77] proposed a mechanism that involves multiple recombination centers that transition between active and inactive configurations. The multiple recombination centers theory produces power-law distributions by assigning each site a unique recombination rate and the fluctuating contributions of the individual active centers produces a distribution of rates. Ultimately, the off-state of such models does not compete directly with band-edge recombination and results in low-intensity fluorescence without a lifetime change, which is the defining characteristic of type-B blinking mechanisms.

While a single, all-encompassing model for fluorescence intermittency is desirable, it is likely not the case. The work of Galland *et al.*[78] demonstrated that both type-A and type-B blinking events could be measured and controlled in the same NC; however, every NC has unique affinity for one mechanism over another. In experiments without such exacting control of the NC environment, NCs may express a combination of both blinking types. Evidence for the multiple recombination centers theory has been demonstrated by Volkán-Kacsó *et al.*[79] because NC blinking exhibits memory effects (long blinking events are likely followed by another long event and short events are likely followed by another short event). The Auger-assisted type-B blinking model proposed by Frantsuzov and Marcus also suggests a possible explanation for the difference manifestations of grey states observed in Figure 2.3 and Figure 2.4. Light-induced spectral diffusion of the $1S_e$ and $1P_e$ states may have different behavior when the laser source can excite above both the $1S_e$ and $1P_e$ states versus between the two states.

Trap states are key components in both types of blinking and some details about their origins will inform later discussions about their impact in higher-order structures of NCs. A trap—as the name suggests—is a feature in a NC where a normally free charge-carrier, either an electron or hole, can become localized by the electrostatic environment that presents a local energy minimum to the carrier. Deviations from the ideal regular crystalline structure produce several types of trap states in NCs: at substitution sites in the lattice, at lattice defects arising from polycrystallinity, or along a heterojunction interface (such as between the core and shell) due to lattice mismatch. In addition crystalline sources, traps can occur at the surface interface due to unsaturated bonds, within the passivating ligands, or in the local external environment of the NC. Incomplete ligand passivation on the surface of NCs leaves dangling bonds and exposed atomic sites that can trap charge-carriers. The detailed

worked of Bryant and Jaskolski[80] showed that incomplete passivation of surface anion sites (specifically from S atoms, but applicable to the Se atoms of other common NC compositions) or cation sites (Cd or Zn) introduced a distribution of trap states between the conduction and valance band. Because ligand attachment is dynamic, particularly in solution, and because ligands can diffuse across a NC surface, the exact passivation configuration can change over time and give rise to additional variability in fluorescence intermittency. This also gives a physical interpretation to the diffusion blinking models where there is spectral or barrier motion to trap states. One should not consider NCs to be static objects even after being fixed to a surface.

Traps function fundamentally in different ways between type-A and type-B blinking models but the states arise from the same types of NC features listed previously. In the context of the charging models, a trap state functions as a retainer for one of the charge-carriers and confines the carrier for the duration of an off-period. Where traps are the sites for non-radiative recombination centers (type-B blinking models), charge-carriers do not occupy the sites for more than a few hundred microseconds and an off-event may cycle through many occupations of the traps.

Because of the nature of some traps, appropriate engineering of NCs has been able to eliminate the fluorescence intermittency altogether[81, 82, 23]. Giant-shell NCs suppress blinking by placing trap states far away from the core such that the wave functions of the charge-carriers have little spatial overlap with the traps. This approach requires a type-I heterojunction between the core and shell. Controlled, monolayer growth of the semiconductor crystals produces few lattice defects and alloying the core/shell interface with epitaxial growth results in a gradient that relieves lattice strain. However, complete suppression of

the blinking may not always be desired, as in the case of elucidating some of the information presented in this work.

With a more complete understanding of the sources of fluorescence intermittency, a brief return to the discussion of grey states is in order. As pointed out by Zhao *et al.*[75], the off-intensity is a full order of magnitude less than the biexciton QY. Charged NCs used in type-A blinking models—a trion versus a biexciton—would present a distinguishable intermediate intensity level. The work of Yoshinkawa *et al.*[83] addresses these intermediate intensity levels in greater detail to conclude that biexciton generation is a step along the pathway to produce the trion state. The implications of measuring grey states is twofold: (1) type-A charging models are valid and should not be dismissed, and (2) multi-level blinking occurs and may factor into interpreting blinking measurements.

2.3. Higher-order Structures: Clusters

Many applications of NCs do not make use of single particles in isolation, but as units of larger systems. Attached to other molecules as signaling agents or as part of large collections of NCs, various arrangements tailor the unique properties and behaviors of NCs to the benefit of a desired task or measurement. In this work, the interactions between attached NCs are investigated in small NC clusters.

Even in the narrow context of higher-order structures involving only NCs of the same type, a variety of different cluster constructions can be formed. Dimers and trimers are the smallest units and have been synthesized with direct physical contact between the NCs, and with linker molecules to produce separation gaps[1]. Wire-like chains have been formed in several systems, including CdTe[2], CdSe[4], and PbSe NCs[3, 5]. These chains are typically core-only systems and the synthesis process involves attachment of initially isolated NCs that

function as building blocks. Electrostatic dipole-dipole interactions between the NCs cause oriented attachment such that the c-axis the crystal lattice from each NC aligns along the length of the chains, and TEM imaging shows long range lattice continuity. Aggregates[6, 7] and ordered arrays[8, 9] involve tens to hundreds of NCs, with ever larger structures eventually entering the size-scale of monolayers[10, 11] and NC films[12–15]. Inter-particle separation distances in each of these higher-order structures can be small enough that strong electronic coupling occurs and collective behaviors arise.

This work focuses on small, physically attached clusters that serve as model systems for the local interactions which occur in larger structures. Collective behavior begins with dimers and becomes more complex in larger higher-order structures.

2.3.1. Synthesis Methods. Two synthesis approaches are applied here to form clusters from initially isolated and unattached NCs: (1) slow clustering at low concentrations, and (2) rapid clustering at high concentrations. The mechanisms of attachment at the single particle level are not well understood and producing clusters from substantially different processing methods provides a means of exploring the processes. Details of the two approaches with discussions are found in Appendix A.

The slow clustering approach has been used in previous studies[16, 84, 21, 85, 22]. The procedure, briefly, involves adding a small amount of MeOH (a bad solvent) to a dilute solution of NCs in toluene. After letting the clustering process proceed for 10–20 minutes, the clusters are deposited onto their final measurement substrate. The length of time roughly establishes the size scale of the resulting clusters. Fluorescence measurements of these clusters demonstrate collective behavior and indicate interaction occurs among the constituent NCs. Done at nanomolar concentrations that can be directly deposited onto substrates at appropriate emitter densities for single-molecule experiments, this clustering method can

provide the conditions for oriented attachment. However, TEM determination of the true attachment orientations—the most direct measurement of such structural information—is difficult with this approach because the low NC concentrations are not ideal for locating NCs in the limited field of view of the TEM at the necessary magnification to visualize such small particles. Furthermore, the NCs and resultings cluster are too small for AFM characterization of the cluster size and geometry.

Rapid clustering followed by size purification through ultra-centrifugation, as described by Xu *et al.*[1], can produce clusters at higher concentrations and that are stable as clusters for months. Similar to the slow clustering method, MeOH is added to a solution of individual NCs that precipitates the particles out of solution. However, the NC solution is in the μM–mM concentration range and a significantly larger amount of MeOH is added which results in a turbid mixture. This mixture is then separated from the MeOH by traditional centrifugation, resuspended, and purified through a series of ultra-centrifugation cycles. At such high concentrations, TEM imaging can be easily done. Figure 2.6 show the distribution of cluster sizes and geometries that are produced by this method.

Despite the effective size selection that Xu *et al.*[1] were able to achieve with fine-tuning the separation procedure, the selection of clusters produced in this work were broadly distributed. The results from three sequential separation runs are shown in Figure 2.7. Ideally, clear, well separated bands constituting single cluster sizes appear after separation. However, such clear bands were not observed after the first purification (Figure 2.7A), and further purification of each region separately resulted in only minor improvement of the banding (Figure 2.7B & Figure 2.7C). However, the final top, middle, and bottom regions did primarily contain singles, small clusters, and large clusters, respectively.

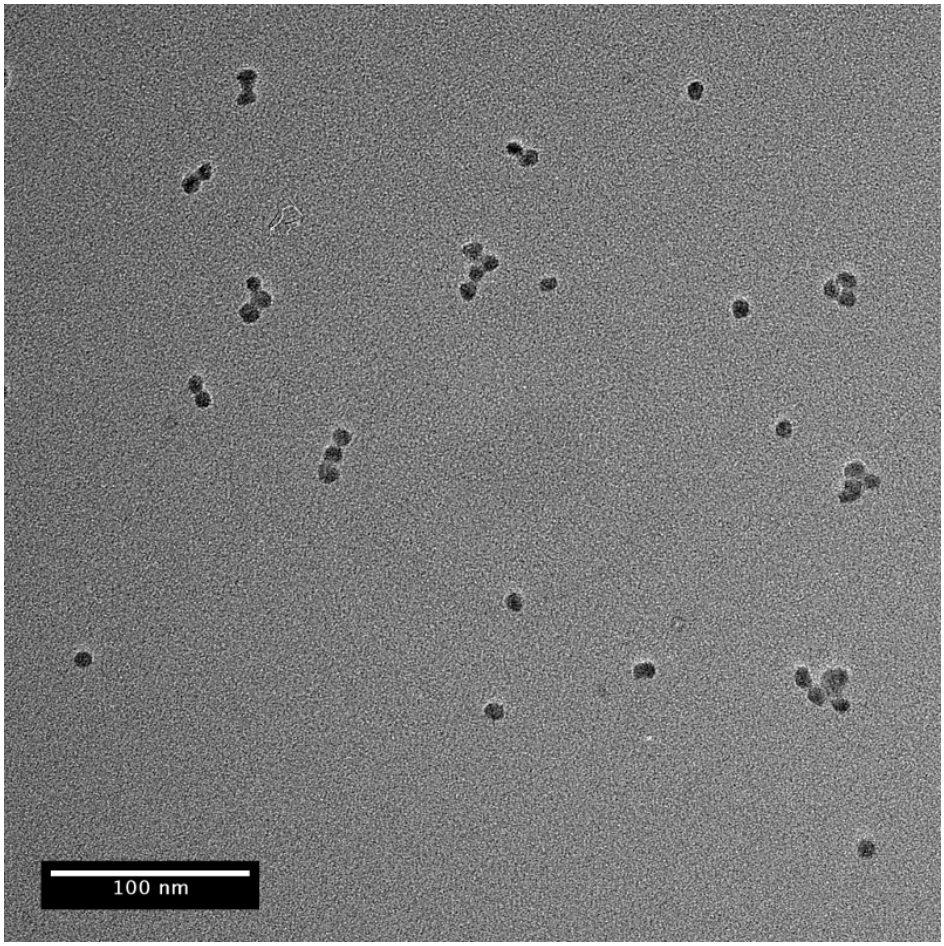

FIGURE 2.6. Distribution of cluster sizes and shapes after UC, imaged by TEM.

There is a variety of minutia associated with the centrifuge process that can affect the end results (see Appendix A for a full discussion). The initial distribution of cluster sizes, the NC concentration, and separation layer thickness can all impact the efficacy of the separation process. In particular, the initial distribution from the clustering step could be narrowed by using fewer crash cycles (three were used here), and is likely the best procedure to improve to obtain narrower size-selection. Using a less aggressive bad-solvent, such as acetone, will also produce clearer banding and, hence, a narrower size distribution (see Figure A.1).

Ultimately, both the slow and rapid clustering methods produced similar clusters. However, only the rapid clustering could be more completely characterized by TEM. Trimers are the smallest higher-order structures that can have different geometries: linear chains, angled

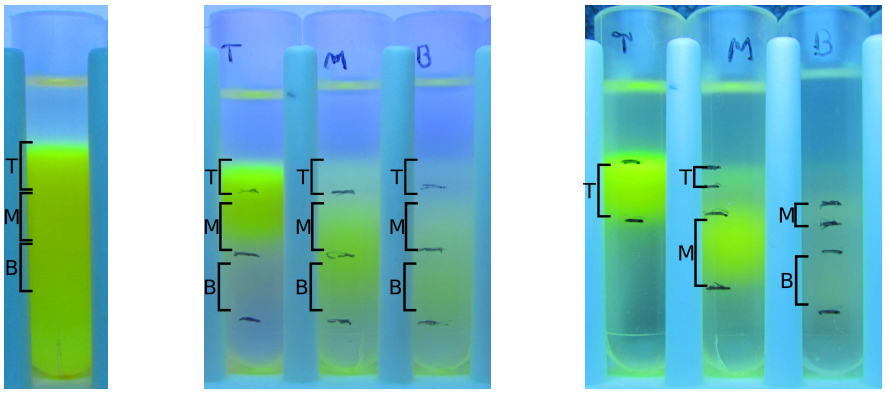

(A) First UC (B) Second UC (C) Third UC

FIGURE 2.7. Ultra-centrifuge separation. The density of the NCs is sufficiently high that the bands can be observed under UV-illumination. Batches were collected from the top (T), middle (M), and bottom (B) of each centrifuge tube. Samples collected from like regions of each tube were combined and dried together for subsequent ultra-centrifugation cycles.

chains, and compact pyramids. Larger clusters can take on an even larger variety of shapes and many unique realizations of geometry were observed. The two clustering methods were indistinguishable from one another in fluorescence measurements, although this does not necessarily rule out oriented attachment in the slow clustering approach.

2.3.2. ENHANCED BLINKING. The effect of collective effects from NC interactions is readily observed in the fluorescence trajectories of clusters formed by either the slow or rapid clustering procedures. Figure 2.8 illustrates what is termed enhanced blinking: rapid intensity fluctuations across a distribution of intensity levels. Quantitative characterization of the rapid fluctuations from enhanced blinking was reported in the autocorrelation study of Shepherd *et al.*[84] whereby the roll-off time of the intensity autocorrelation function occurs at shorter times for clusters than for single NCs. The work demonstrated in simulations that the roll-off time decreases as the number of NCs in a cluster increases.

Enhanced blinking is distinct from binary blinking. In the latter, two clearly separated intensity levels can be identified. Grey state blinking presents in a similar fashion, but with

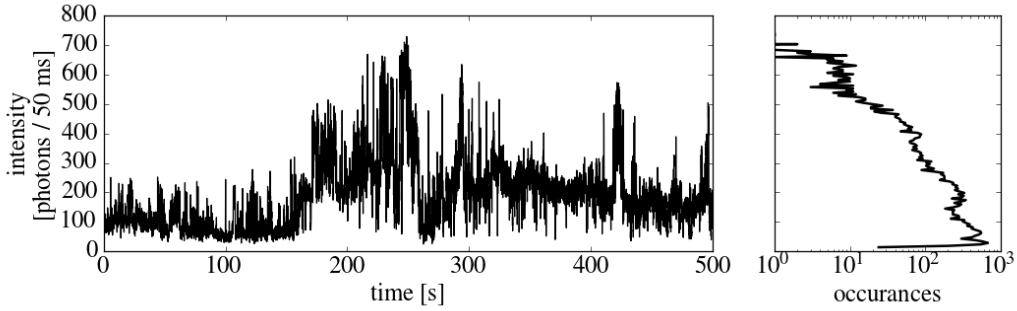

FIGURE 2.8. Example of enhanced blinking.

additional, distinct intensity levels between the on- and off-levels. However, the intensity histogram of enhanced blinking outlines a broad, non-Poisson distribution of intensities. Enhanced blinking is attributed to inter-particle interactions because the intensity trace is distinct from that of multiple NCs blinking independently[16], which would resemble stacked-binary blinking (the superposition of multiple binary blinking trajectories), similar in presentation as grey state blinking where additional levels appear. The work of Tovstun and Razumov[86] have proposed a model to extract ET rates considering NC blinking.

While the blinking of clusters does not divide into convenient on- and off-intensity levels, quantifying intensities as high and low provides a useful analogue to examine blinking statistics. Whitcomb *et al.*[87] proposed this approach and applied it to CdSe/ZnS NC clusters of indeterminate size. The clusters of that study also demonstrated power-law blinking behavior with similar exponent parameters as single NCs. The authors suggest that the similarity to single NCs is due to a single, specific NC within a cluster that is primarily responsible for the emission characteristics because excitons are directed to this acceptor NC through energy transfer.

Figure 2.9 shows the results of such blinking analysis on the clusters used in this work. A smaller cluster, from the middle segment of an ultra-centrifuge purification, Figure 2.9A, shows similar power-law behavior as a larger cluster, Figure 2.9B, from the bottom region.

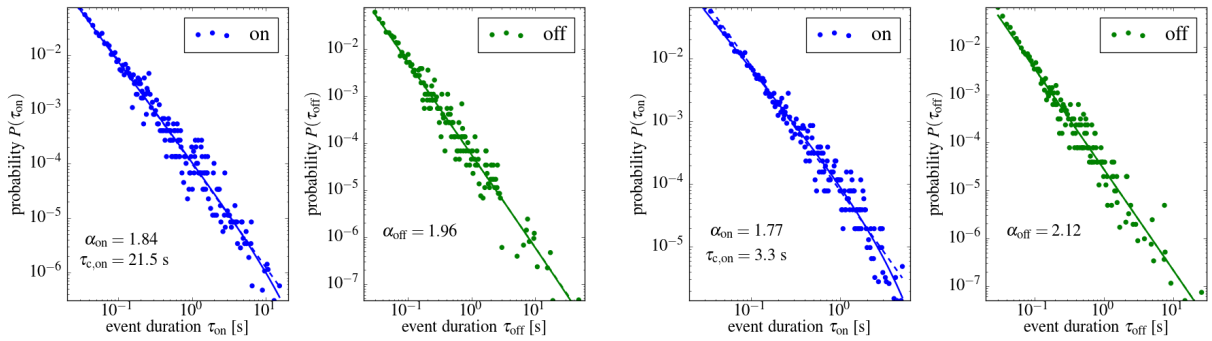

(A) Small cluster (B) Large cluster

FIGURE 2.9. Blinking statistics of a small cluster and a large cluster from 5 ms binned data. The midpoints of the intensity histograms were used as the thresholds to define high- and low-intensities analogously to on- and off-states in binary blinking. Exponent values—particularly for the high-intensity state—are larger than those for single NCs.

The exponent parameters for the clusters in this work were statistically higher than for single NCs of the same synthesis batch for both the on/high- and off/low-distributions. The discrepancy may lie in the different energy transfer efficiencies between the NCs of the two studies. However, blinking statistics for multiple, independent NCs—the closest approximate to NCs with significantly reduced energy transfer—are rarely reported, and pursuing an explanation for such discrepancies is outside the scope of this work. Furthermore, the model selection of truncated power-law over power-law is not as powerful for the high-duration distributions in Figure 2.9 as the on-duration distributions measured earlier for single NCs (Figure 2.5). This suggests additional long rates may be present in clusters and that a broader distribution of individual truncation times from the constituent NCs presents a more strictly power-law behavior.

2.4. Energy Transfer

Most higher-order structures of NCs present the conditions for energy transfer to occur. While dependent on the type of transfer mechanism, the properties that are most relevant to

efficient ET between NCs are proximity and energy level overlap/accessibility. ET can refer to the migration of the individual charge-carriers independent of one another, as is necessary for photo-voltaic applications which aim to collect the separated charges, or the transfer of an entire exciton to neighboring NCs. The former is charge transfer and is typically an engineered process whereby electric fields, either intrinsic or external, drive the transfer, and the charge-carriers diffuse independently. Exciton transfer is the transfer of an electron-hole pair to another NC resulting in an excited state of the acceptor. While both processes can potentially occur in the NC clusters of this work, we focus on the exciton transfer.

Initially reported by Kagan *et al.*[88, 89] in the CdSe system, close packed solids of NCs demonstrated two strong signatures of ET. The emission spectra of monodisperse NC solids were redshifted, indicating emission from the smaller band gap NCs of the sample size distribution. Furthermore, in mixed solids the lifetime and fluorescence of the smaller NCs were quenched while those of the larger NCs were enhanced. Rapid ET in the few nanosecond range was later measured by Crooker *et al.*[90] in gradient layers of mixed-size NCs. Achermann *et al.*[12] further identified three unique lifetime components in monolayers of 4.4 nm diameter CdSe NCs, attributing them to ET to three shells of the nearest- and next nearest-neighboring NCs in the film, and implying that long-range ET can occur.

Förster resonant energy transfer (FRET) is the dominant ET theory applied to NCs[91]. It is fundamentally a dipole-dipole interaction coupling the relaxation of a donor to the excitation of an acceptor in the near-field (exchange of a virtual photon). While not commonly attributed to ET between NCs, Dexter electron transfer (DET) is a similar mechanism (and, in fact, an extension of Förster theory) that considers the effects of dipole-quadrupole coupling[92] and is the exchange of charge-carriers between a donor and acceptor. Where FRET is a singlet-singlet ET, Dexter involves triplet states and depends on the wave function

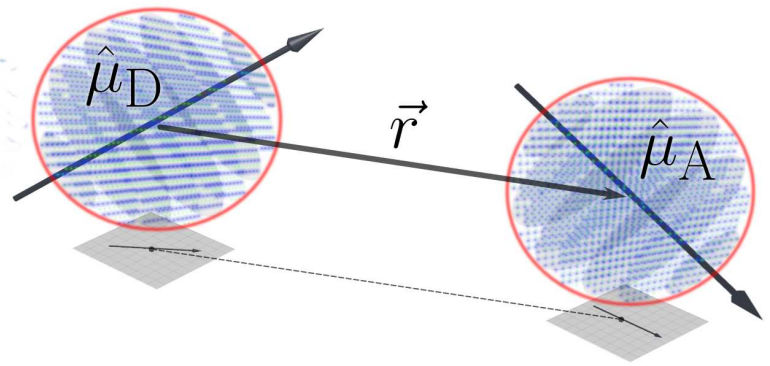

FIGURE 2.10. Calculation of the orientation factor κ for FRET depends on the the separation unit vector $\hat{r}$, and the orientation of the donor and acceptor dipoles, $\hat{\mu}_{\mathrm{D}}$ and $\hat{\mu}_{\mathrm{A}}$.

overlap across the donor and acceptor particles, leading to a stronger distance dependence than FRET.

ET rates for FRET and DET are functionally different, which is emphasized by the distance dependencies of each. The FRET rate is given by

$$k_{\mathrm{FRET}} = \left(\frac{9\eta_{\mathrm{PL}}\kappa^2}{128\pi^5 n^4}\right)\frac{1}{\tau_{\mathrm{D}} r^6}\int \lambda^4 f_{\mathrm{D}}\left(\lambda\right)\epsilon_{\mathrm{A}}\left(\lambda\right)\mathrm{d}\lambda$$

where η_{PL} is the QY of the donor, n is the index of refraction of the surrounding media, τ_{D} is the lifetime of the donor, f_{D} is the normalized donor emission spectrum, ϵ_{A} is the acceptor extinction coefficient, and κ is a factor defining the strength of dipole coupling based on the relative orientations of the emission/excitation dipoles:

$$\kappa = \hat{\mu}_{\mathrm{D}} \cdot \hat{\mu}_{\mathrm{A}} - 3\left(\hat{\mu}_{\mathrm{D}} \cdot \hat{r}\right)\left(\hat{\mu}_{\mathrm{A}} \cdot \hat{r}\right)$$

In this second equation $\hat{\mu}_i$ is the transition dipole moment of each particle and $\hat{r}$ is the unit vector defining the the separation of the donor and acceptor. Figure 2.10 depicts the components of the orientation factor schematically for a donor/acceptor NC pair. Typically the

orientation factor κ^2 is averaged over all orientations and the value of 2/3 is assumed for randomly oriented dipoles in bulk measurements. However, this assumption is not valid in single-molecule measurements, such as individual NC clusters, which have unique donor/acceptor orientations. FRET rates have a $1/r^6$ scaling, which, for the CdSe/ZnS NC system of this work, quickly become negligible at 8–10 nm compared to the fluorescence decay rate.

The DET rate has the functional form

$$k_{\mathrm{DET}} = Ke^{-2r/r^{\circ}} \int \lambda^4 f_{\mathrm{D}}(\lambda)\, \sigma_{\mathrm{A}}(\lambda)\, \mathrm{d}\lambda$$

where r° is the sum of the Van der Waals radii for the donor and acceptor, K is a constant that depends on the orbital interactions (typically experimentally determined for each system), and σ_{A} is the absorption cross section of the acceptor. Note that the integral is similar to that of FRET except FRET involves convolution of the extinction coefficient while DET involves the absorption coefficient. The DET rate has a more rapid falloff because of the dependence on wave function overlap, which is typically limited to a couple nanometers.

A great deal of attention and support is given to FRET in many publications for ET between NCs. NC-NC coupling using the dipole approximation has been shown to be very accurate for 3.9 nm diameter CdSe NCs compared to full density function theory (DFT) calculations and for different orientations of the NCs[93]. However, the recent work of Mork *et al.*[94] measured a discrepancy assuming FRET-only ET theory for exciton diffusion in NC thin-films, and suggested higher-order corrections could reconcile the differences. An experimental investigation comparing the two ET models by Hoffman *et al.*[95] found that in larger core-only CdSe NCs (> 3 nm diameter) FRET was accurate, while DET was dominant for smaller NCs. Hence, Dexter electron transfer may yet have a place in some NC systems.

Both FRET and DET theories were derived for general molecular systems. In addition to the general ET theories that are non-specific to semiconductor NCs, other works have attempted to describe ET effects particular to NC systems[96–98, 93, 99]. From early on it has been known that the fine-structure of the $1S_{3/2}$–$1S_e$ exciton band edge is eight-fold degenerate—three dark states, one linearly polarized bright state (spin 0), and four circularly polarized bright states (doubly-degenerate spin ± 1)—that are obscured by inhomogeneous line broadening[100, 101]. The spin ± 1 states represent a 2D transition plane, oriented perpendicular to the c-axis of a cubic or hexagonal lattice crystal, and the spin 0 state presents an additional 1D transition aligned along the c-axis. Captured in the orientation factor κ of FRET is the assumption that the donor and acceptor are 1D dipoles with defined orientations. The orbital interaction factor K performs an analogous function in DET. Scholes and Andrews[96] developed a quantum electrodynamical treatment of the coupling for two NCs in the dipole approximation with the aim of accounting for the selection rules of NCs, effectively accommodating the 2D + 1D nature of the transition dipole (the 1D transition associated with the spin 0 state has been observed and can contribute depending on the excitation conditions[102]). The resulting ET rate equations are similar to the expression above for FRET and the specific form of the orientation factor becomes:

$$\kappa = \hat{\bar{\mu}}_i^{0\alpha} \left(\delta_{ij} - 3\hat{R}_i \hat{R}_j \right) \hat{\mu}_j^{\beta 0}$$

where α and β refer to the spin state of the donor and acceptor, respectively, and the dipole transition moments are potentially complex—such as the case for transitions involving the circularly polarized states with $\vec{\mu}_{\pm} = (\mu_x \pm i\mu_y)/\sqrt{2}$. The authors point out that a particularly daunting challenge to single-molecule measurements of ET rates is obtaining

the correct spectral overlap integral as this parameter is subject to substantial variability for even the narrowest dispersion of NCs.

Although they are substantially different systems, inter-connected films of NCs used for carrier mobility studies[103] provide insight into the collective effects of clusters beyond the basic donor/acceptor ET perspective. A recent publication by Li *et al.*[104] reported on DFT simulations of linked NC dimers in the context of carrier mobility in inter-connected films. Bridging, where ligands function as linker molecules between NCs, was found to introduce traps due to hybridization of the ligand/NC orbitals and a dipole-induced potential drop. Necking—or fusing—puts the crystal facets of NCs in direct physical contact and did not introduce trap states, leading to higher carrier mobility. Therefore, collective behaviors from NC clusters could benefit from the consideration of carrier-mobility approaches and not solely discrete energy transfer schemes.

CHAPTER 3

Electron Microscopy

Material scientists have a wide range of tools to probe systems of interest. Among them, the electron microscope (EM) images samples with magnifications unapproachable by conventional optical microscopes. The scanning electron microscope (SEM) and transmission electron microscope (TEM), while categorically similar, provide different measurement capabilities for imaging nanoscale structures like NCs. The ability to image objects just a few nanometers in size with high resolution makes EMs ideal characterization tools for NC clusters.

This chapter broadly summarizes the capabilities of SEMs and TEMs, and their modes of operations that are useful for semiconductor NC studies. Section 3.1 outlines the operating principles of the SEM which is used for the correlated studies of Chapter 6. Section 3.2 describes the TEM along with the variety of measurement capabilities that are useful for general characterization of NCs. Finally, Section 3.3 presents specific EM characterization of the samples prepared for this work.

3.1. Scanning Electron Microscope

Of the two types of EMs, SEM is simpler conceptually and in practice. Figure 3.1 depicts the major components: an electron source, a focusing element, the sample, and a detector. The electron gun and lens produce a focused beam of high energy electrons that interact with the sample, producing secondary electrons which are then detected by some rate device such as a scintillator-photomultiplier detector. High resolution images are obtained by raster scanning the 0.5–5 nm diameter focused electron beam across the sample and the intensity of the scattered secondary electrons are mapped to the position of the scanning beam, providing

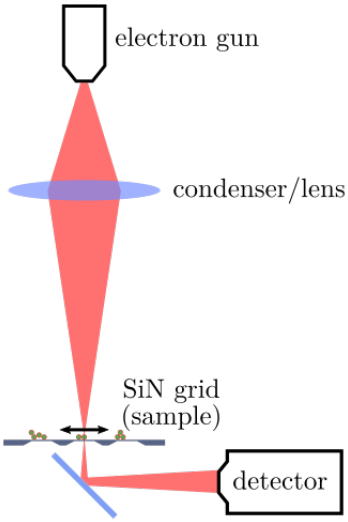

FIGURE 3.1. Principles of operation of STEM-in-SEM.

topographical information. In standard SEM operation, the depth of the interaction volume is small and secondary electrons are detected from the same side of the surface that the primary beam impinges on the sample. Scanning transmission electron microscopy (STEM) is a variant that can be applied to SEM where a thin sample permits the primary electrons to pass through the sample to be detected. This mode of operation can produce high-contrast images for small features if the sample supports transmission. Because the samples must be thinner, the interaction volume is even smaller than in conventional SEM, resulting in improved resolutions. Using the primary electron beam means that the signal-to-noise ratio (SNR) is typically better and Z-contrast images can be obtained in some samples. Semiconductor NCs are ideal samples to image with the STEM-in-SEM technique because they are composed of high-Z materials and the small particles settle into thin layers that support transmission—particularly NC clusters which deposit into single layers with little 3D stacking.

3.2. Transmission Electron Microscope

A more complex and sophisticated system, the TEM uses a higher energy electron beam than SEM in an imaging configuration: lenses focus and image the beam much like a conventional optical microscope. Focusing and imaging requires a greater degree of precise control and manipulation of the electron beam and the number of elements in such instruments is significantly more than its SEM cousin. The necessary transmission configuration of the instrument places restrictions on the types of samples that can be imaged. Figure 3.2A depicts the basic components of high resolution TEM (HR-TEM). Rather than raster scanning the electron beam, HR-TEM uses an imaging device like a camera, phosphorus screen, or film to produce a map.

HR-TEMs can register interference effects due to the wave properties of the high energy electrons of the probe beam (however, this is not unique to HR-TEM operation only). Samples with crystalline regions can, therefore, exhibit interference effects—fringes—that provide additional information about the lattice including orientation and structure. This can be particularly informative in NC systems to diagnose crystal defects or disorder.

A STEM mode similar to that described for the SEM is also compatible with the TEM. However, other detection schemes can be implemented that provide more scattering information. Figure 3.2B depicts the configuration of STEM-in-TEM. High angle annular dark-field (HAADF) imaging places detectors in anuli around the primary beam. High angle scattering rates are extremely sensitive to the atomic number of the scattering material and this method produces detailed Z-contrast maps. Because the center beam is not blocked, both the dark-field and bright-field can be imaged simultaneously, obtaining Z-contrast, topographical, and diffraction information in a single measurement. If a camera is used in place of the typical

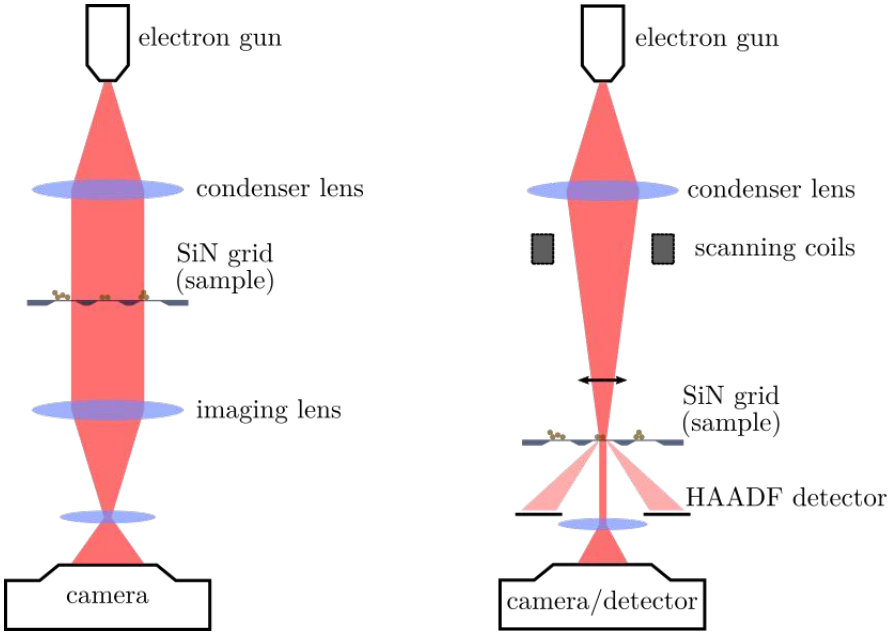

(A) HR-TEM (B) STEM-in-TEM

FIGURE 3.2. Modes of operation of HR-TEM and STEM-in-TEM.

STEM rate detector, interference of the primary beam can be imaged and provide detailed diffraction patterns at specific points within a sample with exceptionally high resolution.

While most applications of TEM to NCs concern batch characterization to validate synthesis approaches, a few studies have appeared that draw correlations between structure and single-molecule fluorescence. The work of Koberling *et al.*[17] first reported high QYs do not require achieving high-quality crystalline structure and NCs that exhibit polycrystallinity or stacking faults have strong fluorescence. Later correlated studies with polarization spectroscopy by the same group demonstrated that even spherical NCs and polycrystalline NCs emit elliptically polarized light, indicating orientation may not necessarily be predicted from fluorescence measurements alone[18]. Orfield *et al.*[19] investigated NCs with poor shell coverage in the context of blinking behavior. Larger numbers of Cd surface sites were identified

as contributing to trap states, resulting in an enhancement of the non-radiative recombination pathway. The group later used correlated TEM experiments to study the structural effects on giant, non-blinking NCs where trap states are moved farther away from the core[20]. However, few works have turned the power of EM imaging towards investigating clusters of NCs where interaction between NCs may occur.

3.3. Characterization of Nanocrystals and Clusters

NC clusters synthesized according to the rapid method detailed in Appendix A were imaged by TEM to identify characteristics resulting from the clustering process. Figure 3.3 shows a HR-TEM image of a trimer from the middle segment of an ultra-centrifuged batch with each of the constituent NCs circled in white for identification. 2D Fourier transforms of fringe patterns from HR-TEM images provide information about the lattice that scattered the electron beam. The Fourier transforms of the fringe patterns from each NC are shown in the same figure. It is clear that each NC has a different diffraction pattern which is reflected in the Fourier analysis of the fringes. None of the clusters imaged by HR-TEM exhibited correlation among the diffraction patterns of the constituent NCs. Furthermore, clusters did not appear to form chains nor follow any obvious super-lattice patterns.

Defining the extents of such small NCs in HR-TEM can be difficult and another imaging mode can provide improved feature recognition. Figure 3.4 shows the HAADF image and bright-field scattering of a different trimer from the same clustered batch. The trimer is made up of three NCs that are very different: their size, shape, and Z-distributions indicate that the NC building blocks were not homogeneous and suffered from a high degree of variability. As commercially synthesized NCs, this is not unexpected as the preparation methods are often aimed to produce the highest batch QYs. The Z-distribution subtly indicates that

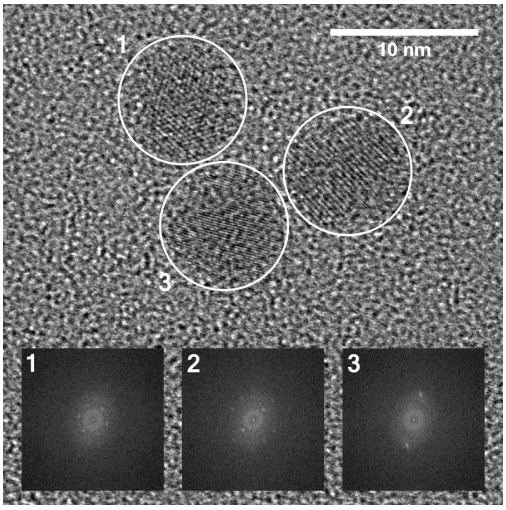

FIGURE 3.3. NC cluster imaged with HR-TEM. The 2D Fourier transforms of the image sub-regions corresponding to each NC are shown at the bottom. Each NC of the cluster has a unique diffraction pattern.

the higher-Z core material (CdSe) can be located off-center inside irregular shells. Hence, core separation distances (i.e. for ET calculations) do not follow directly from center-to-center measurements, particularly for synthesis batches that are not well characterized. The STEM-in-TEM measurement also corroborates what the HR-TEM fringe analysis indicates: the diffraction pattern of the bright-field beam is different for each NC in the cluster. To place this observation of uncorrelated diffraction patterns into context of NC structure, the clustering process, ET coupling, and, ultimately, the fluorescent properties of clusters, we must recognize the role the crystal lattice has among these various NC properties.

Oriented attachment can produce order in two ways: in the geometric arrangement of the NCs, as observed by some hexogonal close packed (hcp) super-lattices[3], and in the relative crystal lattice orientations between neighboring NCs[105]. The mechanism for both is commonly attributed to the interaction of the permanent dipole moments of the NCs. Dipole strengths are proportional to the NC size, ranging from 40 Debye for 3 nm diameter CdSe NCs to 100 Debye for 6 nm NCs[106]. ZnS scales similarly but is slightly weaker. Hence, the thin- and thick-shell CdSe/ZnS NCs in this work are expected to posses relatively significant

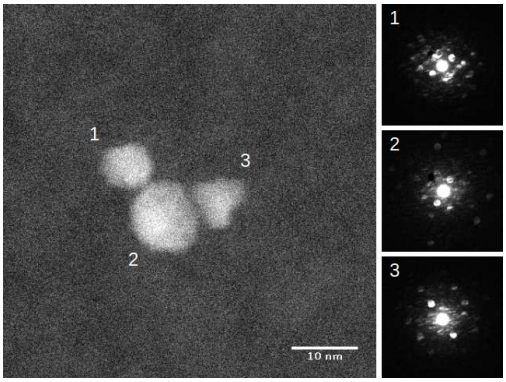

FIGURE 3.4. HAADF imaging of a NC cluster with the associated bright-field scattering from each NC. Some degree of Z-contrast relief discern between core and shell material.

dipole moments due to their size. Screening by the passivating ligand layer has been shown to have minimal effect on the dipole strength[107]. However, the origin of the NC dipole moment is still not completely understood and two explanations dominate the conversation. In one explanation, the dipole moment is fixed to a particular crystal axis (i.e. the c-axis in wurtzite) due to the lattice type[107, 108]. Such a fixed dipole moment would result in every NC having the same relationship between dipole moment and lattice, which can result in the correlation of lattice orientations among NCs in close proximity. A second explanation for the source of the dipole moment is the configuration in which particular crystal facets terminate. Shim *et al.*[106] suggests that the facets of NCs are decorated with surface charges due to the finite lattice extent and the terminating atomic species gives rise to a dipole moment not specifically oriented along a particular axis nor common to all NCs of the same type. While this mechanism can form higher-order structures where lattice orientations are correlated from high-quality NCs[3], in general lattices may be uncorrelated if there is sufficient surface irregularity, such as the thick, non-spherical NCs in Figure 3.4. The environment and time-scale during which clustering proceeds may also render the dipole-dipole forces insignificant enough for orientation into the lowest energy configuration to occur.

The crystal lattice has a more deterministic role for the emission dipole, uniquely specifying the orientations of the 1D spin 0 transitions and the 2D plane for spin 1 transitions. This is particularly important when considering ET. Although a simple observation, the seemingly random lattice orientations suggests ET coupling for the clusters characterized above will not be at the maximum efficiency. The ET theory from Scholes and Andrews[96] indicates the orientation factor peaks when the c-axis of NCs are aligned parallel or anti-parallel for both the circularly polarized states and the linearly polarized state. Furthermore, in the parallel and anti-parallel orientations, the spin state is either maintained or flipped during transfer for the circularly polarized states. As a function of the relative angles of the donor/acceptor NCs and the vector between them, the ET rate can vary by as much as an order of magnitude; however, the κ factor does not approach zero for any orientation. Figure 3.5 illustrates the implications of the energy transfer efficiency variations in terms of κ for two NCs involving circularly polarized states as a function of the azimuthal angle ϕ between the NCs.

While EM diffraction imaging is a powerful tool for characterizing NCs, particularly for high-quality NCs, polycrystallinity and polytypism complicate the determination of orientations and the energy level landscape enough that specific ET coupling predictions cannot be made for the NCs used in this study. Polycrystallinity was measured in HR-TEM images of many NCs, especially the thick-shell NCs. Furthermore, the core CdSe material and shell ZnS material are both polymorphic and can form wurtzite (hexagonal) or zinc-blende (cubic) crystalline structures, requiring sophisticated and difficult EM imaging methods to sort out at single particle resolutions.

Comparing groups of unattached NCs to clusters is informative about how NCs settle on a substrate. Figure 3.6 shows the STEM-in-TEM imaging of two different samples:

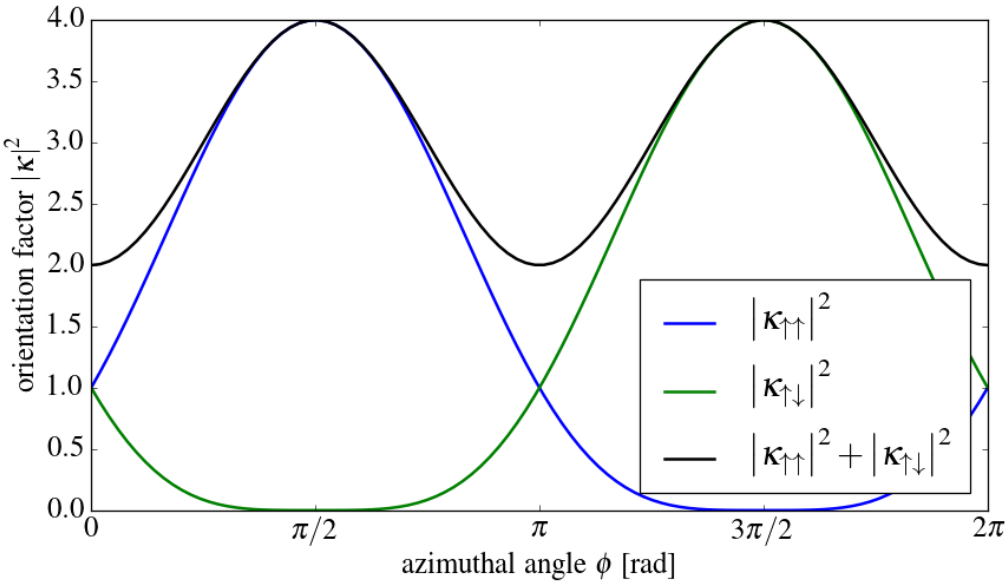

FIGURE 3.5. The orientation factor for ET between spin 1 states as a function of the azimuthal angle ϕ for one of the NCs, the other fixed at $\phi = \pi/2$. The polar angles of each NC are fixed at $\theta = \pi/2$. Angles are measured relative to the c-axes of the NCs and the separation vector $\vec{r}$.

(1) unclustered thin-shell NCs deposited as singles (Figure 3.6A), and (2) a large cluster of thick-shell NCs formed by rapid MeOH treatment (Figure 3.6B). Several observations are worth discussion. First, the inter-particle separation distances (gap size between NCs) are significantly different between unclustered single NCs and attached NC clusters. The size of the gap between single NCs is primarily set by the ligand length—octadecylamine in this case. Clusters, however, have either entangled ligands or direct physical contact, which is clearly indicated by EM imaging by the smaller gaps. Second, even single NCs from the less than high-quality batches studied here appear to easily self assemble into super-lattices with long range hcp structure. Several studies have also observed this[8, 9]. This is likely a combination of the solvent drying process being slow enough that order can be established, driven by dipole interactions, and the freedom of motion the ligands provide, acting like a surfactant during the process. In contrast, clusters do not demonstrate

this level of collective ordering and appear to form irregular arrays of NCs, which was alluded to earlier. That NCs form faceted attachments during clustering is not supported by the diffraction imaging which indicates random lattice orientations for such clusters. Furthermore, clusters always appeared as flat, 2D structures in EM imaging, indicating a malleability upon deposition where clusters can reshape yet remain large units. Little is understood about the malleability of clusters after attachment: ligands are known to diffuse, which could enable NC settling into aligned configurations that reduce the energy of the system, but faceted physical attachment of the NCs may suppress reordering or limit the configurations that can occur. These observations suggest that the rapid MeOH clustering treatment does not produce oriented attachments and, despite the flexibility for clusters to reshape, the forces between dipole moments are not strong enough to create hcp lattices once NCs are attached.

Concentrated batches of NC clusters imaged with EM at relatively low magnification, such as Figure 2.6, provide meaningful statistics about size, shape, and inter-particle separation distances. Shown in Figure 3.7 are the distributions of gap sizes, particle diameters, and nearest-neighbor separation distances for thin-shell single NCs and thick-shell clusters. Analysis of the hundreds of NCs and clusters was done with ilastik[109], a feature classification software package. For simplicity, the particle diameter is reported despite the irregularly shaped NCs that were used. Thin-shell NCs clearly have smaller diameters and a narrower distribution compared to the thick-shell NCs. The distributions of gap sizes, determined by the difference between nearest-neighbor and particle diameter measurements, shows that un-clustered, single NCs naturally space farther apart than clusters—the octadecylamine covering ligand has a length of ~ 1.4 nm. Thus, attachment in the rapidly formed clusters results in spacing shorter than ligand buffering would produce, which suggests the form of

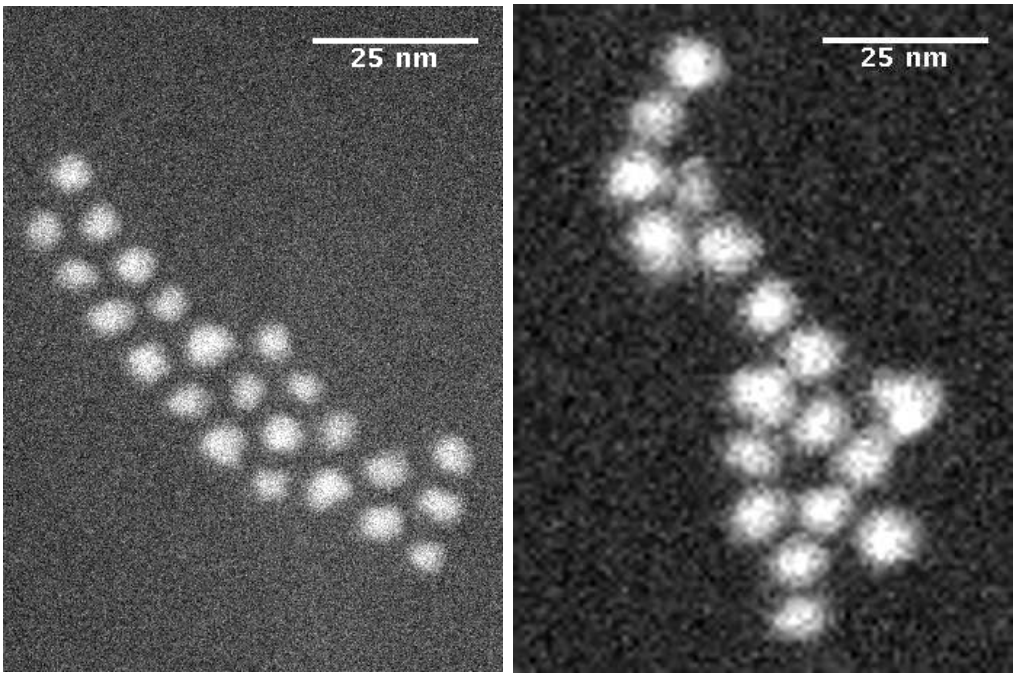

(A) Thin-shell NCs as singles (B) Thick-shell NC cluster

FIGURE 3.6. TEM images of thin-shell NCs before clustering (Figure 3.6A) and thick-shell NCs after clustering (Figure 3.6B). Both images are at the same magnification. Separation gaps due to the ligands are visible in the pre-clustered sample while the clustered sample shows close-contact separation.

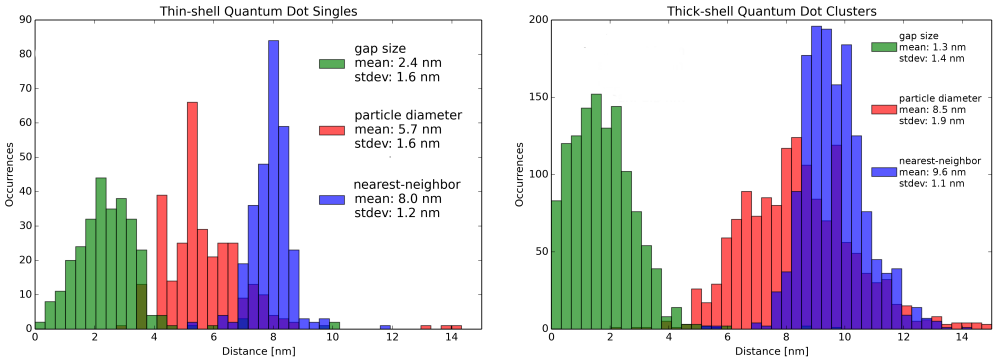

(A) Thin-shell NCs (B) Thick-shell NCs

FIGURE 3.7. Size and spacing distributions for thick- and thin-shell NCs.

attachment could be due to unsaturated surface covering ligands producing patches that enable closer contact, or even direct contact. Summarized in Table 3.1 are the mean NC diameters, nearest-neighbor distances, and gap sizes from the distributions in Figure 3.7.

TABLE 3.1. Distribution summary of particle diameter, nearest-neighbor center-to-center spacing, and gap size for thin-shell single NCs and thick-shell clusters.

	NC diameter [nm]	nearest-neighbor [nm]	gap size [nm]
singles (thin-shell)	5.7(1.6)	8.0(1.2)	2.4(1.6)
clusters (thick-shell)	8.5(1.9)	9.6(1.1)	1.3(1.4)

CHAPTER 4

Single-molecule Fluorescence Microscopy

Single molecule spectroscopy is a collection techniques and methods that aim to measure the properties and behaviors unique to specific, individual molecules. Bulk measurements sample many identical molecules simultaneously and benefit from a strong signal to which multiple particles contribute, but such measurements can also obscure the details of how individual particles behave. The blinking phenomenon of semiconductor nanocrystals, for example, is not apparent from bulk excitation of the particles. Although NC clusters contain multiple particles, the fluorescence emitted by them can still be treated like a single-molecule signal for sufficiently small clusters. Blinking actually enables the application of single molecule techniques to clusters because only a few emitters may be active in a cluster at a time and individual on/off transitions are not overwhelmed by large photon statistics from the group. A wide variety of variations and configurations can be used to make single-molecule measurements using conventional microscopes. Two instruments were used for fluorescence measurements in this work: a confocal microscope and a wide field microscope configured for total internal reflection fluorescence (TIRF) illumination.

This chapter describes the experimental components of the two microscopes used in this work. Section 4.1 details the confocal microscope that is used to obtain lifetime and spectral measurements in Chapter 5. Section 4.2 provides an introduction to the field of super-resolution microscopy with emphasis on the approaches put forth in the literature to perform fitting and analysis. Finally, Section 4.3 relates efforts by this author to apply multiple-emitter approaches to resolve the emitters at the short separation distances found in NC clusters with suggestions for moving forward.

4.1. Confocal Microscopy

A confocal microscope, such as the configuration depicted in Figure 4.1A, is an instrument that improves the SNR of measurements by collecting light from only a small, single-point focal volume. Light from outside a fixed focal volume is rejected by placing a pinhole at an intermediate imaging plane. The excitation light is likewise only concentrated to the same focal volume as the detection—hence the term confocal. Alignment of a confocal system is simplified if an infinity corrected objective is used. Working in the infinity space of the objective, a collimated laser source focuses to the same depth as the detection arm and in-plane adjustments of the pinhole at an intermediate imaging plane co-localizes the detection and excitation volumes. Scattered light is minimized because the excitation volume is limited to a single diffraction-limited region and the detection volume rejects any photons originating from outside the same volume. Because photons from only a small volume are collected at a time, the sample must be positioned such that a fluorescent particle of interest is inside the confocal region, which typically involves scanning a sample around the focus. The confocal microscope used in this work paired a 100 μm diameter pinhole with a Zeiss Fluar 1.3 NA, 40$\times$ infinity-corrected objective lens.

4.1.1. Time-tagged Time-resolved Measurements. Particular excitation and detection configurations of fluorescence microscopes provide accurate measurements of the lifetime of a fluorescent molecule. A pulsed laser source may be used to excite a fluorescent molecule within a short and finite interval. Because the excitation is momentary, the excited state of the single-molecule evolves without the influence of external fields, decays according to the mechanics of the molecule, and the individual excitation/emission events from the molecule can be recorded. Detecting the photon or photons from a single excitation event

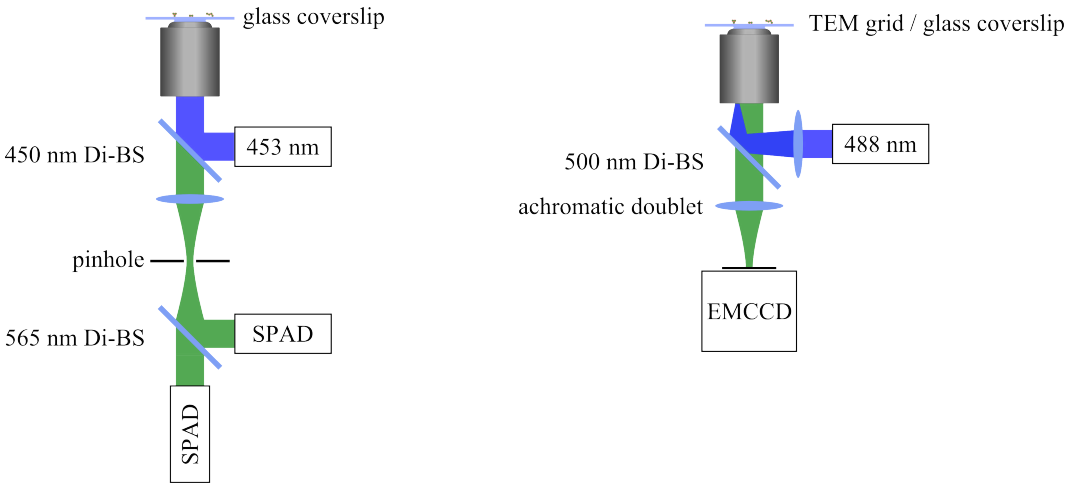

(A) Confocal microscope (B) TIRF microscope

FIGURE 4.1. Diagrams of the excitation and detection beam paths in a confocal microscope (Figure 4.1A) and a wide field TIRF microscope (Figure 4.1B).

is efficiently done with avalanche photodiodes (APDs) that produce an electronic pulse for every photon detection event. Pulses are registered by counting hardware in reference to the timing signal when the excitation pulse occurred, and each photon event is recorded with the information about the absolute timing of the event within the duration of the measurement and the timing of the event relative to the excitation. This dual-timing information is called a time-tagged time-resolved record, schematically represented in Figure 4.2, and is the basis of the paired single-molecule lifetime measurement with emission intensity fluctuations.

The confocal experiment in this work used two PicoQuant τ-SPAD APDs with the PicoQuant TimeHarp 200 counting hardware, which, together, are capable of measuring timing resolutions down 144 ps at detection rates as high as 1 MHz. A PicoQuant LDH-P-C-450B 453 nm pulsed laser source with 68 ps FWHM pulse width was used for excitation. The beam profile from the diode laser was cleaned by coupling to a fiber and recollimated before passing the beam into the confocal microscope. While the source is specified to have $> 90\%$ linearly polarized emission, the fiber coupling does not preserve the polarization. A 450 nm

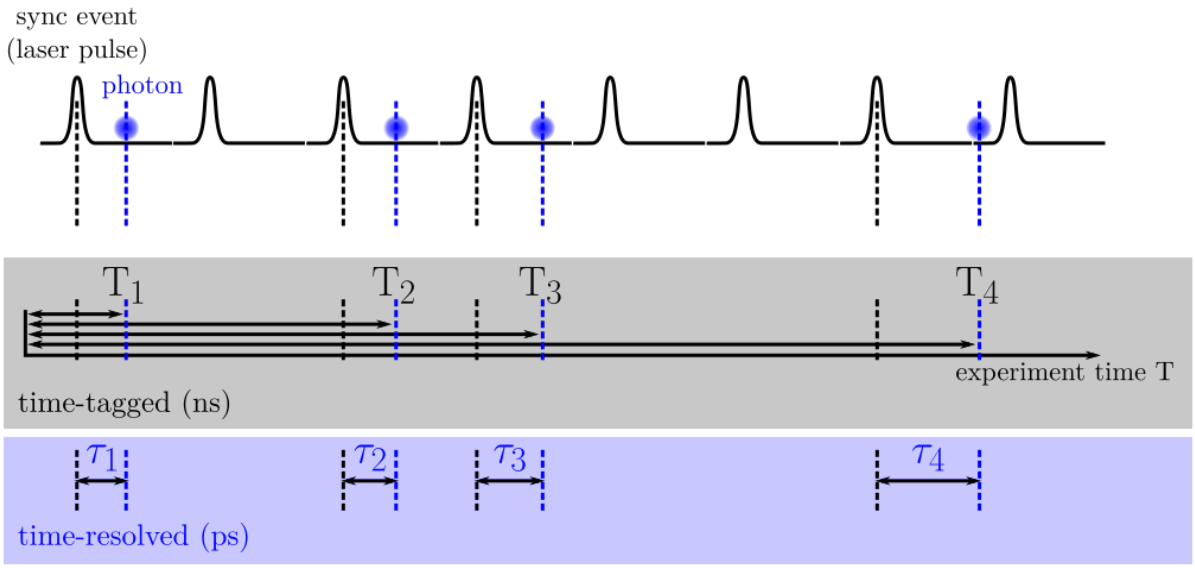

FIGURE 4.2. Concept of time-tagged time-resolved measurements. Excitation pulses may produce a detected photon event. When a photon is detected, information about the absolute timing of the event, T_i, and the relative timing in relation to the excitation, τ_i, are recorded. A measurement is the collection of all photon events that occurred with both of these pieces of information.

dichroic beam splitter separated the excitation and detection beam paths. An additional 525 nm long pass filter was placed before the detection beam splitter to further filter out scattered excitation light and a laser line clean up filter was placed before the microscope to remove the infrared emission common from diode lasers.

4.1.2. SPECTRAL MEASUREMENTS. Single-molecule spectral measurements provide another level of information that can inform about the dynamics of a system. Measurements from a spectrometer typically require a trade-off when investigating single-molecule sources: a detailed spectra requires integrating over time to collect enough photons for the measurement, but integration reduces the temporal resolution and will obscure the spectral dynamics of the system. Furthermore, simultaneous time-tagged time-resolved measurements are not compatible with integrating sensors such as a camera that are necessary for spectrometers. While there is fine structure to the emission spectrum of a single NC, at room temperature

the emission profile of the $1S_{3/2}$–$1S_e$ transition is well characterized by a Gaussian profile. Placing a dichroic beam splitter in the detection path of a confocal microscope splits the photon stream into a blue- and red-channel[110]. Therefore, by matching the transition wavelength of the dichroic to the peak emission wavelength of the molecule of interest, a dynamic measurement of the central wavelength can be acquired simultaneously with lifetime dynamics by comparing the relative blue- and red-channel detection rates. The ratio

$$r = \frac{I_{\mathrm{R}} - I_{\mathrm{T}}}{I_{\mathrm{R}} + I_{\mathrm{T}}}$$

where I_{R} is the intensity of the detector on the reflected arm (blue-channel) and I_{T} is the intensity of the detector on the transmitted arm (red-channel), is used to calculate the emission wavelength center. The binned trajectory of each detector channel is used to calculate the ratio r, from which a wavelength is assigned to each bin based on a calibration curve. The confocal measurements in this work used a 565 nm dichroic beam splitter to send the photon stream to two APDs. Convolving the transmission and reflection curves of the dichroic with a Gaussian profile yields a calibration curve for each detector and the ratio above defines how the measured detector rates are related to the wavelength. Figure 4.3 shows the calibration curve for the dichroic used.

4.2. Super-resolution Microscopy

Wide field microscopes image the spatial distribution of the point spread function (PSF) from a fluorescent molecule. While confocal instruments provide high temporal resolution, they do so at the expense of obtaining spatial information. Super-resolution (SR) microscopy is a broad term that encompasses instrumentation advances, measurement approaches, sample preparations, and analysis methods to obtain single-molecule localization below the

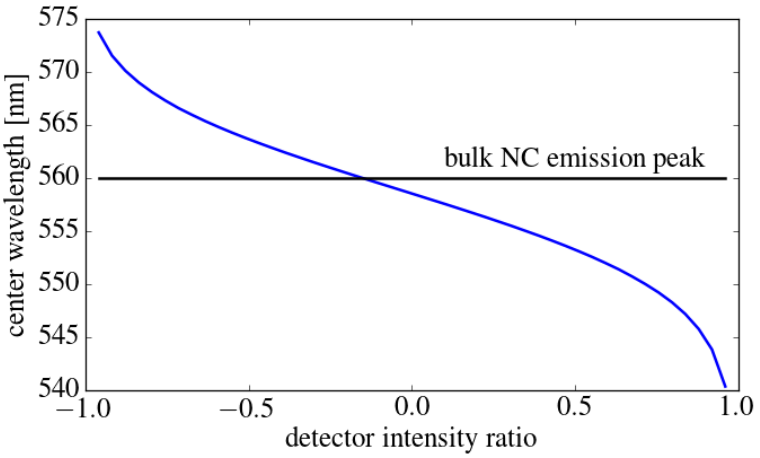

FIGURE 4.3. Spectral calibration curve for confocal measurements. The transmission and reflection curves of a 565 nm dichroic beam splitter are convolved with a 15 nm FWHM Gaussian profile (determined from the bulk single NC spectral profile at room temperature).

diffraction limit. Traditional microscopy is limited to identifying features no smaller than a few hundred nanometers due to the resolving power set by the diffraction limit of light. In a seminal paper, Yildiz *et al.*[111] measured the individual steps of the hand-over-hand movement that myosin V traverses actin filaments. The approach was a combination of single-molecule labeling, high SNR imaging devices and instrumentation, and the recognition that the center of a PSF can be numerically calculated to arbitrarily high precision with a sufficient number of photons[112]. Spatial localization with resolutions of $\sim$ 1.5 nm are now routinely obtained and the methodologies Yildiz *et al.* introduced heralded the era of super-resolution microscopy.

Later biological imaging by Betzig *et al.*[113] built upon these methods and demonstrated structural reconstructions of—among several inter-cellular structures—the actin filaments with spatial resolution of $\sim$ 2 nm in a technique termed photoactivated localization microscopy (PALM) Simultaneously, Rust *et al.*[114] demonstrated a similar technique, stochastic optical reconstruction microscopy (STORM) and the two methods are now the

standard-bearers of SR imaging for biological applications. The on/off switching of fluorescent molecules utilized in PALM is the basis of many SR approaches and draws obvious parallel to NCs blinking—a point that underscores the ideal pairing of SR microscopy with NC cluster studies. Even as the field of SR microscopy has matured, many new applications of the general methodologies are continually introduced[115, 116]. It is the contents of this work that expands microscopy into a new direction by investigating structure of NC clusters at the length scales accessible with SR microscopy.

To obtain SR measurements, the setup depicted in Figure 4.1B was used. The simplicity of the system betrays the power of such a microscope configuration. A central component to obtain quality images for SR localization is achieving a high SNR. Bright semiconductor NCs have an intrinsic advantage over many dimmer organic fluorophores due to their high QY. A total internal reflection microscope (TIRF) further improves the SNR. Using an infinity corrected objective and focusing an excitation source at the back imaging plane results in a collimated beam exiting the objective. Careful engineering of the beam profile can produce a nearly homogeneous excitation flux across the field of view and provide the same excitation conditions for all fluorescent molecules in the field of view. In TIRF, the angle of the focusing excitation beam is adjusted to satisfy the optical criteria for total internal reflection at the objective/sample (glass/air) interface and the evanescent wave travels only $\sim$ 100 nm into the sample. Similar to a confocal microscope, the excitation region is limited to a small volume to reduce the amount signal from scattering; however, instead of a small spot, TIRF produces a thin plane of excitation at the interface.

On the detection side, an electron multiplying charge coupled device (EMCCD) images the sample with single-photon efficiency and produces high SNR images at high frame rates. The SR in this work used a custom built TIRF microscope with an Olympus Apo N 1.49 NA,

60× oil immersion objective and a Princeton Instruments ProEM 512B EMCCD[117]. The excitation and emission beam paths were separated with a Semrock FF500/646 dual-edge dichroic beam splitter and the emission was further cleaned by a Semrock FF01-562/40 band pass filter. A quarter-wave plate could be inserted into the excitation path of the 488 nm Coherent sapphire source to produce circularly polarized excitation. The magnification of a microscope to be used for SR imaging requires the PSF be spread across enough of the camera pixels that enough information about the PSF shape can be obtained. However, too high a magnification and the individual pixels received too few photons to overcome the intrinsic detector noise. At 150× magnification, the TIRF microscope had an effective pixel size of 106 nm, near optimal condition for SR measurements.

4.2.1. Point Spread Function Models. The localization improvement of SR microscopy stems from making full use of the information contained in the intensity distribution of the PSF to estimate the center of a single-molecule spot with higher precision than the apparent maximum intensity pixel location would imply. In particular, low intensity rings contribute significantly to the estimation if given proper weight. However, selecting an appropriate model PSF to fit the image data to is not a trivial task. Particularly when multiple spots must be fit, as in the case for PALM and similar imaging modalities, model PSFs that require minimal computation time during the fitting process have been favored over more precise models. A discussion about the most prominent models emphasizes these issues.

The simplest and most recognizable model PSFs in SR microscopy are the 2D versions of the Airy disc and the Gaussian function. Derived from a simple scalar optics approach of the diffraction pattern produced by a circular aperture, the Airy disc has a firm basis in the

physical origin of the PSF:

$$q(x, y, \{\boldsymbol{\theta}\}) = \frac{1}{\theta_\sigma^2} \cdot \frac{J_1^2\left(\theta_\sigma \sqrt{(x-\theta_x)^2 + (y-\theta_y)^2}\right)}{(x-\theta_x)^2 + (y-\theta_y)^2}$$

where θ_i are the fit parameters (θ_σ has a specific relationship to the optical parameters of the imaging system, but is often left as a fit parameter) and J_1 is the Bessel function of the first kind of order one. The low intensity rings produced by diffraction are represented in the Airy function. However, the Gaussian function is a good approximation to the center region of the Airy function:

$$q(x, y, \{\boldsymbol{\theta}\}) = \frac{1}{2\pi\theta_\sigma^2} \exp\left(-\frac{(x-\theta_x)^2 + (y-\theta_y)^2}{2\theta_\sigma^2}\right)$$

Figure 4.4 illustrates the accuracy of this approximation. The intensity in the rings is small compared to the central region and is generally considered insignificant. Both functions represent similar computational demands in the above forms. However, the next level of model sophistication is the incorporation of pixelation effects due to the imaging sensor. This is done by integrating the PSF over the pixel size

$$\mu_k(\{\boldsymbol{\theta}\}) = \theta_I \int_{A_k} q(x, y, \{\boldsymbol{\theta}\}) \mathrm{d}x\mathrm{d}y + \theta_{bg}$$

where μ_k is the intensity of the PSF at pixel k and A_k is the area of the pixel and depend. Smith *et al.*[118] published an algorithm that makes use of the relatively simple form of the pixel-integrated Gaussian and the closed form of its derivatives that is commonly used for SR analysis. While a more precise description of the PSF, the Airy disc does not have such a tractable pixel-integrated form and fitting requires either additional approximations or numerical integration, a computationally intensive task.

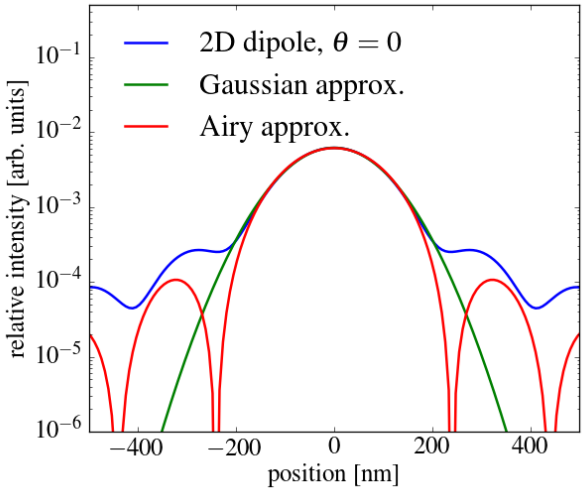

FIGURE 4.4. Lineout of the PSF produced by a 2D dipole emitter with the optical configuration used in the TIRF experiments (1.49 NA, 106 nm pixels, 565 nm emission wavelength). Fits to the dipole PSF using a Gaussian function and an Airy disc show strong deviations outside the central 400 nm spot.

Recently, developments into models that consider the PSF produced by a dipole emitter have gained attention in the SR field[119–121]. Single dipole emitters produce an anisotropic PSF that will bias SR localizations if symmetric PSF models are used[122, 123]. Dipole models treat the image produced by high-NA objectives with a field-vector framework that is able to capture the subtleties of real dipole emission effects[124]. Furthermore, fitting such models retrieves orientation information of the emitter. These model PSFs can incorporate additional parameters that characterize the optical system in greater detail and the deviations thereof, including the index of refraction of the various embedding media, the effective focus of the imaging system, and the contributions of large collection angles introduced by high-NA objectives. Figure 4.4 shows the calculation of a 2D dipole emitter and the least-squares best fit of the Gaussian and Airy models to the dipole model. Although the Airy function is appreciated for its inclusion of the low intensity rings caused by diffraction, it is clear that the higher intensity central region will dominate fitting routines and results in poor matches for the rings when compared to dipole models. This is particularly problematic

for 2D dipole emitters where the central peak is broadened independently of the diffraction rings.

Because of the complexity of dipole models, the equations describing the PSFs typically require slow numerical evaluations even when approximations are used[121]. This has hindered the application of such models to SR microscopy, where high throughput is desired for biological imaging and the fit bias of symmetric model PSFs is often not an issue. Auget *et al.*[119, 120] recognized the orientation components and the position components of the full representation can be factored and presented a computationally improved approach to SR dipole fitting using steerable filters. However, dipole models are still typically only used when single-molecule orientation angles are the primary parameters of interest.

A final method that provides models for SR fitting is to characterize the PSF produced by the instrument experimentally and use a deconvolution approach to obtain the SR localizations. The astronomy software DAOPHOT II[125] takes this approach for star fields and the DAOSTORM adaptation implements the tools for SR microscopy[126]. Because the instrument response function (IRF) of a microscope can introduce additional aberrations that cannot be easily addressed by a theoretical model, the experimentally characterized PSF algorithms can accommodate distortions unique to a particular instrument or measurement. While dipole effects can, in theory, be corrected with careful PSF characterization, in practice this may not be possible as individual molecules with different dipole orientations within the field of view or with non-static orientations will not result in a single characterization that applies to all emitters across all times. The rotational freedom of some labels or emitters often negates these issues and, therefore, such characterization-based approaches are widely used. Appendix D details several artifacts of both the PSF characterization method and model-based approaches[127].

4.2.2. Fitting Methods and Noise Models. With an appropriate model PSF selection, fitting proceeds by maximizing (or minimizing) a function that compares the image data to the model. Many algorithms exist that perform the optimization task with or without parameter bounds or knowledge of the derivative of the comparison function which stabilize solution searches and improve computation time. Least-squares and weighted least-squares are simple comparison functions that provide rudimentary fitting and are largely ignored in SR analysis due to their inaccuracy with small signals. Maximum likelihood estimation (MLE)[128], favored by the SR community, defines a likelihood function $\mathcal{L}(\boldsymbol{\theta}|s_k)$ that is the joint probability function of a particular model parameter selection $\boldsymbol{\theta}$, given the measured pixel intensity values on the camera s_k

$$\mathcal{L}(\boldsymbol{\theta}|s_k) = \prod_k p_{s_k}(\boldsymbol{\theta})$$

Often the logarithm of the likelihood function is calculated when the intensity values are large.

There are several choices for the marginal probability function in MLE, depending on the noise model that is appropriate to the SR measurements. Since photon emission is a Poisson process, a basic marginal probability function that considers only the variation of the number of photons reaching the detector is[118]

$$p_{s_k}(\boldsymbol{\theta}) = \frac{\mu_k^{s_k} e^{-\mu_k}}{s_k!}$$

where the explicit dependence of the model on the model parameters has been suppressed. In this form, the background parameter θ_{bg} is included as a Poisson noise source and has the physical meaning of a real background photon rate such as a uniform scattering.

SR localization can be improved by considering noise models that capture some of the detection characteristics of the instrument. This is particularly important for giving significance to pixels with count rates on the order of the noise level. Because the EMCCD is an electron multiplying device, amplification is a stochastic geometric process initiated by the Poisson detection process quoted above[129]. For SR microscopes equipped with an EMCCD, the gain g and the statistics it introduces can be included in the marginal probability function[121, 130, 131]

$$p_{s_k}(\boldsymbol{\theta}) = e^{-\mu_k} \cdot \delta(s_k) + \frac{1}{s_k}\sqrt{\frac{\mu_k s_k}{g}}\, e^{-s_k/g-\mu_k} \cdot I_1\left(2\sqrt{\frac{\mu_k s_k}{g}}\right)$$

where δ is the Dirac delta function and I_1 is the modified Bessel function of the first kind of order one. The measured signal is further convolved with a Gaussian distribution arising from detector readout noise[130]. Because readout noise can result in negative count values, a constant factory offset of 500–1000 counts is programmed into such detectors. Identifying and subtracting this offset is necessary to convert the acquired signal to the true raw signal which is properly represented by the Poisson and exponential statistics of the noise models. The readout noise is often small and the analysis implementations in this work did not incorporate this convolution step in favor of reliable solution convergence.

Many SR fitting packages, although powerful and fast, adopt varying degrees of model complexity, particularly for noise models. It is up to the researcher to identify when more sophisticated methods are necessary and perform due diligence benchmarking the selected algorithms for a particular application. Often a custom implementation is necessary to perform fitting that a mainstream package cannot accommodate. The fundamentals of SR fitting outlined above are meant to be a starting point for constructing custom algorithms and the references within are excellent sources to do so. Three SR algorithms were used

for the NC cluster studies presented in the following chapters and each chapter outlines the arguments behind each choice.

4.3. The Multiple Emitters Problem

A major issue of SR fitting is the treatment of overlapping PSFs. The Rayleigh criterion for epifluorescence microscopes (both confocal and TIRF are in this category) represents the minimum resolvable distance between two point sources where the overlap is sufficiently great that conventional microscopy cannot determine the independent positions of the sources:

$$R = \frac{0.61\lambda}{\mathrm{NA}}$$

where λ is the wavelength of the light and NA is the numerical aperture of the imaging objective. Already SR microscopy breaks this convention for resolving power; however, overlapping emitter PSFs require special considerations and, in general, the accuracy of such measurements is significantly lower than the case of widely separated emitters.

The multi-emitter problem is often framed in the context of biological imaging where there is a trade-off between the number of frames that need to be acquired to build up a SR image and the density of the fluorescent labels. However, higher densities of labels result in the higher probability that PSFs will overlap. Even high density images contain valuable information if a method to sort out overlapping emitters is used. A common solution to the issue of multi-emitters in SR analysis is to apply an iterative approach where a single emitter is found and then the residuals are used to guide subsequent iterations that attempt to fit additional PSFs to the region[132, 126, 133, 134]. In the spirit of PALM and STORM, approaches that utilize the temporal fluctuations of emitters between frames in combination with SR fitting have been successful deconvolving dense fields of emitters[135–139].

NC clusters also present the situation where multiple emitters may be contributing to the imaged spot. Because ET may be inefficient enough that the individual blinking events of the NCs in a cluster produce a fluctuating emission origin or large clusters may have only limited ET distances resulting in several acceptors within the cluster, multiple PSFs separated by $\sim$ 10 nm may contribute to the signal. However, most of the blind multi-emitter algorithms cannot accurately distinguish signals from emitters separated less than 100–200 nm. We investigate the viability of two alternative approaches through simulation of achievable experimental conditions: a fixed-model fit based on *a priori* knowledge of the emitter locations and an independent component analysis.

4.3.1. Multiple Model Functions. Motivated by the recognition that EM imaging of NC clusters can provide information about the specific arrangement of the NCs within the cluster, we investigate if a patterned PSF approach is capable of identifying the true emitting configuration of a cluster. Even clusters with efficient ET will produce emission from each of the NCs—ET and fluorescence are competing rates—and the resulting imaged spot will be the combination of multiple PSFs centered on slightly different positions. Consider the simple case with three NCs in closest-contact (a pyramid), separated by the distance d, and each NC in a cluster has the same intensity. The five unique emitting configurations are illustrated in Figure 4.5. These configurations were simulated with the combination of Poisson photon noise and Gaussian readout noise to produce images that had signal and noise characteristics matching the experimental conditions of (1) the correlated SEM experiments of Chapter 6 and (2) the best case TIRF imaging obtained by the instrument (NCs directly on glass coverslip). Each configuration was simulated at inter-particle separation distances

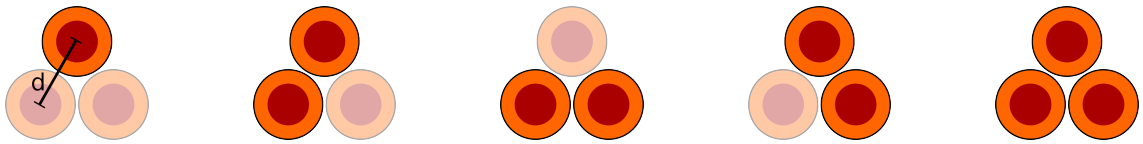

(A) Monomer (B) Dimer #1 (C) Dimer #2 (D) Dimer #3 (E) Trimer

FIGURE 4.5. Configurations for model function-based super-resolution fitting.

d spanning 5–500 nm with 10,000 images to each configuration/distance pair. The pixel-integrated Gaussian model was used to generate the individual PSFs as no particular model selection should inherently result in better fitting so long as the fit model matches the source.

A modified implementation of the Smith *et al.* algorithm[118] was used to fit the simulated data that could accommodate multiple emitters at pre-specified and fixed relative positions. Every image of a particular separation distance was analyzed by a PSF model patterned after each of the configurations in Figure 4.5 at the given separation distance. The same pixel-integrated Gaussian function was used as the model PSF; however, for speed and simplicity, only a Poisson noise model was applied for the likelihood function definition. In addition to the final parameter estimations (θ_I, $\theta_{x,y}$, and θ_{bg}), the value of the likelihood function was recorded for each fit. Parameter estimations were always accurate to within the expected variance as calculated from the Fisher information matrix.

To evaluate the accuracy of using a patterned fit model that knew of the true emitter positions, we calculate the Bayesian information criterion

$$\mathrm{BIC} = -2 \cdot \ln \mathcal{L} + N_\theta \cdot \ln N_k$$

where $\mathcal{L}$ is the likelihood function evaluated at the maximized parameter values, N_θ is the number of estimated parameters in the model function (three for each PSF used plus one for the background), and N_k is the number of data points (number of pixels). Because

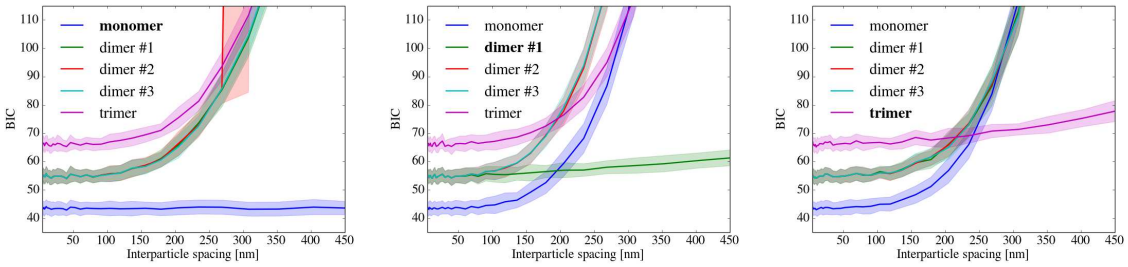

(A) Monomer (B) Dimer confiuration #1 (C) Trimer

FIGURE 4.6. Model selection for SR under TEM correlation conditions. The bold line shows the mean of 10,000 fits and the shaded region represents the standard deviation of the BIC around those mean values.

additional PSFs increase the number of free parameters, the value of the likelihood function alone should not be used to compare different models.

Figure 4.6 shows the accuracy of the models in terms of the BIC as a function of interparticle separation distance. The smaller the BIC value, the more likely the model is valid. In the case of a one emitter, Figure 4.6A shows that a PSF of only a single emitter (monomer) will always be the best model of choice—a relieving result. The cases of a dimer or trimer, Figure 4.6B and Figure 4.6C, respectively, show more interesting behavior. In both cases, the true model function only becomes the most likely for separation distances larger than $\sim$ 200–250 nm, and the single PSF model is the best choice for smaller distances. A similar behavior also results from direct likelihood comparisons.

The signal and noise levels are the primary experimental characteristics that can be improved to produce more accurate fits. Because the fluorescence measurements for correlated SEM experiments had inferior SNR than the TIRF instrument was, in theory, capable of achieving, a study replicating the best achievable conditions demonstrates if such methods are useful for disentangling the fluorescence signals from SR measurements of NC clusters. Figure 4.7 shows the model selection results from simulated ideal TIRF conditions. Because of the improved SNR, the correct model selections occur at smaller separation distances,

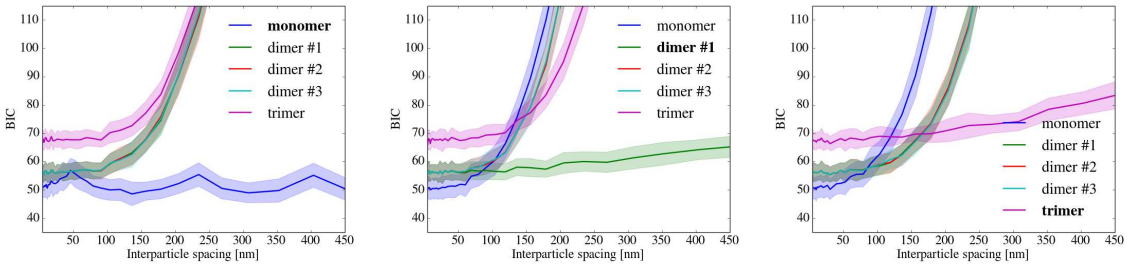

(A) Monomer (B) Dimer configuration #1 (C) Trimer

FIGURE 4.7. Model selection for SR under best case scenario TIRF conditions.

which is most significant for the dimer. Hence, the patterned PSF approach, even under the best experimental conditions, will not be able to identify the correct model for the separation distances necessary for NC cluster studies. Most blind multi-emitter deconvolution algorithms are based on similar operating principles and it is clear from these simulations that they cannot achieve the $\sim$ 10 nm feature identification required for analysis of small NC clusters.

4.3.2. INDEPENDENT COMPONENT ANALYSIS. From signal processing comes an alternative approach to isolating the PSFs of the individual emitters. Independent component analysis (ICA) is a method of sorting out multiple signal sources provided there are multiple measurements of the signal that are correlated in time and corrupted by some mixing matrix. Conceptually, ICA is often described by the cocktail party metaphor. Imagine a cocktail party where there are multiple groups of people, each having their own conversation. It would be difficult to follow any one particular conversation if you stood in one place. However, if you recorded the entire scene from multiple vantage points and compared the signals, the individual conversations would be present as common fluctuations within each recording at different volume levels. Applying this concept to SR imaging, the individual blinking behavior of the NCs are the time fluctuations of each conversation, the multiple

recordings are the individual pixels that make up the image, and the various volume levels are represented as the intensity modulations of the PSFs.

Mathematically, ICA solves the problem of determining the mixing matrix $\mathbf{A}$ in the equation $\mathbf{x} = \mathbf{As}$ where $\mathbf{x}$ is the time-series of the observations, $\mathbf{s}$ is the time-series of the sources, and $\mathbf{A}$ is the mixing matrix that encodes information about the strength of the signals at each observation point and the system noise. Only the observations are known. After deconvolution, the mixing matrix $\mathbf{A}$ will contain the spatial distributions of the PSFs for each emitter and $\mathbf{s}$ the time trace of the blinking events for each emitter. ICA approaches the deconvolution by maximizing the measure of the non-Gaussianity of the sources. This requires the individual signals not be Gaussian distributed. Binary NC blinking satisfies this requirement as the fluctuations of each source are between two intensities (two Poisson distributed states, one the on-state, the other the off-state, or noise), not a Gaussian distribution of intensities. Details of the ICA algorithm can be found in the works of Hyvarinen[140] and Lidke *et al.*[141].

The multi-emitter problem using ICA has been studied before in the context of localizing NCs[141, 142]. However, no EM imaging was available to verify the analyses against experimental data. In these approaches, the resulting mixing matrix $\mathbf{A}$ obtained by examining movies of blinking NCs in close proximity was used to extract the PSFs from each NC, followed by SR fitting to determine the location of the unmixed source PSFs individually. Accuracies down to $\sim$ 25 mn were reported for non-interacting NCs—within the range of the inter-particle spacing of some medium-sized NC clusters. In the study by Lidke *et al.* blinking was simulated by sampling a uniform distribution. In an effort to see the applicability of these analysis method to NC clusters, we simulated the conditions for the TIRF experiments and incorporated the power-law blinking distributions to further validate the

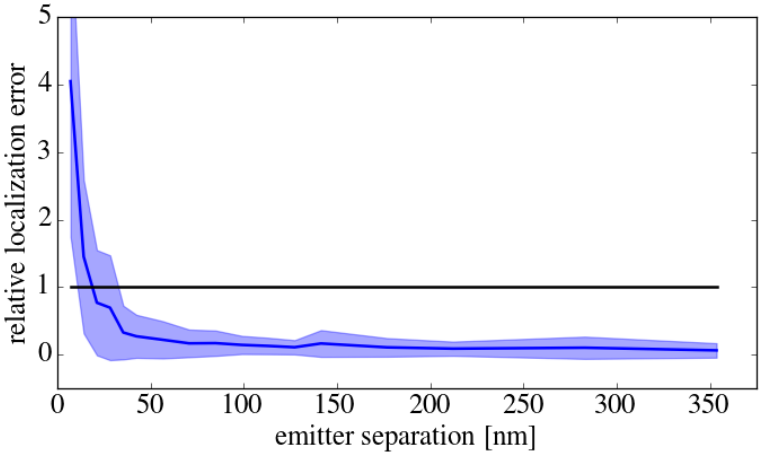

FIGURE 4.8. ICA localization accuracy with simulated data. Simulated data was based on a background of 10 photons and 1,000 photons in the PSF. A relative localization error of 1 indicates the deviation of the fits from the true positions was equal to the magnitude of the separation distance.

ICA method in the context of real NCs. To compare results, the relative localization error of two emitters was calculated according to

$$\varepsilon = \frac{\left|\mathbf{P}^{(1)}_{\text{true}} - \mathbf{P}^{(1)}_{\text{fit}}\right| + \left|\mathbf{P}^{(2)}_{\text{true}} - \mathbf{P}^{(2)}_{\text{fit}}\right|}{2\left|\mathbf{P}^{(1)}_{\text{true}} - \mathbf{P}^{(2)}_{\text{true}}\right|}$$

where $\mathbf{P}^{(i)}_{\text{true}}$ is the true location vector of the i^{th} emitter and $\mathbf{P}^{(i)}_{\text{fit}}$ is the location vector determined by SR fitting.

Figure 4.8 shows the results from simulations done in a similar manner as the patterned PSF simulations above. Only two NC were simulated in the blinking movies. A benefit of ICA is that it removes the noise components in the separation process and the effects of noise models in SR analysis are less significant. ICA is able to effectively separate signals at distances down to 50 nm without any appreciable localization error—a significant improvement over the patterned model PSFs method. Relatively good localization down to ~ 25 nm can be obtained with this method.

Examination of the individual PSFs at small separation distances shows that the source of the localization error increase is deformation of the PSFs when there is sufficient overlap. The deviations from ideal PSFs are primarily in the gap region between the emitters. There is an apparent minimal distance within the range of 25–50 nm that, as the separation distances decrease, the overlapping regions of the PSFs cannot be isolated to one emitter or the other and the effect is that the signal is not correctly assigned to either emitter and may appear in the noise terms of the mixing matrix. An alternative SR fitting model may improve localization accuracy if it considers the degree of distortion that ICA generates at small distances among all extracted PSFs. Because noise is largely removed with ICA, PSFs match surprisingly well to the ideal model functions (the pixel-integrated Gaussian, in these simulations) and the deviations are clear. Additional work with ICA of this sort could improve the resolvable distances. Furthermore, because NC clusters can include multiple acceptor regions separated by more than a single NC diameter (discussed in detail in Chapter 6), ICA could provide information in medium- and large-sized clusters. Particularly for experiments where EM correlation cannot be obtained, ICA provides the potential for supplementing such measurements. Another approach similar to ICA is the iterative non-negative matrix factorization (iNMF) of Mandula *et al.*[143, 144]. iNMF and other fluctuation-based algorithms[135, 145, 139] are worth exploring as alternatives to pure SR fitting.

CHAPTER 5

Lifetime and Spectral Studies of Nanocrystal Clusters

As a preliminary study of the NC clusters that have been clustered in various ways, and to gain insight from the spectral measurement techniques, clusters of thick- and thin-shell NCs were examined with the confocal fluorescence microscope described in Section 4.1. Details of the cluster synthesis method and the sample preparation can be found in Appendix A. Time-resolved lifetime measurements in conjunction with measurements of the spectral dynamics of the clusters reveals several features of ET and collective behavior that have not been previously reported. The approximate size and type of the clusters have to be inferred based on their preparation method and source solution because no independent structural verification was done for these measurements. However, the EM characterization studies detailed in Section 3.3 apply to the batches that served as samples for this chapter and the physical manifestation should be considered in view of the EM studies. Section 5.1 presents lifetime data in line with previous works[21, 22] and Section 5.2 expands our understanding of NCs and NC clusters by introducing new data that examines the spectral signatures of the samples.

The experimental work was carried out by myself and Dr. Roy Geiss, and Dr. Alan Van Orden and Dr. Martin Gelfand directed the work and provided theoretical considerations. This preliminary work is currently unpublished.

5.1. Lifetime-intensity Observations

A common measurement for fluorescent molecules is to examine the lifetime characteristics of individual emitters. With time-resolved measurements, histograms of the decay times can be compiled and fit to a single decay function or to multiple decay functions. Because the lifetimes of NCs are tens of nanoseconds and ET rates can be an order of magnitude faster, the decay histograms must be deconvolved with an IRF which could otherwise introduce artifacts involving short lifetime components and several methods of to do so have been published[146, 147]. The entire measurement involving all photon events may be analyzed to obtain the principle lifetime components. However, a more informative measurement breaks the photon stream into bins of fixed duration (typically 1–100 ms) and examines the time-resolved records of only the photons within that bin. When combined with the total photon count for the bin, these measurements form the basis of the fluorescence lifetime-intensity distribution (FLID). Because the bins contain significantly fewer photons to fit a decay lifetime to and fluorescence decay is a Poisson process for which there is a simple likelihood function, MLE fitting results in accurate parameter estimates. In previous studies of NC clusters, the effect of ET was manifest as a short lifetime component in addition to the intrinsic fluorescence lifetime[84, 21, 148]. To capture such dynamics and avoid over-fitting, bi-exponential decay functions were used to calculate FLIDs. In a commonly used analysis method, the average lifetime of the two exponentials was used to generate FLIDs and the amplitude fit parameters weight the contribution of each time-bin to the FLID histogram. In this presentation, the projection of a FLID onto the intensity axis does not necessarily match the simple intensity distribution. Other FLID formation approaches may highlight other aspects of the lifetime-intensity relationship, but all generally present the same information.

Figure 5.1 depicts several types of FLIDs that can occur. A single NC, such as the one shown in Figure 5.1A, has a well-defined lifetime at a well-defined intensity level. Both the thick- and thin-shell NCs had fluorescence lifetimes of $\sim$ 30 ns, which is expected because fluorescence lifetime is, most generally, an intrinsic property of the material and the cores are the same (size and material) for both NC types. Detection events during off-durations are mostly noise, which is randomly distributed. Because they are not fit well by an exponential decay, such bins with insufficient photons to overcome the SNR are not plotted. Hence, only a single feature appears in the FLID of this NC representing the on-state. When multiple, non-clustered and non-interacting NCs are in the single-molecule detection volume, this single feature is broadened in intensity, but not in lifetime, as shown in Figure 5.1B. Hence, the lifetime is independent of the intensity. Examples of single NCs that demonstrate the distribution of lifetime features are given in Figure C.1. The CdSe/ZnS NCs used in this study had a distribution of lifetimes between 20–30 ns.

Grey states, described initially in Section 2.2, can appear in FLIDs of single NCs as additional well-defined features similar to the intrinsic lifetime/intensity feature. A charged NC is responsible for grey states and they manifest in FLIDs as additional low-intensity, short-lifetime features. The work of Galland *et al.*[78] demonstrates the representation of these features, where access to the grey states was electrochemically controlled. Excitation power studies by Yoshikawa *et al.*[83] show the relative intensities of the on state and the grey states are fixed for a given NC, but the probability of accessing the grey states is strongly dependent on the excitation power, essentially dependent on the average occupancy of the excited state. As shown in Figure 2.3 for excitation at 450 nm, grey states were observed in these NCs, although they do not occur as frequently as the on- or off-intensities of binary blinking. The low occurrence of grey states in these time-resolved measurements is due to

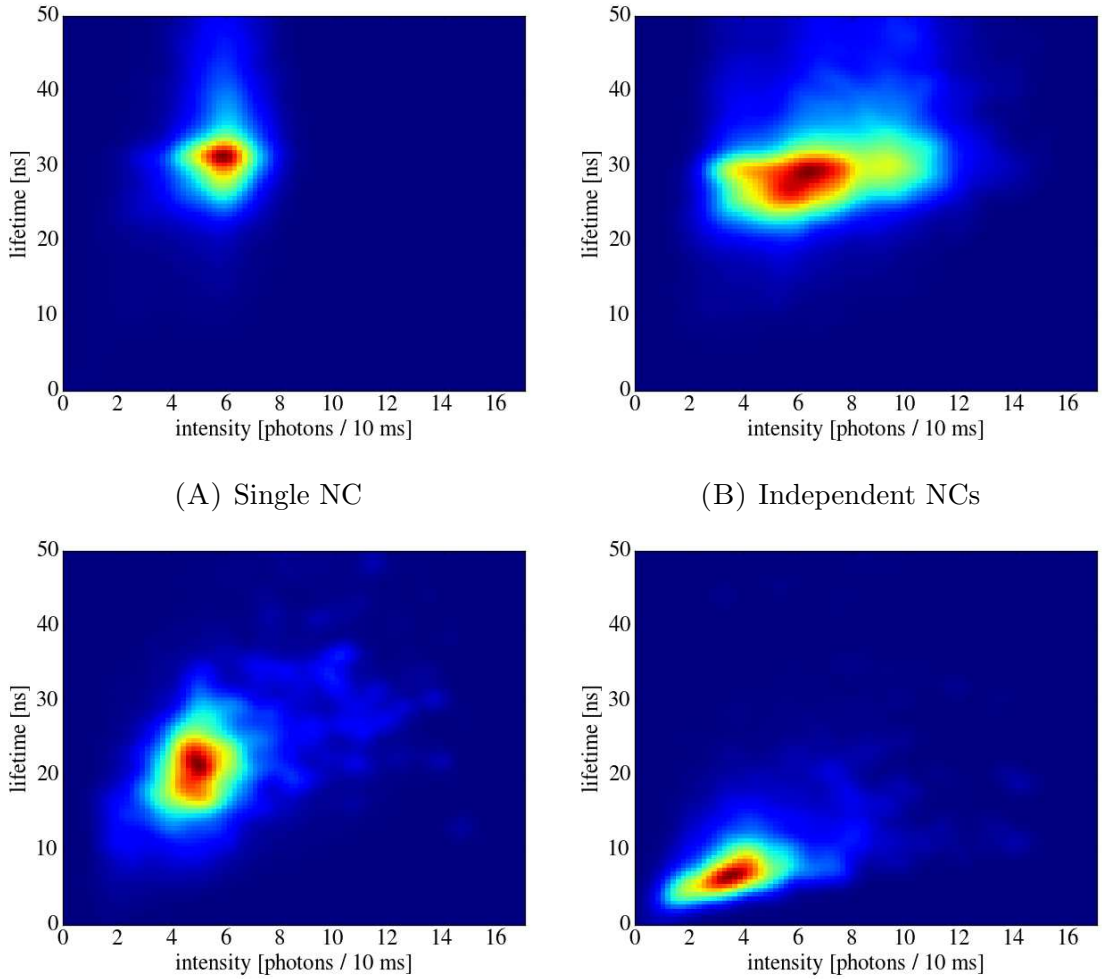

(A) Single NC

(B) Independent NCs

(C) Cluster of thick-shell NCs

(D) Cluster of thin-shell NCs

FIGURE 5.1. FlIDs of different sample types. The cluster from thick-shell NCs was from the rapid clustering procedure and UC separation while the cluster from thin-shell NCs was the result of slow MeOH clustering. Each FLID was calculated from 50 ms binned photon streams and fit to a bi-exponential decay. 1,000 seconds of data were used for each measurement. The histograms were smoothed by a 2 bin Gaussian kernel for display.

the low excitation flux: the probability of generating an exciton during these measurements was $\langle \mathrm{N} \rangle_{450\ \mathrm{nm}} = 1.7 \times 10^{-3}$ excitons/pulse (see Appendix B).

FLIDs from NC clusters can signify that ET processes are present. The FLID for a thick-shell NC cluster is shown in Figure 5.1C. As opposed to the multiple non-interacting NCs case, the cluster exhibits a feature where lower intensities are correlated with shorter

lifetimes than the intrinsic lifetime of NCs. There is a dependence of the lifetime on the intensity. This effect is even more pronounced for the thin-shell NC cluster in Figure 5.1D. Such correlations have been identified as indicators of ET in the work by Shepherd *et al.*[84]. Because ET and fluorescence decay are competing processes for excitons, a donor NC in a cluster may emit a photon instead of transferring the exciton to an acceptor NC. Emission from donor NCs occurs with lower yield than the intrinsic QY of the particles and lifetimes are quenched because of the competing non-radiative rate. Donor emission is most prominent when acceptor NCs are in their off-states and do not overwhelm the decay curve with the intrinsic lifetime. Minor intensity fluctuations or blinking in donors convolved with those of acceptors result in the distribution of lifetimes and intensities that appear in FLIDs of NC clusters. These signatures of ET are different from those that are produced by grey states. A grey state is a feature with well-defined yield and lifetime and ET is a distribution that has a positive correlation between the lifetime and intensity.

The difference between the FLIDs of thick-shell clusters and thin-shell clusters can be understood in the context of ET. ET is very sensitive to the inter-particle separation distances: FRET has a $1/r^6$ dependence and DET is an exponential decay. The range for FRET reported by Mork *et al.*[94] is $\sim$ 8–9 nm, aligning perfectly with the characterized nearest-neighbor separation resulting from thick-shell clusters (see Table 3.1). Therefore, the thick-shell samples produce clusters with less efficient ET. Clusters containing thin-shell NCs have shorter separation distances and will exhibit more efficient ET. The ET features for thin-shell NCs deviate more significantly from the multiple non-interacting situation because of the difference of ET efficiency. Figure C.3 illustrates the variety of unique FLIDs that can be measured from NC clusters.

Another factor of the clustering process that can affect the ET efficiency is the relative orientations of the NCs. As observed in the TEM characterization of rapidly clustered NCs, the orientation between particles is random for that preparation method. Where the thick-shell cluster of Figure 5.1C was from a rapidly clustered UC batch, the thin-shell cluster in Figure 5.1D is the result of the slow clustering procedure for which there is no TEM characterization of the orientation correlations. The degree to which spacing or orientation has a greater effect on ET efficiency within clusters cannot be distilled from this preliminary study of different samples and preparation methods, and remains a direction for future work. These time-resolved measurements further support the ET behavior of clusters that has been proposed in previous works.

5.2. Spectral Behavior

Previous single-molecule spectral measurements of individual NCs revealed the emission spectrum to be dynamic and not static[32, 149–151]. Spectral shifts of 10 meV ($\sim$ 2.5 nm for the emission range of the 565 nm NCs) have been observed in low temperature measurements[32] and at room temperature shifts as large as 100 meV have been reported[151]. Figure 5.2 illustrates the spectral diffusion of a single thick-sell NC obtained by monitoring the relative detector rates split by a dichroic beam splitter in the confocal setup. The spectral motion can occur following a blinking event, as a sudden and discrete change, or as a drift over time, and this NC exhibits all types of motion during the trace. While some studies have observed a prolonged unidirectional spectral drift as measurements progress[34]—a blueing attributed to the oxidation of the CdSe core—the spectral trajectory of the thick-shell NCs in this study did not exhibit any long term drifts. Spectral motion is attributed to the redistribution of charges in the local environment[152], internal reordering,

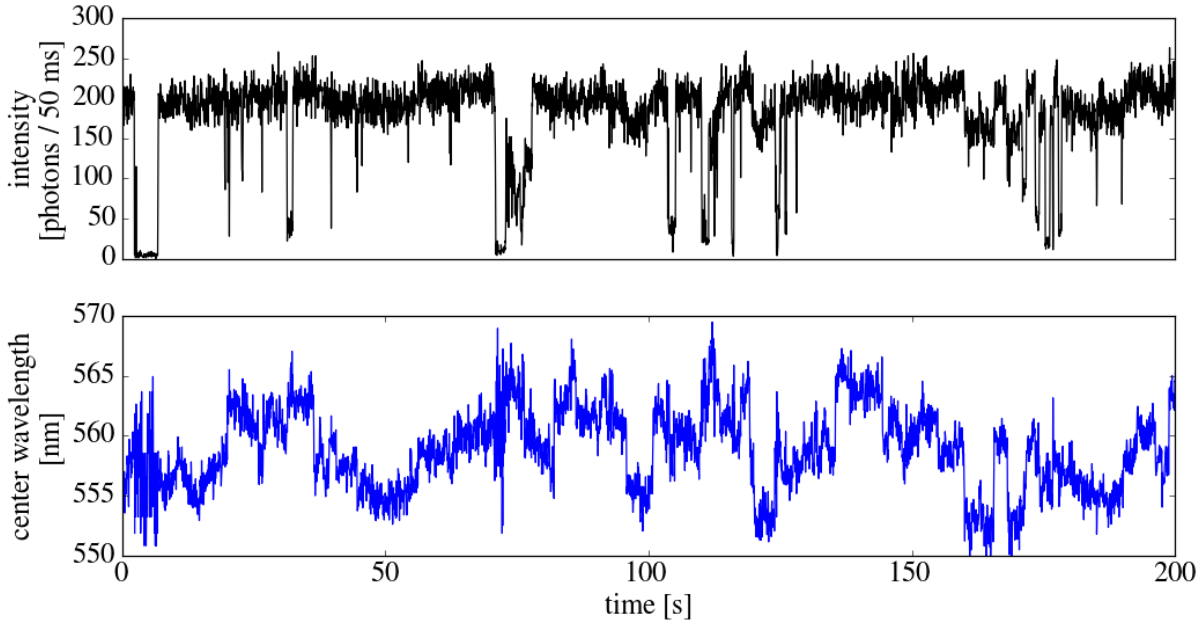

FIGURE 5.2. Time traces of intensity and spectra for single thick-shell NC. Some spectral jumps are correlated with blinking events; however, not all spectral motion is correlated with an intensity change.

and NC charging[153]. Light-induced spectral diffusion has been suggested as a source of the spectral broadening at low temperatures[154]. Of particular note is that some blinking theories rely on spectral diffusion to explain the distributions of on- and off-durations[76].

Spectral diffusion can present differently for a NC cluster. Figure 5.3 shows the fluorescence intensity and spectral time traces for the thick-shell NC cluster of Figure 5.1C. The traces are well correlated in time and the random fluctuations observed in the single NC appear suppressed. It should be noted that these traces represent highly correlated spectral and intensity features and many clusters studied did not exhibit such substantial correlation. However, in general, spectral traces from NC clusters showed higher degrees of correlation with intensity than single NCs.

Theories used to explain the spectral fluctuations in single NCs may also suggest an explanation for the reduced fluctuations in NC clusters. Türck *et al.*[152] indicated that

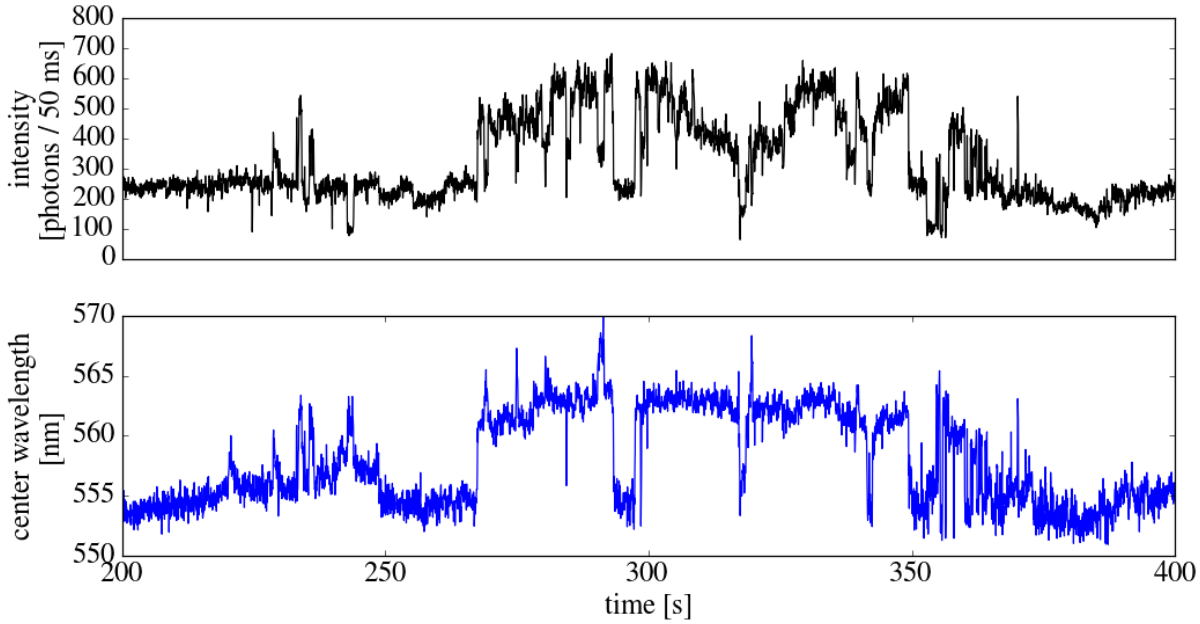

FIGURE 5.3. Time traces of intensity and spectra for a thick-shell NC cluster. Spectral motion is highly correlated with intensity fluctuations.

random field fluctuations due to the embedding environment are responsible for the spectral diffusion in CdSe NCs. A quantum-confined Stark effect can be induced in NCs by external electric fields[155] and exciton polarization from a constantly changing environment results in spectral diffusion[156]. NC clusters represent a different local environment where neighboring NCs may provide stability to the random environmental fluctuations. Since individual thick-shell NCs consistently demonstrate strong spectral diffusion, the thick-shells protecting the core from random fluctuations in the local electrostatic environment cannot explain the suppression in clusters. However, occupying a fraction of the surface through attachment, neighboring NCs may suppress spectral diffusion by shielding the embedding environment. Unfortunately, these experiments do not directly give information about the mechanism.

Another informative way of examining the intensity and spectral relationship is to construct spectral-intensity distributions (SIDs). Analogously with FLIDs, SIDs are generated from binned trajectories of the spectral and fluorescence intensity information. Presenting

them as scatter plots instead of histograms also aids recognizing subtle features. Figure 5.4 shows SIDs for the same NCs represented in Figure 5.1. The SID for a single NC, Figure 5.4A, is as simple as its FLID counterpart: primarily a single feature that corresponds to a well-defined intensity and central wavelength. Although the batch of NCs is ideally monodisperse, spectral variation between NCs was observed with individual NCs exhibiting emission wavelengths spanning 550–570 nm. Figure C.2 provides additional examples of single NCs with unique spectral signatures.

Multiple non-interacting NCs produce more complicated SIDs, but they can be easily understood. In Figure 5.4B the spectral signatures of multiple NCs as they appear in a SID are apparent. Where the FLID provides no explicit indication of the number of independent NCs measured, the SID suggests two NCs were present in the focal volume: one with emission centered around 567 nm and the other with emission centered around 555 nm. A grey state is likely observed for the 555 nm particle. That the SID suggests there are probably two NCs is because two well-defined features of approximately the same intensity are present (the QYs for single NCs from this batch were relatively homogeneous). The grey state of the shorter wavelength NC has the same center wavelength, a characteristic observed in other single NCs with clear grey states. Each NC produces its own feature when the other NC is in its off-state. Finally, a feature broadly distributed in intensity at $\sim$ 561 nm is the product of both NCs emitting and the spectral position is the average of the two. A lower intensity side-lobe at $\sim$ 563 nm is likely due to the spectral averaging involving the grey state of the shorter wavelength NC. These features are broader in intensity than the features of the individual NCs because they are the sum of two independently distributed signals. While this example suggests two NCs, in general, such explicit counting of the number of particles can be difficult, particularly when there is more substantial spectral overlap.

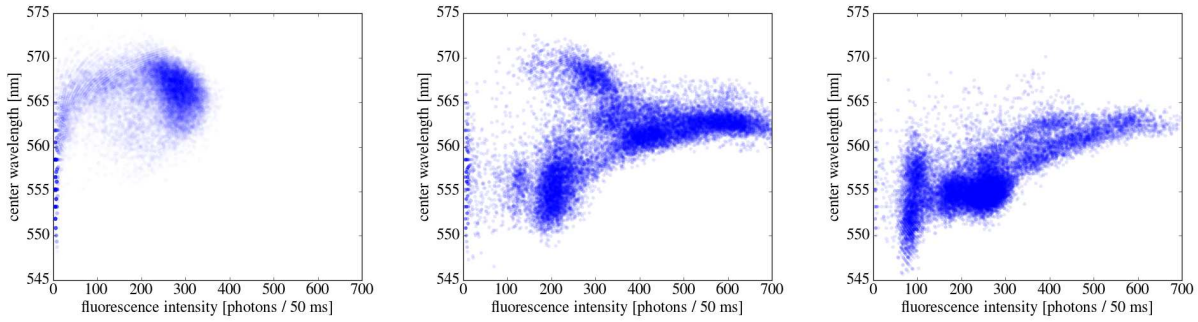

(A) Single NC (B) Independent NCs (C) Cluster of thick-shell NCs

FIGURE 5.4. SIDs of the same NCs whose FLIDs are shown in Figure 5.1. ET features appear in the cluster SID while the multiple non-interacting NCs do not, which display an averaged feature. The intensity distributions appear different from their counterparts in the FLIDs because SIDs were generated from the raw photon rate data and the histograms of FLIDs are compiled from distributions weighted by the fit parameters. Additional examples demonstrating the variety of unique spectral signatures from NCs and NC clusters exhibiting ET can be found in Figure C.2 and Figure C.4, respectively.

ET from NC clusters produce clear features in SIDs. Figure 5.4C shows the SID of the thick-shell cluster. While strikingly similar to the two NC SID discussed previously, the cluster SID is clearly missing the longer wavelength feature that would have an intensity comparable to the QYs of individual NCs. The longest wavelength feature corresponds to the brightest intensities emitted by the cluster and is comparable to the that of multiple NCs contributing to the signal. This long wavelength feature is the emission from the acceptor NC in the cluster. Because ET drives excitons to the smallest band gap NC, the majority of the emission will emanate from the longest wavelength NC—the acceptor. Furthermore, the intensity of the acceptor is enhanced by the contributions from donor NCs, resulting in a distribution of higher intensities than a single NC would typically produce. When the acceptor NC is in an off-state, the spectral features of the donor NCs at shorter wavelengths are apparent. These SID features are different from the multiple NC case because of the distinct lack of a low intensity, long wavelength feature. The higher intensity features in Figure 5.4B are the result of emission from multiple sources averaged together. However, no

long wavelength features are present to be averaged in the cluster example except for the enhanced emission at the longest wavelength.

An interesting consideration for examining the fluorescence lifetimes in a split detector arrangement concerns rise-times and ET. With the split detector arrangement, correlated time-resolved and spectral measurements are obtained simultaneously. However, samples that exhibit ET produce a rise-time in the red-channel detector. This is because excitons arrive at an acceptor at delayed times as the transfer process requires a finite amount of time to occur. As a result, careful fitting and lifetime analysis must be done when extracting decay curves from the separate red- and blue-channels. This artifact is also the primary source of the different appearances of the intensity components between FLIDs and SIDs of the same NC. FLIDs are constructed from fitted parameters and the rise-times of the red-channel produce exponential decays with negative amplitudes, affecting the weighting in the histogram. A third exponential is sometimes necessary to accommodate the rise-time which must be factored into the analysis approach. However, extracting both lifetime and spectral measurements can be useful, particularly because correlations between lifetime changes and spectral jumps have been reported[157] and may be of interest for future NC cluster studies.

The simultaneous measurements of lifetime and spectral signatures differentiate single NCs from NC clusters in ways not previously observed. In particular, the spectral diffusion of single NCs is suppressed in clusters. While further studies may reveal the details of the mechanisms involved, this experiment is the first observation to indicate such behavior and suggests that NCs in clusters exist in a more stable electrostatic environment than NCs in isolation. Spectral measurements also produce signatures that validate the ET model of donor/acceptor relationships. While a short lifetime component has previously been the sole indicator of ET in clusters, the spectral features show clear relationships between intensity

and emission wavelength in agreement with ET: the highest intensity emission in clusters is a longer wavelength than the lower intensity emission, a consequence of ET to smaller band gap NCs. Furthermore, suppressed spectral dynamics and clear spectral-intensity relationships suggest donor/acceptor roles are fixed in clusters despite the magnitude of spectral diffusion in single NCs.

CHAPTER 6

Correlated SEM and Super-resolution Microscopy of Nanoscrystal Clusters

To better understand the connections between the fluorescence behavior of NC clusters and their physical structure, independent measurements of each must be made. Up until this point, the form of the clusters studied had to be implied from fluorescence measurements alone. The variety of geometries, orientations, and inter-particle separation distances means that clusters may have very efficient ET, in which case donor NCs may hardly present a signal above the dominant acceptor, or ET may be inefficient resulting in signals from individual NCs that are effectively isolated giving the appearance of multiple unattached NCs. Previous work utilizing correlated fluorescence microscopy with atomic force microscopy could identify large clusters and indicate if multiple NCs were present in the focal volume, but not provide the resolution necessary to determine exact geometries[21, 22].

Studies combining EM imaging with fluorescence microscopy primarily utilize the fluorescence measurements to determine QY in correlation with defects and identify anomalous blinking behavior in single emitters[17–20]. Linking the fluorescence behavior of aggregates spanning dimers to hundreds of nanoparticles with verified by TEM imaging was reported by Wang *et al.*[158, 159]; however, these studies concerned general intensity fluctuations and were not well-resolved spatially. The work of Weber *et al.*[160] reported on the correlated surface-enhanced Raman scattering with SEM imaging of large aggregated silver colloids, and was among the first applications of correlated SR and EM measurements on clusters of nano-sized particles. However, the size of the silver colloids were an order a magnitude

larger than the NCs of this work and the measurements were looking for surface activity over length scales larger than the small clusters studied here.

In this chapter, we present the results from correlated super-resolution microscopy and SEM imaging on NCs and NC clusters. This work represents the first such combined measurements for NC clusters and introduces new approaches to studying ET with single-molecule methods. The experiental work was carried out by myself, Dr. Peter Goodwin, and Chris Sheehan at the Center of Integrated Nanotechnologies (CINT) at Los Alamos National Laboratory, with Dr. Alan Van Orden and Dr. Martin Gelfand directing the project and theoretical work. A published initial report of the findings appeared in *Proceedings of SPIE*[161] and a more extensive manuscript is currently under review.

6.1. Experimental Design

The primary difficulties in obtaining correlated measurements with two significantly different imaging modalities are (1) preparing samples that can be imaged in both instruments, and (2) to identify the same features of interest between the two measurements. It is, therefore, necessary to perform SR measurements on a sample substrate that can be imaged in the SEM and generate fluorescence maps in order to facilitate finding the NCs in the SEM. Ideal substrates for fluorescence microscopy are glass coverslips and for EM imaging copper grids. However, copper grids (or any material that promotes ET to the substrate) can quench fluorescence needed for SR localization and glass coverslips do not enable high-resolution EM imaging because of surface charging. These requirements limited the available sample substrates to thin windowed grids of silicon nitride (see Appendix A). Once a set of fluorescence measurements is completed, the sample substrate is unmounted from the TIRF microscope and transferred to an SEM for electron imaging.

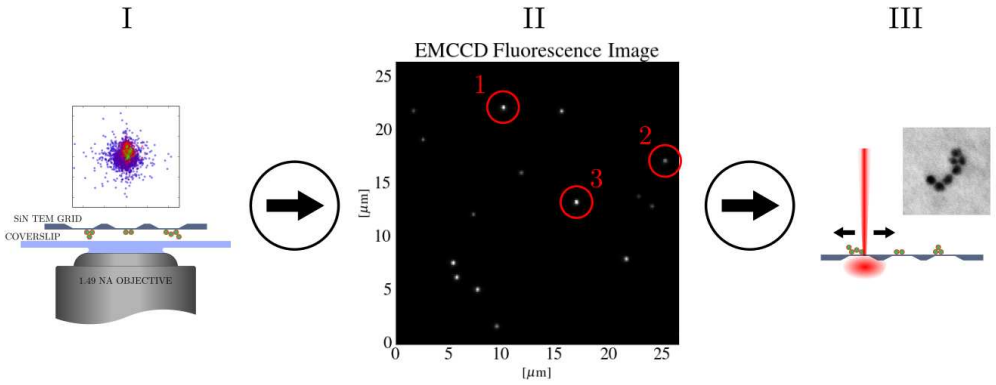

FIGURE 6.1. Correlation scheme. Fluorescence measurements on the TIRF microscope are performed first. Emission centers of interest are identified and a table of the locations are compiled referencing the NC coordinates to the edges of the SiN grid windows. Finally, the coordinates are used to locate the NCs in an SEM where the structure and geometry are measured.

Figure 6.1 illustrates the method used to obtain correlated measurements. Samples of NCs or NC clusters are deposited onto windowed SiN TEM grids. The substate is placed with the exposed surface of deposition facing the top of the TIRF microscope on top of a mounted coverslip. In this arrangement there is a small gap of air between the glass coverslip and the surface of the SiN. This gap alters the TIRF conditions at the coverslip interface. While lower SNRs measurements were achieved in these correlated experiments utilizing the SiN grid, it is not clear if the air gap affecting the TIRF condition, reflection at the air-SiN interface, or autofluorescence from within the SiN itself contributed most significantly to the reduced SNRs. However, fluorescence signals were strong enough for SR imaging. Movies with dozens of fluorescing NCs in the field of view were obtained under 488 nm CW illumination at 185 W/cm^2 and the EMCCD imaged with an exposure of 100 ms/frame. 10,000 frames were collected for each measurement in order to sample as many blinking transitions as is feasible.

Location maps of the NCs positions were compiled after fluorescence measurements where the particle locations were referenced relative to the hard edges of the SiN windows. Because

of the small size of the NCs studied here, SEM imaging only clearly indicates a particle at high magnifications and the location maps needed to be accurate to within a couple hundred nanometers. Over the course of EM imaging, non-emissive NCs were sometimes found where no fluorescence appeared in the maps, underscoring the need to accurately label the locations of interest in correlated measurements so that NCs were not misidentified. Some studies have used marked substrates where particles could be located relative to large structures such as printed electrodes or large polystyrene beads. The approach taken here was sufficient for SEM correlation because many SEM instruments have sophisticated position indexing that track absolute locations of the sample across large distances and magnifications. However, TEM imaging is difficult to use here because fields of views as large as 40 μm and sparsely populated NCs with feature sizes as small as 5–10 nm make finding the particles difficult. Position indexing for TEM instruments is implemented differently than most SEMs because they are imaging devices and precise calibration between high- and low-magnification can be tricky. For this experiment STEM-in-SEM measurements were done using a Magellan 400 XHR-SEM operating at 30 kV and 0.2 nA.

6.2. Analysis

Because the localization accuracy required for these correlated experiments is near the limit of what can be obtained from SR methods, multiple analysis approaches were compared for verification. Two algorithms were primarily used because they each represent a different approach to localization. ThunderSTORM[162] is an ImageJ plugin that uses MLE to fit a variety of analytical PSFs to image data. For this data set the pixel-integrated Gaussian was used as a PSF model. It should be noted that ThunderSTORM does not consider the EMCCD gain in the noise model. While it is a parameter, the algorithm only makes use

of it to convert raw image data into photon counts and in the calculation of uncertainty for which there is an additional factor from excess noise introduced by EMCCD cameras. As an alternative SR algorithm, DAOSTORM[126] was also used to analyze the image data from the correlated experiment. DAOSTORM uses an experimentally characterized PSF derived from image data as a model to accommodate the deviations from an ideal Gaussian PSF. The gain from EMCCDs is not considered in the DAOSTORM algorithm either. Both ThunderSTORM and DAOSTORM have methods to automatically treat closely spaced emitters. However, Section 4.3 demonstrates model-based approaches to the multiple emitter problem cannot resolve the individual NCs for separation distances found in the NC clusters and the emitter densities were otherwise sparse enough that emission from neighboring NCs were well separated and did not bias localizations from adjacent emitters.

The results from both algorithms were further processed to remove stage drift using the ThunderSTORM fiducial-based drift correction feature. Drifts of ~ 1.5 pixels (150 nm) over the duration of a measurement were typical. Examining the position trajectories of known single NCs within the field of view verifies the accuracy of the drift correction and addresses concerns about bias introduced through position jumps from NC clusters that were used as fiducial markers for the correction.

As discussed by Engelhardt *et al.*[123], dipole effects can result in inaccurate SR localizations. While a dipole-based SR method could be applied to the data set from the correlated experiments, it was found that such models were not necessary and likely were not accurate representations of the PSFs produced by the imaging system. Defocused imaging of the correlated samples showed symmetric diffraction patterns, which is not expected from emitters known to have such strong dipole effects[163–166]. Furthermore, examination of the PSF residuals from the DAOSTORM analysis indicated general symmetry that was not present

for NCs or NC clusters deposited directly onto glass coverslips (see Figure D.1). Because these observations only occur for samples deposited on SiN grids, it is suspected that the unconventional substrate arrangement renders dipole effects irrelevant for these measurements. The presence of the air gap placing the NCs several hundred nanometers above the ideal coverslip-air imaging interface and the two SiN surfaces from which reflection occurs (the grid windows were 10 nm thick and semitransparent in the optical range) are possible contributors to the symmetry effect. Near-field reflected emission superimposed on the regular emission is likely the most dominating effect. As additional verification that dipole emission does not introduce localization bias, some spots from the correlated measurements were analyzed with a custom implementation of a dipole orientation algorithm. The resulting orientation angles from a single NC and a NC cluster were uniformly distributed, reflecting no dominant dipole effect and that noise primarily contributes to the variability of orientation fitting in these data sets. Furthermore, no significant between ThunderSTORM, DAOSTORM, and the dipole analysis was observed in the SR localizations: all methods resulted in similar position measurements. The SR results presented in this chapter are from the DAOSTORM algorithm as a matter of preference. See Appendix D for detailed discussions of dipole effects in SR imaging as observed under these experimental conditions.

6.3. Intensity Scaling

From SEM imaging, the number of particles in each NC cluster can be correlated with the fluorescence properties of the cluster. One would expect that as the number of particles in a cluster increases, so would the rates of exciton generation and fluorescence. Because of blinking events, a NC cluster typically does not spend a significant amount of time in a configuration that produces the highest intensity (all NCs in their on-states). However,

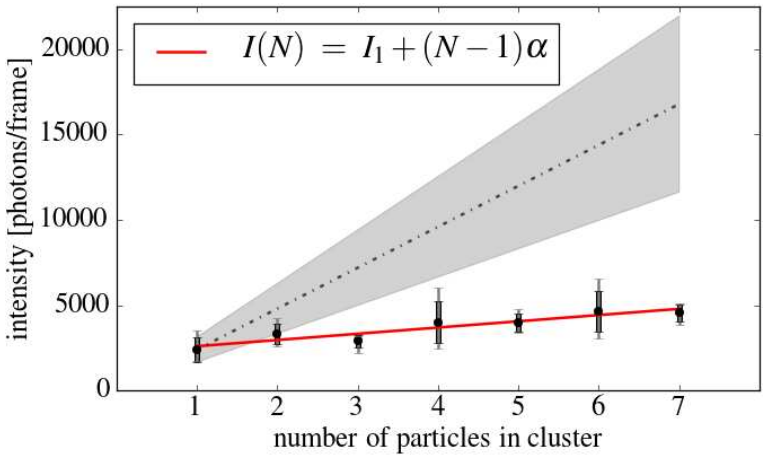

FIGURE 6.2. Intensity scaling of thick-shell clusters as a function of the number of NCs in the cluster. The standard deviations are indicated by solid black marks and the minimum/maximum intensities of the set by a grey line. The dashed line indicates the projection of a simple linear scaling where $I(N) = I_1 N$ and the grey shaded region represents the range such a scaling would produce given the distribution of single NC intensities measured. Fitting the measured scaling to the linear function $I(N) = I_1 + (N-1)\alpha$ yields the parameters $I_1 = 2590$ and $\alpha = 370$, where I_1 represents the average intensity of a single NC and α the intensity increment an additional NC to a cluster would contribute.

intensity bursts are indicators of the maximum intensity that a cluster is able to achieve and the brightest intensity burst from a fluorescence trajectory was used as the best approximation of highest achievable yield from a cluster. Figure 6.2 presents the intensity scaling of thick-shell NC clusters as a function of the number of constituent particles. While clusters larger than a dimer have the additional complexity of geometry and shape that could impact overall yield, the intensity scaling was compiled considering the number of particles. Also plotted is the expected scaling if the maximum intensity of a NC cluster is simply proportional to the number of particles and the region of one standard deviation (based on the distribution of single NC intensities found in the same sample).

The intensity scaling deviates significantly from the projected simple linear dependence that would be anticipated if intensity is just the superposition of individual emitters. A linear

fit of the data suggests that every additional NC in a cluster contributes only $\sim 14\%$ of a single particle QY, resulting in large clusters that appear to have suppressed fluorescence despite the greater number of NCs to absorb and emit. It should be recognized that a dark fraction—a population of NCs that are never emissive—may contribute to the scaling observed. Depending on the synthesis quality, dark fractions of 2–50% have been reported. During formation, dark particles may be incorporated into clusters. However, the standard deviation of the intensities would be larger for clusters if a substantial dark population were being incorporated into clusters, and this is not the case. Recall that only emissive single NCs were used to determine the statistics of monomers in the scaling plot. Therefore, dark particles would produce broader distributions of maximum intensities in any cluster. In fact, the magnitude of the standard deviations does not appear to correlate with cluster size.

Similar scaling behavior is observed for measurements with slowly clustered thin-shell NCs. Figure 6.3 shows the intensity scaling for thin-shell NCs and the yield does not increase with a direct linear scaling to the number of NCs; rather, dimers and trimers produce lower yields than such scaling would imply. Interestingly, the slow clustering method produces a narrower distribution of cluster sizes for the process duration used (17.5 mins). Monomers, dimers, and trimers made up the majority of the cluster sizes for this preparation method. The distribution of single NC intensity, I_1, and the intensity increment per additional NC, α, were consistent with those of the thick-shells. However, the slowly clustered thin-shell NCs spent a significantly larger proportion of the time in their on-states: an average of 69% of the time for thin-shell clusters compared to an average of 7.3% of the time for thick-shell clusters. This behavior indicates that a thin-shell NC cluster was likely to have transitioned to the most emissive configuration and that it would be observed at some point over the course of a measurement. Because the scaling is similar between the two sample types, it

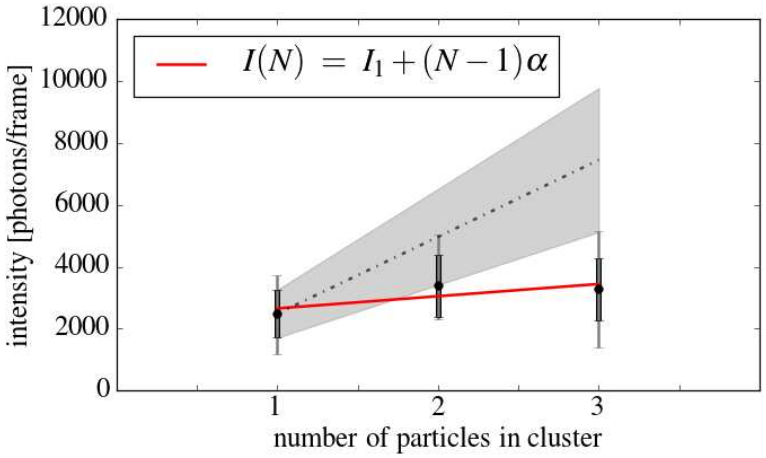

FIGURE 6.3. Intensity scaling of thin-shell clusters as a function of the number of NCs in the cluster. Fitting to the linear function $I(N) = I_1 + (N-1)\alpha$ yields the parameters $I_1 = 2650$ and $\alpha = 400$.

would appear that this behavior is not the primary reason for the intensity suppression for larger clusters.

6.4. SINGLE NANOCRYSTALS

Initially focusing on the SR analyses of single NCs provides a foundation of how to later interpret results from NC clusters. Figure 6.4 depicts the drift-corrected SR results of a single thick-shell NC along with the SEM verification. The SR localizations are displayed as a scatter plot with a point for each frame of the movie sequence in which the emission level was above a threshold value (marking the NC in an emitting on-state). Each localization is also color coded to the value of the intensity parameter from the SR fit. The scatter plot of a single NC is dominated by higher-intensity fits (green), which appear as a distribution about a single well-defined central location. This type of feature would seem obvious because the single NCs in this work exhibited primarily binary blinking behavior. The NC depicted in Figure 6.4 is representative of all single NCs correlated in these experiments.

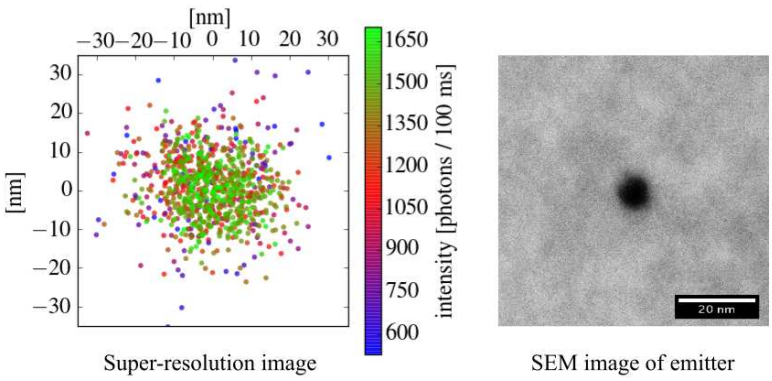

FIGURE 6.4. Super-resolution localizations of a single thick-shell NC correlated with SEM. The SR image and SEM image have the same distance scaling for direct comparison (SEM scale bar 20 nm). Color coding of the SR scatter plot indicates the intensity fit parameter corresponding to the particular localization. The standard deviations of the x- and y-coordinates are $\sigma_x = 11.2$ nm and $\sigma_y = 10.0$ nm, or $\sigma_{avg} = 10.6$ nm.

Because the off-states do not produce informative SR localizations, not every frame in the movie sequence is represented in SR results. For the specific NC in Figure 6.4, the fraction of time the NC was emitting was $\sim 9\%$ of the measurement corresponding to ~ 900 frames. Statistics from all thick-shell single NCs indicate these particles were in their on-states for 7.3% of the time on average. However, the samples studied using thin-shell NCs showed the particles emitting for significantly higher fractions of time. Thin-shell NCs were on average in their on-states for 69% of the time.

Displayed next to the SR results is the SEM image of the NC with the same distance scaling. The SR localizations are distributed more broadly than the physical size of the NC with a standard deviation of $\sigma_{avg} = 10.6$ nm. This is primarily a function of the SNR achieved for these measurements but it is also near the limits that SR microscopy can produce. Clearly distinguishing between multiple NCs will, therefore, be difficult because the standard deviation of the position distributions is larger than the NC size.

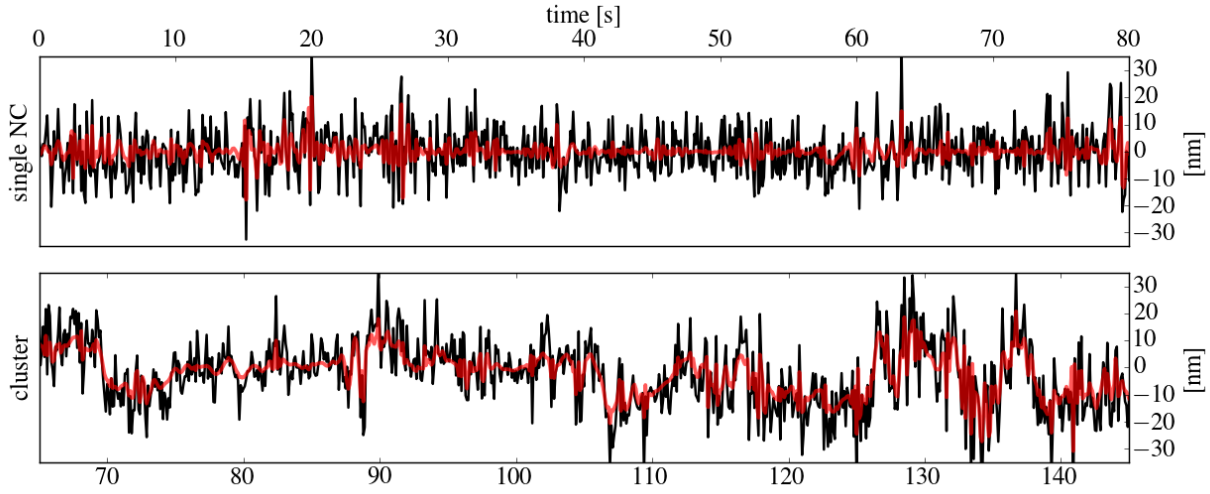

FIGURE 6.5. Wavelet denoising of an individual position coordinate for a single NC (top) and a cluster (bottom). The raw SR signals (black) are smoothed using wavelet denoising (red). Gaps due to blinking events have been removed for visualization.

A close examination of the position trajectories suggests a path to improve our ability to distinguish individual NCs within a cluster given the magnitude of the scatter obtained in experiments. Figure 6.5 plots the trajectory (black) of a single coordinate from a single NC and a NC cluster. Blinking events that would produce gaps in the traces have been omitted to illustrate continuous position trajectories. The single NC trace (top) appears to be random fluctuations about a constant mean. The NC cluster position trace (bottom) displays strikingly different behavior. Discrete and random jumps occur. This signal is not the result of fluctuations about a single mean value but is represented by fluctuations about multiple mean values with sudden transitions between them. A cluster of NCs can be described by its configuration—the on/off states of the constituent NCs—and a discrete transition of one of the NCs to a different state would result in a corresponding discrete step in the localization center as the configuration changes. In this picture, multiple levels that are associated with specific configurations represent different mean values with noise fluctuations around the means. Exploiting this interpretation we can improve the raw position traces.

A post-processing step which smooths raw coordinate trajectories can be performed to reduce the noise contribution and clarify the multiple discrete mean positions. Applying the approach of Taylor *et al.*[167, 168] to improve noisy single-molecule FRET trajectories, the position traces from SR fitting were smoothed using wavelet denoising. This involves applying a wavelet transformation to each position time trajectory. A threshold is applied to the transform of each trace to eliminate the high frequency signals and the resulting signals are then processed through the inverse wavelet transform to produce the denoised signal. The results of using a discrete Meyer wavelet basis with soft thresholding are shown in Figure 6.5 in red. The soft thresholding approach is commonly called wavelet shrinkage and differs from typical wavelet thresholding by applying an adaptive scaling of the wavelet coefficients that weights the coefficients according to their proximity to the threshold value. It was found that this approach resulted in effective denoising without introducing artifacts. However, other denoising methods aside from wavelet shrinkage can be used to reduce the noise of position trajectories. SR reconstructions presented in the remainder of the chapter will be plotted from wavelet denoised traces.

6.5. Nanocrystals Clusters

Where SR results from single NCs are straightforward, the results from NC clusters exhibit more complexity and subtleties that can indicate some of the underlying fluorescence dynamics. In particular, the pairing of the intensity distribution and the position distributions can indicate unique features within NC clusters that are not present in single NCs. We present an interpretation scheme where emission is categorized into high intensity (green),

medium intensity (red), and low intensity (blue). SR scatter plots are then grouped into regions based on their intensity characteristics which, when combined with the true structures from SEM imaging, can indicate the roles of individual particles.

6.5.1. Small Clusters. Dimers and trimers are the simplest clusters to interpret because the number of different emission configurations is limited and, in general, there are no ambiguous configurations that may be interpreted in multiple ways. Figure 6.6 presents the denoised SR results of several small thick-shell NC clusters and the correlated SEM imaging. Where the highest intensity (green) localizes in small clusters is an indication of which NCs are primarily responsible for emission. The SR image of Figure 6.6A clearly indicates the highest intensity localizing to the upper region of the cluster. The correlated SEM image shows a dimer in such an orientation that one of the NCs is positioned in the same region as the highest intensity localizations. Lower intensity emission is distributed across the entire area of the cluster. This dimer demonstrates the case of efficient ET where the upper NC is the acceptor and the lower NC is the donor. Only low intensity emission localizes in the region of the lower NC. The fluorescence trajectory of this dimer corroborates the indication of strong ET because it exhibits enhanced blinking. Another possible interpretation for the distribution of the intensity levels is that the upper NC has a high QY compared to that of the lower NC. This is unlikely because the low intensity corresponds to an emission rate just above background noise whereas the distribution of QYs for single thick-shell NCs (see Figure 6.2) is well above background rates and such a low QY NC would be a rare occurrence. The low intensity in the lower region of the dimer is due to the reduced emission rate of the lower NC which competes with ET. When the acceptor NC is in an off-state, this smaller emission rate can be observed.

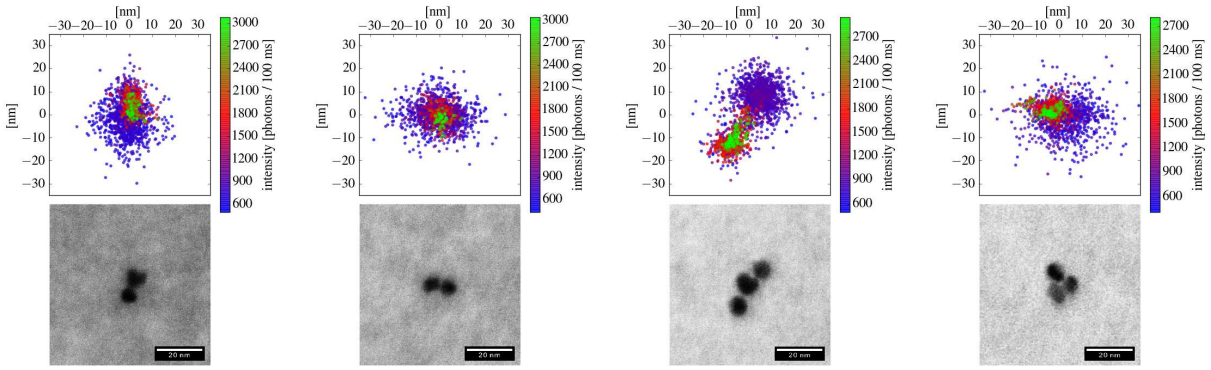

(A) (B) (C) (D)

FIGURE 6.6. Correlation of small thick-shell NC clusters. There is good agreement between the SR results and the SEM images. Figure 6.6A shows a dimer with strong ET signatures while Figure 6.6B shows a dimer without. The trimers in Figure 6.6C and Figure 6.6D illustrate cases where ET occurs but the geometry dictates specific donor/acceptor relationships: the linear case isolates one of the NCs while the pyramid example represents the most compact geometry which identifies a single acceptor. The SR and SEM images are scaled to match and the scale bars in the SEM images are all 20 nm.

In contrast to the efficient ET cluster, Figure 6.6B depicts a situation where there are no strong indications of ET from a dimer. This dimer exhibits a linear shape with the same orientation as the SEM image and the distribution of SR localizations, ignoring the intensity information, matches the SEM image. However, the highest intensity emission localizes to the region in between the two NCs, while both medium and low intensities are distributed across the entire extent of the cluster. This is the situation where ET is not an efficient process and the two NCs emit essentially independently. The highest intensity occurs when the both NCs are emitting simultaneously and the resulting SR fit is the geometric average of the positions. Medium and low intensities occur when at least one of the NCs is not in its on-state. One NC in its off-state produces a localization analogous to the single NC and should be positioned over the one emitting NC. However, grey states present configurations where there is a reduced contribution from one of the NCs, resulting in a weighted position at some location between the two NCs. It should be observed that, even in this simplest

of cases of a dimer, there is no indication from SEM imaging alone that would identify one NC as a donor and the other as an acceptor (from structural information), nor if ET is an efficient process (from distance information).

The SEM image of the linear trimer in Figure 6.6C is clearly reproduced in the SR image. Trimers are the smallest type of cluster where geometry must be considered for ET implications. This geometry represents a cluster where the spacing is large enough that at least two of the NCs are farther apart than the $\sim$ 10 nm localization standard deviation of a single NC. Individual NCs can also be identified from one another because a trimer, unlike larger clusters, still has a relatively small set of emission configurations to complicate the interpretation. The highest intensity localizes to the bottom-most NC and the upper-most NC appears to present as an isolated particle—the emission from the upper region is distributed across a circular region separate from the rest of the trimer. This trimer likely exhibits strong ET from the middle NC to the bottom-most NC and the upper-most NC behaves independently. While ET between the upper and middle NCs may occur, it is likely inefficient because the donor/acceptor signatures for those NCs that would arise when the bottom NC is off do not appear to be present. The final trimer in Figure 6.6D has a pyramid geometry which produces the highest probability for ET coupling because every NC is in closest contact with every other NC. Indeed, this trimer exhibits a strong ET signature as the highest intensity region is localized at the upper-left position. Emission originating from the positions of the other NCs is limited to the lowest intensity level.

6.5.2. Large Clusters. Where a limited number of ET pathways are available in small clusters, large clusters a can quickly become complex with the inclusion of only a few additional NCs. The variety of geometries that form produce arrangements where some NCs may be isolated while others may be participating in strong collective effects, and both

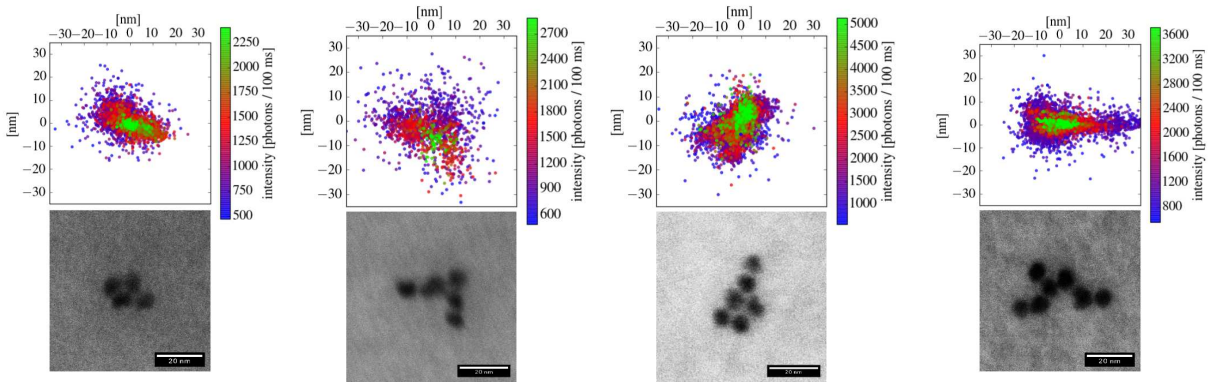

(A) (B) (C) (D)

FIGURE 6.7. SR of large thick-shell clusters with their true geometry from SEM imaging. Figure 6.7A and Figure 6.7C show clear high intensity features that do not localize over the geometric center position of the cluster which is an indication of ET. However, the clusters in Figure 6.7B and Figure 6.7D do not exhibit such off-center localization and likely do not have strong ET coupling. For larger NC clusters, the presence of each NC is not necessarily clearly indicated, unlike the simpler dimer and trimer cluster types.

contribute signals to the overall localization of the emission center. The tasks turns from determining individual ET relationships to identifying regions of fluorescence activity. Each change in emission configuration results in an emission center shift that provides information about the roles of the constituent NCs. Figure 6.7 illustrates a variety of large clusters types with their true geometries determined by SEM imaging. These clusters are large enough that their sizes exceed the $\sim$ 10 nm precision of SR localization and unique shapes emerge from the SR reconstructions. ET beyond nearest-neighbor and multiple ET events become important considerations for these large clusters. Furthermore, the finite range of ET mechanisms manifests as breaking long range collective effects into regions of activity. These more substantial structures serve as surrogates for studying the local collective behaviors that occur in higher-order NC system such as films.

The intensity distributions of large clusters are particularly descriptive in reference to their geometries. As with the small clusters, the large clusters in Figure 6.7 demonstrate

excellent agreement between the true physical structures and the SR images. However, the activity centers in the tetramer and pentamer (Figure 6.7A and Figure 6.7C, respectively) localize to regions of the clusters that are not the simple geometric mean of the structures. These clusters indicate hot spots of activity centered on particular regions offset within the clusters. In contrast, the high intensity regions of the hexamer and heptamer (Figure 6.7B and Figure 6.7D, respectively) are localized on the apparent geometric centers of the clusters. Among these large clusters, the tatramer and pentamer exhibit strong ET signatures while the hexamer and heptamer do not. There are no identifiable features in the SEM images of these clusters that would indicate the degree of ET efficiency within each specific cluster. As discussed previously, EM imaging that can resolve the NC core from the shell could provide more precise measurements of the inter-particle spacing, and possibly indicate the degree of ET efficiency that should be observed in the fluorescence measurements. However, the SEM imaging in this study could not resolve such details.

The interpretations of high, medium, and low emission intensities (green, red, and blue in the color coding scheme) from NC clusters take on the following meanings. The high intensity regions are typically associated with the emission from an acceptor within the NC or emission from the geometric mean where independent NCs are emitting simultaneously and the location is the average of the signals. Medium intensity regions are generally interpreted as the emission from acceptors without the enhancement from a donor (as in the case when the donor transitions to an off-state), or as the single emitters when ET is inefficient. The low intensity regions are produced by donor emission when the acceptor is in an off-state or from a combination involving grey states. Therefore, distilling the roles of individual NCs within a cluster involves interpreting the intensity information in the context of the structure determined by SEM imaging.

6.6. Discussion of Correlated Experiment

6.6.1. Intensity Scaling. Because many bulk applications attempt to multiply the benefits of single NCs by packing large numbers of particles into small areas, often in direct physical contact, the intensity scaling observed earlier in this chapter poses concern. On the large scale, it would be exceedingly unlikely to achieve the maximum possible device efficiency as the random and independent blinking imposes a limit on the fraction of NCs that may be simultaneously contributing to a desired signal. However, the deviations beginning at the dimer and trimer level—where there is a high probability of observing the configuration with all NCs in their on-state—indicate a more fundamental efficiency limitation. That both rapidly formed thick-shell NC clusters and slowly formed thin-shell NC clusters exhibited reduced intensity scaling suggests the effect is less specific to the details of attachment process than to the interactions and group dynamics in their final form. While the present measurements do not identify any particular source being primarily responsible for the scaling, several considerations are worth addressing.

Distribution of single NC intensities: Indicated in both Figure 6.2 and Figure 6.3 is the projected scaling if cluster intensity is the simple sum of individual NCs given the average intensity of single NCs. The distribution of single NC intensities was obtained from the same measurements as the clusters and all NCs from a measurement were exposed to the same environments. Therefore, any degradation of fluorescence from time, the processing steps, deposition, or experimental conditions would have be experienced by singles and clusters alike. The distribution of single NC intensities is projected in the plots and, despite the variations, do not account for the reduced intensity of clusters. However, these distributions were compiled from correlated NCs which includes an inherent selection bias as their fluorescence signal had to be observed in order to be correlated and, hence, confirmed as

single NCs. Under-representing the number of single NCs in a measurement by missing low intensity NCs was minimized as best possible by scrutinizing the movies. The correlation map was generated by constructing a frame that represented the magnitude of the standard deviations of individual pixels, which is a higher contrast method to identify emission spots. Effort was made to find every spot identified in this frame during the SEM correlation step. Hence, only the lowest of intensity would be missed. This effect of mischaracterizing single NC intensities is related to a second possible explanation for the observed scaling.

Dark fraction: Discussed briefly ealier, a substantial dark population could exist during cluster formation where the final clusters, despite containing a certain number of NCs, contain fewer particles that fluoresce. This would also apply to extremely low intensity NCs where their presence could be missed by selection bias. Characterizing the dark fraction of a batch of NCs is a difficult task, further complicated by the idea that the clustering process and sample deposition, possibly being a violent events for the particles, may increase the population of dark NCs. However, a few observations suggest the dark fraction of the samples, even after clustering, storage, and deposition, is relatively small.

Dimers present a limited number of emission configurations and SR imaging of such clusters easily identifies the roles of the individual NCs for both efficient ET coupling and inefficient ET. The ET dimer in Figure 6.6A exhibits a fluorescence signal originating from the bottom NC and the dimer is recognized as containing two emitting NCs. Even clearer is the dimer in Figure 6.6B where both NCs have strong fluorescence signals. Thus, by examining all of the correlated dimers in the sample for the presence in the SR image of two emitters, an estimation of the dark fraction can be obtained. For the thick-shell NC clusters, nine dimers were correlated and in only one was there an absence of one of the fluorescence signals. This places the dark fraction estimation as low as 6%. It should be noted that

dimers with two dark NCs are also possible. With the existence of such dimers, this approach underestimates the dark fraction. However, the probability a cluster containing two dark NC is small given the first-order approximation of the dark fraction, and such clusters do not significantly alter this estimate.

Multiple excitations: The presence of multiple excitons within a NC cluster would have a quenching effect on the overall fluorescence yield. Because of the greater number of absorbing NCs in clusters, multiple excitons can be generate nearly-simultaneously at different NC sites and, with efficient ET, transfer to the same acceptor NC where the Auger non-radiative recombination process would quench the fluorescence[169, 170]. The probability of multiple excitons is characterized by the average single-particle excited state occupancy, $\langle \mathrm{N} \rangle$, which is dependent on excitation conditions and the absorption cross-section of the NCs. Appendix B details the calculation for the 185 W/cm^2 CW excitation of these correlated measurements. While excitation conditions were set primarily to obtain reasonable SNRs that would result in high SR localization precision, the conditions also resulted in a small average occupancy probability where $\langle \mathrm{N} \rangle_{488\ \mathrm{nm}} = 0.055$. In this range, NCs are dominated by single exciton generation[171]. However, the average occupancy probability for a cluster containing multiple NCs, assuming excitations are independent events, is given by $\langle \mathrm{N} \rangle_{\mathrm{cluster}} = n \cdot \langle \mathrm{N} \rangle_{\mathrm{single}}$ and, for sufficiently large clusters, may result in the situation where multiple excitons are present. Maintaining $\langle \mathrm{N} \rangle_{\mathrm{cluster}} \ll 1$ is necessary to avoid quenching. While the excitation conditions for these correlated measurements satisfied this condition, lower power levels may result in different scaling behavior. A detailed power study could address more explicitly if multiple excitons are a major factor of the intenstiy scaling observed. However, the conditions applied here do not imply such quenching should have been strong.

Enhancement of loss mechanisms: The argument behind the expected fluorescence yield of a NC cluster is that every NC in a cluster contributes its individual intensity to the overall yield of the cluster. It is not expected that the absorption process is affected by the presence of additional NCs, although experiments to test this assumption have not been reported and may be difficult to address. Hence, the mechanism of the reduced yield must be due to processes that occur after excitation. Already several mechanisms have been identified as sources for reducing the QY (such as blinking, trap sites, Auger recombination, and non-radiative recombination sites) within an individual NC. However, when NCs are in close proximity, some of these mechanisms could also influence the dynamics of a neighboring NC, such as trapped surface charges at the interface between NCs, access to additional local trap sites, polarization of the exciton by the dipole moment of neighboring NCs, or effects due to charge transport where hot electrons may delocalize across the entire cluster[104]. Furthermore, when ET is efficient, the yield from a single exciton can be reduced as the exciton interacts with new non-radiative recombination processes at each NC along a chain of transfer events. Hence, a single absorption event may experience an amplification of loss mechanisms. Without suggesting a particular mechanism for the enhancement of loss mechanisms, we do propose that such sources are more significant contributors to the observed intensity scaling than the other sources discussed. The dynamics associated with additional loss mechanisms may also be responsible for the enhanced blinking features of NC clusters.

6.6.2. Position-Intensity Distributions. While the high intensity locations within SR images inform about the possible roles of NCs, particularly the dominant roles of acceptor NCs, the intermediate intensity levels also contain a great deal of information about the dynamics of NC clusters. The medium intensity level, for example, can be due to a single NC emitting without the mixing of other sources which would otherwise produce an averaged

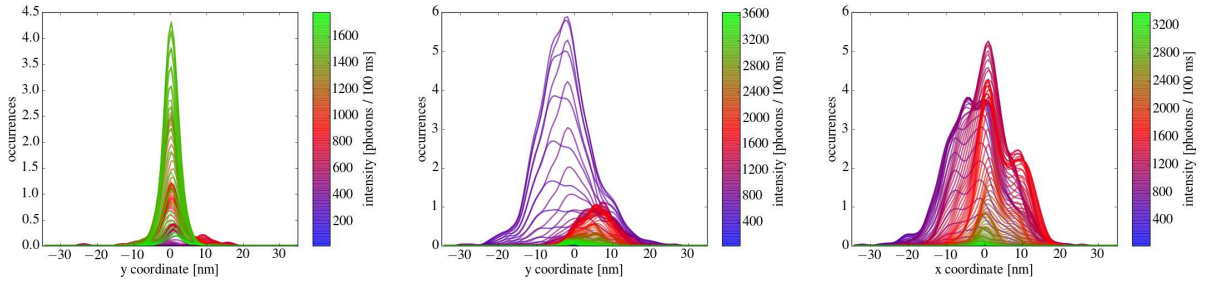

(A) Single NC (B) Dimer (C) Tetramer

FIGURE 6.8. PID lineouts of a single NC, a dimer, and a tetramer (same NCs as Figure 6.4, Figure 6.6A, and Figure 6.7A, respectively). Each lineout was smoothed by a Gaussian kernel with 1.4 nm FWHM.

position. Furthermore, low intensity regions can be attributed to donor emission or grey state emission. The scatter plot visualizations of Figure 6.6 and Figure 6.7 are presented with the position data sorted according to their corresponding intensity: high intensity markers are plotted over low intensity markers, obscuring the lower markers. While this scheme categorizes emission naturally into the respective intensity levels, the distributions of the low and medium intensity levels below the high intensity regions are less obvious.

Another approach is to present SR results as the distribution of the individual coordinates for various intensity levels. 2D histograms of position, either the x- or y-coordinate, and intensity are compiled from SR fits in what we term position-intensity distributions (PIDs). Presented in Figure 6.8 are PID lineouts from a selection of the previously discussed NCs. A single coordinate of the SR results is shown for each example. Each intensity bin is plotted and color coded on the same graph for comparison against other intensity levels. In these visualizations, the distirbutions of the low and medium intensity levels clearly show underlying structure not obvious from the scatter plot representations. By virtue of being constructed from histograms, these representations also indicate the number of occurrences of the relative intensity levels.

Basic interpretations of single NCs and small clusters from scatter plots are equally evident in the PID lineouts, although some nuance can be seen. The single NC in Figure 6.8A reflects observations already made: the high intensity (green) is dominant and localizes over a single location. Less frequent middle intensity levels (red) are also localized to the same region as the high intensity and very little low intensity (blue) is present. Not obvious from the scatter visualization of the NC is that a relatively significant grey state, represented by the medium intensity level, is observed. However, the various dimer intensity levels localize to different positions within the cluster in Figure 6.8B. The low intensity is centered to one side of the distribution and the medium intensity is centered to the other side. These are the features due to donor emission and acceptor emission that is not enhanced by ET (when the donor is in an off-state). Both of these intensity levels produce unique features that are well-separated spatially. Furthermore, the high intensity is not centered at the midpoint between the two other intensity features, but is weighted toward the medium intensity side. The high intensity feature can be understood as the emission configuration with both the donor and acceptor in on-states and the location of the signal is an averaged position of the two emission sources. The smaller fluorescence yield from the donor results in a weighting that favors the acceptor location and, hence, the high intensity localizes nearer to the medium intensity region.

Examining PIDs is more illuminating for larger and more complex clusters than the scatter plots. Figure 6.8C shows the PID lineout for the x-coordinate of the tetramer depicted in Figure 6.7A. The simple low/medium/high nomenclature is not as cleanly delineated, but it is clear that the different intensity levels have unique features and localize to difference regions accordingly. The medium intensity regions, in particular, contain multiple peaks. These intensity levels are likely due to fluorescence configurations involving single non-donor

NCs. This can include individual acceptors (with or without enhancement by ET) or non-ET NCs that fluoresce largely independently. The high intensities would then be due to donors being active and/or multiple acceptors emitting simultaneously. While the medium intensity localizes to the right side of the cluster, the low intensities distribute on the opposite side. Examining the SEM image for this cluster, the true structure is two rows of two NCs each, offset by half a NC spacing (in a close-packed structure). From the correlation a couple interpretations about NC roles are possible. The offset of the low and medium intensity levels may be due to the top row acting primarily as donors to the bottom row. This is also suggested by the scatter plot and the y-coordinate PID (not shown) where the high intensity clearly localizes to the bottom row. While the scatter plot might imply a single acceptor because the hot spot is small and localized, examination of the PID reveals two distinct peaks of medium intensity, suggesting multiple acceptors may be present in this cluster and act independently of one another.

Given the complexity of the arguments necessary for the simple tetramer, it is apparent that interpreting particle roles in larger clusters quickly becomes a daunting task. Every NC cluster needs to be scrutinized carefully in attempts to identify the roles of individual NCs. The approach utilized here also relies on two assumptions: (1) the cluster has transitioned to enough—if not all—emission configurations and multiple unique emission patterns have been observed, and (2) there was enough dwell time in each configuration to obtain a sufficient number of localizations that provide some weight to the significance of the features they produce. From an analysis perspective, there is also a great deal of information in the time traces of the localizations as the transitions between configurations are typically sudden and discrete events. However, visualizing such tracking can be difficult.

6.7. Conclusions

By preparing clusters from thick-shell NCs or thin-shell NCs, and imaging the fluorescence as the particles blink, SR images with distinctly different features from single NCs were obtained. Regions of low, medium, and high intensity are observed and are typically located at positions that are clearly off-center from the emission region as a whole. With correlated SEM imaging the SR results could be compared against the true geometries of the clusters and interpretations of individual NC roles could be implied in the context of ET. Small NC clusters, such as dimers and trimer, contain relatively few unique emission configurations and the individual NCs roles can be determined with good confidence. Large clusters can contain multiple emitting regions and only through the cycling of the various emission configurations can those hot spots be identified. In general, identifying NC roles in large clusters becomes significantly more complicated with the addition of only a couple NCs. Furthermore, with the SEM verification of the NC number in a cluster, intensity scaling curves were measured. It is clear that the intensity from clusters is suppressed for both thick-shell and thin-shell NCs as the numbers of particles in the clusters increases. The discrepancy between the overall cluster yield and number of NCs is likely due to the amplification of loss mechanisms that also scale with cluster size, and not due to other sources, such as dark populations, that appear to have minimal presence in these samples. These measurements represent the first application of SR imaging with EM verification on NC clusters and are a direct observation of ET. Mapping hot spots to such small distances has not been previously reported in higher-order NC structures.

CHAPTER 7

Orientation Super-resolution Microscopy of Nanocrystal Clusters

Using two different and relatively simple super-resolution fitting algorithms that make no assumptions about the emission properties of the emitters, Chapter 6 examined the SR imaging of NC clusters. A framework for interpreting SR results in the context of clustered NCs—with ET considerations and the incorporation of intensity information into the analysis—was established and validated for samples that were not strictly single-molecule systems, but where the true structure could be verified with SEM imaging. The unique emission characteristics of semiconductor NCs provide an ideal system for applying advanced super-resolution methods that extract information describing additional degrees of freedom of the particles: their orientation. Orientations of the transition dipole can be obtained from fluorescence imaging using model functions that appropriately describe the generally asymmetric PSFs of dipole emitters. The analysis framework presented in the previous chapter provides a foundation for studying the additional orientation information from SR imaging.

This chapter presents unpublished results applying orientation SR microscopy to NCs and NC clusters. While a preliminary study, the results advance the understanding of the collective dynamics in NC clusters and connect several observations made in previous chapters as well as reveal additional features. The experimental work was carried out by myself and Dr. Peter Goodwin of the Center for Integrated Nanotechnologies at Los Alamos National Laboratory under the guidance of Dr. Alan Van Orden and Dr. Marin Gelfand of Colorado State University.

7.1. Motivation for Particle Orientation Measurements

Clusters of NCs exhibit a variety of group dynamics that have been systematically described in previous chapters. From the physical structure of clusters, to spectral and lifetime characteristics, to blinking behavior, signatures of inter-particle interactions are present in multiple different single-molecule measurement methods. Cluster formation was shown in Section 3.3 to produce clusters that lacked a common alignment between NCs. Identified in Chapter 5 were collective effects in NC clusters that appear to inhibit the spectral diffusion typically observed in single NCs and lifetime measurements exhibiting signatures of ET. And direct observations of the motion of emission centers within NC clusters from Chapter 6 indicated donor/acceptor relationships. Several of the suggests mechanisms for such observations—namely, electrostatic influence from neighboring NCs and ET coupling—would also affect the dipole emission characteristics of such clusters.

The term dipole characteristics or dipole effects of NCs used throughout this chapter refers to the emission produced by a dipole. Specifically, a dipole emitter produces a unique emission pattern that is not isotropic. Intrinsic in the term dipole is an orientation axis that specifies a reference orientation. Hence, the angle between the orientation of a dipole and the direction from which it is viewed or imaged describes the unique emission pattern. The emission from NCs can be formed by super-imposing three orthogonal dipole emission patterns of different strengths: two that represent the degenerate 2D emission plane and one that represents the 1D emission. In well-formed NCs, the 1D emission dipole is oriented along the c-axis of the crystal and the 2D plane is perpendicular to the c-axis. For these experiments, the 2D emission profile dominates the final emission pattern, meaning the 1D dipole emission contributes negligible intensity compared to the 2D emission. The sum of

these signals produces the unique emission patterns which carry information about the orientation of the emission planes relative to the observer. However, the emission or transition dipoles should not be confused with the permanent electrostatic dipole moment that NCs also poses. While electrostatic dipole moments play a role in orienting NCs during clustering and may produce Stark effects on neighboring NCs, our discussions will not be concerned with the electrostatic dipole moments of NCs.

Dipole effects produce interesting behavior in individual NCs. Chen *et al.*[166] and then later Li *et al.*[172] observed spontaneous rotations of the emission planes in CdSe/ZnS NCs and attributed them to environmental influences and surface conditions. However, these studies did not spatially resolve NCs nor provide verification of single-emitters in the measurement volume. While the crystalline structure and orientation is fixed, such studies suggest there are mechanisms that allow a dynamic emission plane that changes, weakening the connection between fluorescence behavior and crystal orientation. With neighboring NCs modifying the local environment, NC clusters may exhibit such dynamic dipole effects in a manifestation of collective behavior. Furthermore, ET, strongly dependent on the dipole orientation, would be affected by such spontaneous rotations.

To study the dipole dynamics in NC clusters, a different approach to modeling the PSF is necessary. Enderlein[173] developed a theoretical framework that considers dipole emission imaged by a high NA objective with a vector-optics based approach, providing detailed PSF models for dipole systems. Initially, the framework for dipole emitters was applied to defocused imaging where PSFs deviate dramatically from the Gaussian or Airy disc models[174, 175]. The 2D emission nature of NCs has been verified[163–165, 18] and 2D+1D emission behavior was observed by Cyphersmith *et al.*[102], demonstrating emission from the various spin states including the spin 0 state. While the effects of dipole emission

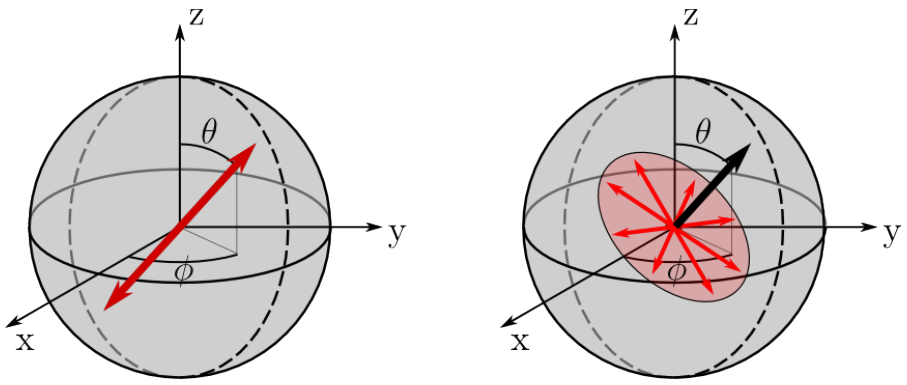

FIGURE 7.1. Orientation conventions for 1D linear dipoles and 2D dipole planes. For 1D dipole emission, θ is the polar angle and ϕ is the azimuthal angle defining a single vector representing the dipole (red, left). 2D transitions constitute a degenerate plane of dipoles (red, right). A vector perpendicular to the emission plane is used in this work to index the orientations for 2D emission and the angles θ and ϕ refer to this vector normal to the plane.

are particularly strong in defocused experiments and such images yield uniquely characteristics PSFs, defocused measurements cannot be used for SR localization because the spatial information is too diffuse. On- or near-focus imaging provides the conditions necessary for effective SR localizations, and applications of dipole emission model PSFs have only recently gained popularity.

7.2. Methods and Analysis

Applying dipole PSFs to SR imaging enables the mapping of orientation and emission dynamics from NC clusters, an extension to the SR approach used to understand NC clusters in Chapter 6. The orientation conventions for 1D dipoles and 2D dipole planes are shown in Figure 7.1. While the polar angle θ and azimuthal angle ϕ define the orientation of a vector corresponding to a 1D dipole, we use these angles to define, for the 2D case, the plane that is normal to the vector. Emission from a 2D dipole emitter is generated by any orientation of 1D dipoles within this plane.

Construction of a 2D dipole PSF is done by superimposing the images of two orthogonal 1D dipoles that lie within the plane normal to the specified angles[164]. While it seems counter-intuitive that such superposition would correctly describe emission from all subsets of 1D dipole orientations within the plane, it was verified that this approach produces the correct PSFs. Figure 7.2 illustrates the on-focus PSFs for 1D emitters (top) and 2D emitters (bottom). Shown are over-sampled images that would then be integrated over pixel areas to produce the image a camera would observe. Contained in the asymmetry of these PSFs is information about the orientation that is obtained simultaneously with SR position. Examining lineouts from these PSFs, Figure 7.3, demonstrates how dipole effects can bias SR localizations. The center peak, which carries significant weight in most fitting methods, can be located off-center by tens of nanometers. A symmetric model PSF, such as a Gaussian or Airy disc, would produce a fit that attempts to maintain the symmetry despite not corresponding to the center location.

To measure the orientation dynamics of NC clusters, we have implemented a SR algorithm to fit dipole PSFs. Most strategies to accommodate 2D dipoles, particularly in defocused imaging, fix the orientations of two 1D PSFs relative to one another, ensuring they are linearly independent and orthogonal. However, by using a model function with two independent 1D PSFs constrained to the same origin, but not the orientations, ellipticity and deviations from an ideal circular 2D plane can be accommodated, as well as introduce the flexibility of modeling a system that may not necessarily maintain a strict 2D dipole because of interactions or broken degeneracy. Such an approach only introduces one additional degree of freedom compared to a fixed approach which would need two additional parameters to model eccentricity and the rotation of the axis of eccentricity. Finally, the

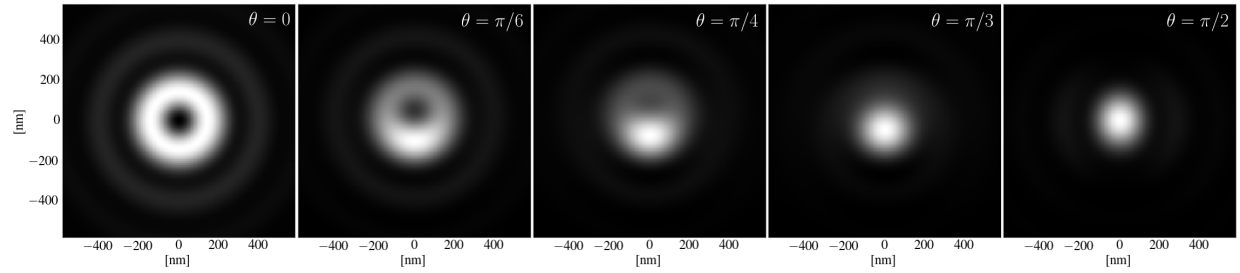

(A) 1D PSFs

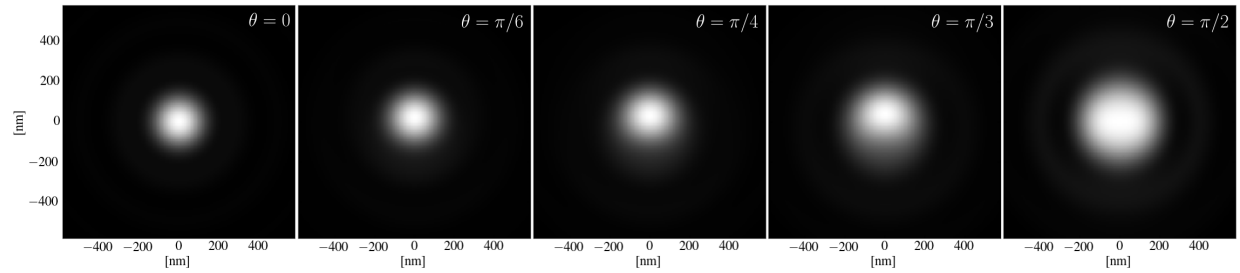

(B) 2D PSFs

FIGURE 7.2. Model PSFs for 1D dipoles and 2D dipole planes calculated on focus at several different polar angles ($\phi = 0$). The unique distributions enable the extraction of orientation information from the image data even on focus. Here, the z-axis of Figure 7.1 is aligned with the optical axis.

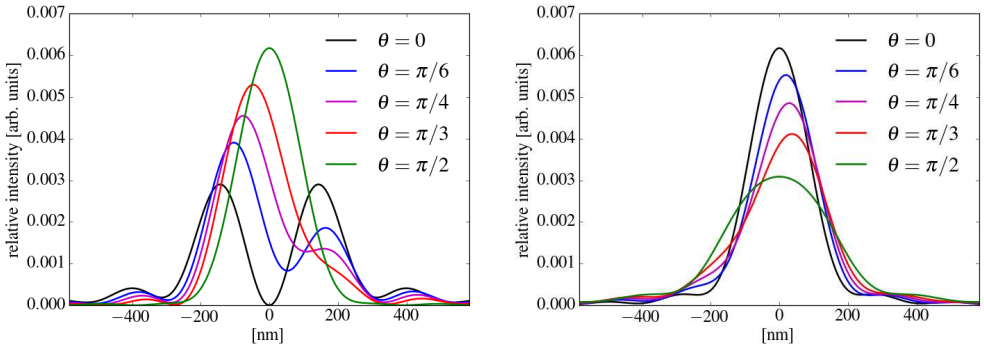

(A) 1D PSF (B) 2D PSF

FIGURE 7.3. Lineouts of 1D dipole PSFs and 2D dipole plane PSFs for several different polar angles. The SR localization bias that is introduced by symmetric PSFs (such as a Gaussian model) can be understood from the peak shifts in both the 1D and 2D cases. Information in the tails of the PSFs is symmetric; however, the peaks are dependent on the polar angle.

implementation also applies a noise model that considers EMCCD gain in the calculation of the likelihood function and accounts for pixelation.

Thick-shell NC clusters produced by slow clustering were prepared to study orientation dynamics. To obtain images that contain dipole information, the simple imaging configuration with NCs deposited directly onto glass coverslips was used. Glass substrates are not, in general, compatible with EM imaging without additional sample treatment because charging of the surface results in poor identification of small features. While coating samples for the SEM with Au is a common approach, this method was not successful as a post-treatment step after fluorescence measurements because no NCs could be found with the SEM. Circularly polarized excitation is typically used to study orientation effects in NCs and placement of a quarter-wave plate into the excitation beam path produced such conditions for these measurements. Because excitation is far above the band gap, circularly polarized light does not specifically select excitation into the 2D dipole plane over the 1D dipole state as phonon-assisted energy loss into the 1Se state can alter the spin state.

Figure 7.4 compares the dipole SR implementation against the ThunderSTORM and DAOSTORM algorithms. The custom algorithm produces comparable localization accuracy. For the example NC cluster depicted, ThunderSTORM produces very similar results to the dipole algorithm. However, DAOSTORM introduces artifacts because of transitions between different asymmetric PSFs generated by NCs with unique orientations within the cluster. Because DAOSTORM uses a fixed PSF that has some measure of dipole effects, transitions between differing patterns results in large errors. A halo feature appears around DAOSTORM objects when changes to the PSF occur, as illustrated in the large field of view in Figure 7.4D. See Appendix D for a detailed discussion about the halo features in

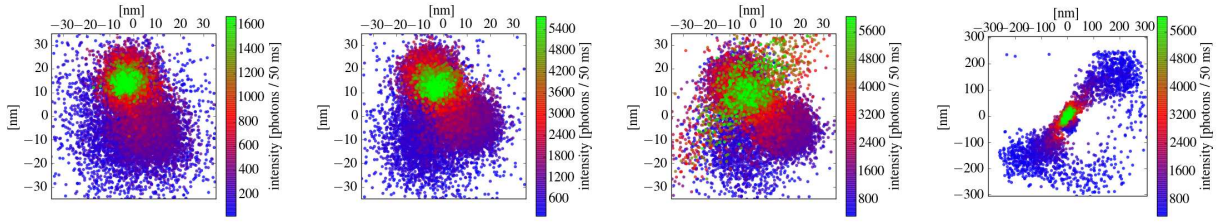

(A) 2D dipole (B) ThunderSTORM (C) DAOSTORM (D) DAOSTORM halo

FIGURE 7.4. Comparison of SR results using various fitting methods. ThunderSTORM, using a symmetric Gaussian PSF, does better to match results of data from 2D emitters than DAOSTORM, where asymmetric PSFs create halo features.

DAOSTORM. The effects of orientation changes in ThunderSTORM analyses are manifested as smaller biases because the algorithm uses a symmetric Gaussian PSF.

The independent superposition approach to fitting emitters with 2D transition planes produces two vectors, each corresponding to a 1D dipole within the transition plane. Because their orientation to one another is not fixed in this approach, the vectors are not guaranteed to be linearly independent. It should be noted that only orthogonal combinations of the two 1D dipoles in the emission plane correctly reconstruct circular 2D emission patterns. Furthermore, one of the dipoles may dominant and unequal magnitudes can emulate emission from an elliptical transition plane. A measure of the combined effects is described by the magnitude of the normal vector. The orientation of the normal vector represents the orientation as defined in Figure 7.1. The magnitude contains information about the eccentricity and orthogonality, calculated according to the cross product

$$\varepsilon = \left(\frac{I_1}{I_1 + I_2}\right)\hat{\mu}_1 \times \left(\frac{I_2}{I_1 + I_2}\right)\hat{\mu}_2$$

where I_i is the intensity associated with the ith 1D dipole oriented along the unit vector $\hat{\mu}_i$.

Figure 7.5 shows the eccentricity for a single NC and a NC cluster. The histrograms show the distribution of eccentricity values over all frames fit during the measurement for the given

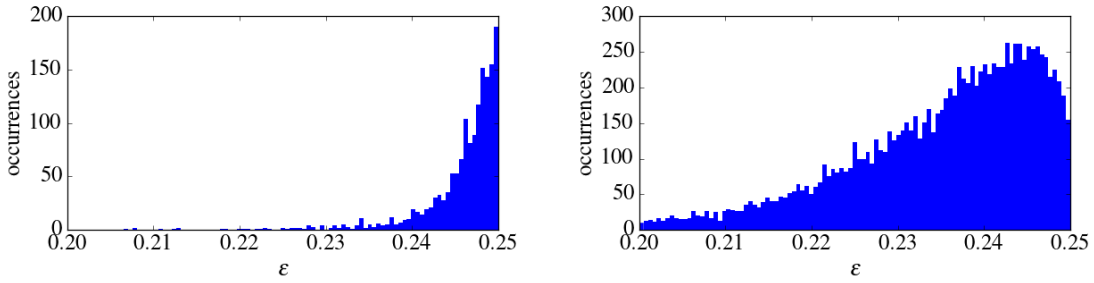

(A) Single NC (B) NC cluster

FIGURE 7.5. Ellipticity of the 2D dipole plane can be measured by fitting two 1D dipoles. Weighting by the relative magnitude of the two orientations and calculating the cross product of the vectors gives a measure of the combined ellipticity and linear dependence of the 1D dipoles. A value of $\varepsilon = 0$ refers to the case where the data was fit by a nearly 1D dipole, whereas a value of $\varepsilon = 0.25$ would represent a perfectly circular 2D dipole plane. The distributions are generally confined to the upper range with $0.20 < \varepsilon < 0.25$ and there are very few occurrences with $\varepsilon < 0.20$.

particles. From the definition above, emission from a circular plane that is best deconvolved into two orthogonal vectors produces the maximum value of $\varepsilon = 0.25$. A value of $\varepsilon = 0$ represents emission that is nearly 1D—either linearly dependent or a negligible magnitude for the second dipole. The distribution of ε for a single NC is grouped primarily near the maximum value, indicating single NCs are best described by a 2D dipole. This particular NC emitted primarily from a circular plane. Other reports of single NCs measured sample distributions of ellipticity ranging from strongly elliptical to perfectly circular[165] and of the identified single NCs in this study, similar distributions of ε as Figure 7.5A were found, indicating the samples were relatively homogeneous.

Eccentricity measurements of a NC cluster, Figure 7.5B, shows a broad distribution of ε. Such a characteristic distribution exceeds the variations of single NCs from the same measurement and similar distributions were observed for other clusters. While such a distribution may suggest that clusters posses more elliptical emission planes than their constituent NCs—and that interaction among the NCs is the source of the different behavior—it should

be recognized that for clusters with multiple emission centers (inefficient ET or large clusters), fitting two 1D dipoles may preferentially identify the dominant components of each of the multiple emitters. The random orientations of the individual transition planes would result in a broadening of the distribution. Sorting out such sources requires the additional consideration of the orientation distributions.

As noted before, the magnitude of the normal vector is affected by orthogonality and eccentricity. The individual contributions can be separated by examining the distributions that are derived from the simple cross product, $\hat{\mu}_1 \times \hat{\mu}_2$, which indicates only orthogonality. Comparing such distributions to those in Figure 7.5 suggests that both effects are simultaneously present and that there is no one single source for broader magnitude distributions.

7.3. Results from Orientation Fitting

Gaining appreciation for the results of single NCs provides perspective to interpret the more complex cases of NC clusters. Figure 7.6 depicts three single NCs that exhibit different orientation features. To present the orientation information (bottom row), the polar angle θ and azimuthal angle ϕ of the vector normal to the 2D emission plane are plotted for each frame as polar scatter plots, color coded according to the total intensity $I = I_1 + I_2$. No denoising has been applied to the SR localization scatter plots (top row). With a dipole model PSF, SR localization images of single NCs look similar to the correlated results detailed in Chapter 6. Of the single NCs identified in these measurements, most exhibited a high on-time fraction. This was also observed in thin-shell samples and suggest the slow clustering method better preserves the fluorescence stability of NCs compared to the harsh environmental treatment of the rapidly clustered thick-shell NCs.

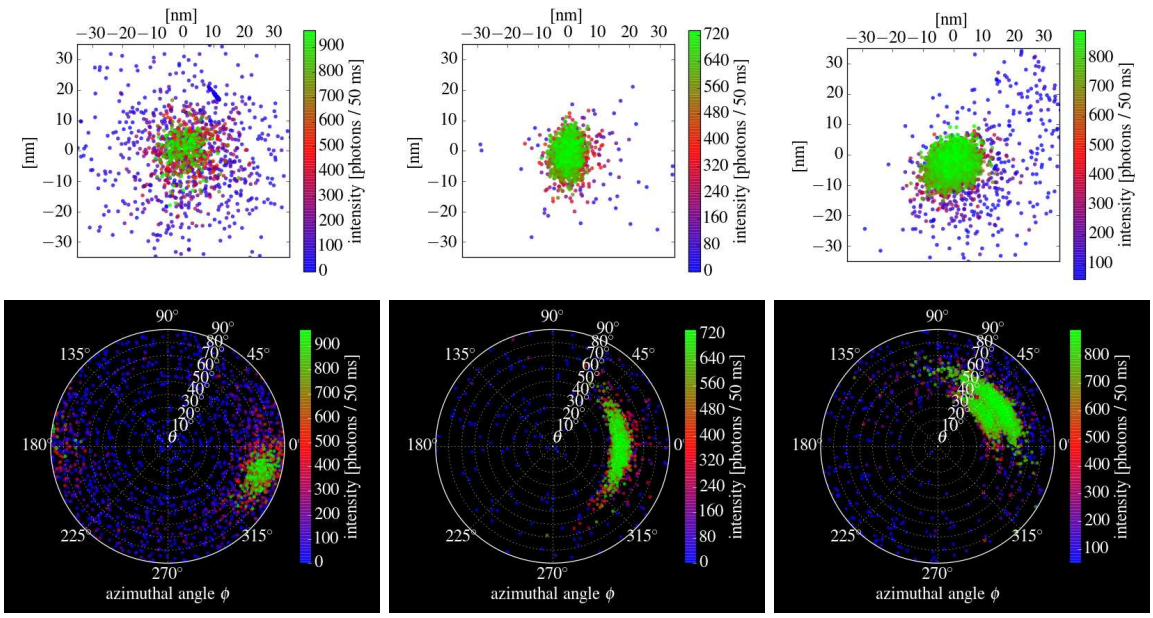

FIGURE 7.6. Types of dipole orientation features observed from single NCs. The top row shows the SR localizations of three NCs and the bottom row shows their emission orientations. The orientation plots depict the angles that define the orientation of the dipole emission and not the emission pattern itself (see Figure 7.2). A NC may exhibit a single well-defined orientation (Figure 7.6A), a distribution of azimuthal angles (Figure 7.6B), or multiple distributions (Figure 7.6C). While the NC with a single well-defined orientation did not emit long enough to observe multiple intensity levels, the two NCs with distributed features show clear signs of grey states.

Single NCs exhibit straightforward orientation distributions. The example in Figure 7.6A has a well-defined orientation as illustrated by the small distribution of high intensity fits around a single pair of angle coordinates. As another, and more common, example of single NC orientation signatures, Figure 7.6B depicts a similar distribution of polar angles as the previous NC, but with a broader distribution of azimuthal angles. Orientation features of this type are generally the signatures of emission from single NCs with stable emission planes and such examples are common.

A less frequently observed signature of some single NCs is depicted in Figure 7.6C. Two features are prominent with similar azimuthal distributions, but distinctly different polar

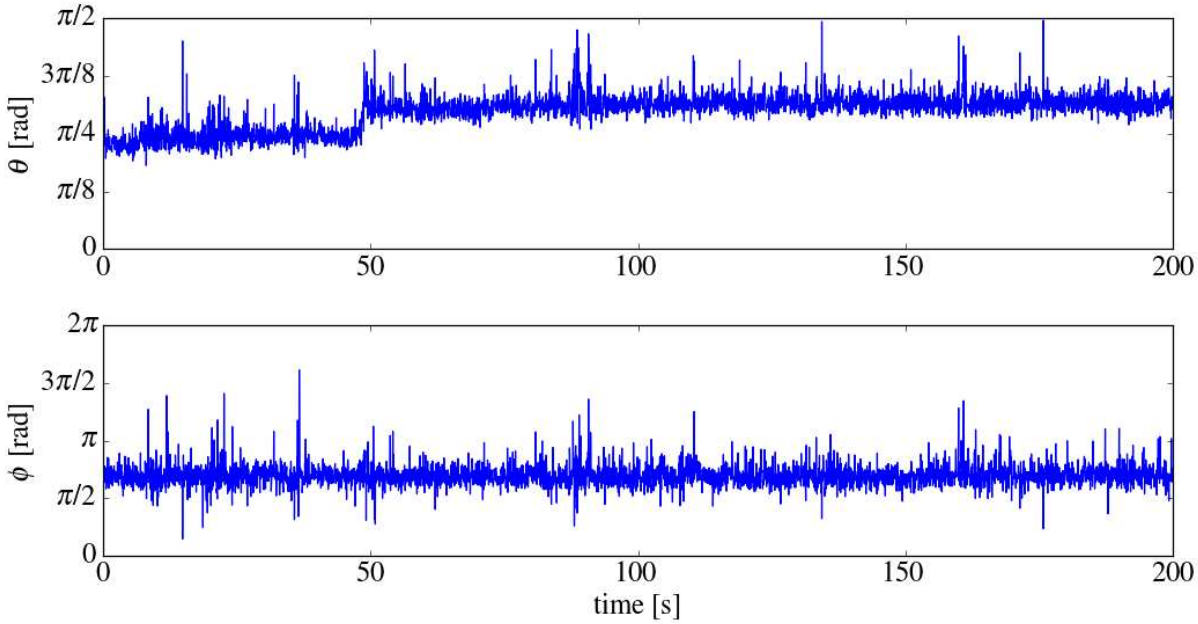

FIGURE 7.7. Time traces of the orientation angles for the single NC in Figure 7.6C. The multiple distributions evident in the scatter plot are shown to be two distinct polar orientations with a single sudden transition from one to the other. There are no discrete changes in trace of the azimuthal angle, indicating the azimuthal orientation is distributed, not the product of transitions between multiple discrete orientations. The blinking events have been removed to show the angles as continuous traces. However, the discrete change of the polar orientation occurred during a prolonged off-state, indicating a correlation with blinking.

angles. Figure 7.7 shows the time-trace of the two angles for this NC. The two features with distinct polar angles are the result of a sudden and discrete transition that occurs in the middle of the measurement. No corresponding change occurs in the azimuthal coordinate when the polar jump occurs. The blinking events were removed from the traces to provide continuous stream to compare; however, the transition in the polar orientation occurred during an off-event. This type of orientation change after a blinking event has been observed in defocused imaging[166, 172].

The broad azimuthal distributions that are frequently observed for single NCs, though seemingly uninformative, are also unexpected from NCs with static and fixed emission plane

orientations. While examination of the spectral traces in Chapter 5 showed that those broad distributions were the result of random but discrete changes and not from random fluctuations, traces of the azimuthal coordinate show so such underlying dynamics, as illustrated in Figure 7.7. The width of the distributions are determined exclusively by uncorrelated noise. Furthermore, the orientation variations are not due to the finite variance from fitting (realization of the Cramér-Rao bound from the information content of the estimator). The single NC example in Figure 7.6A has a narrower distribution under nearly identical intensity conditions and is more representative of the fundamental precision of the azimuthal parameter estimation. Furthermore, simulations of fixed dipole orientations given the SNR conditions achieved in these measurements produce an orientation feature identical to Figure 7.6A with the similar distribution widths.

Previous studies that observed discrete orientation changes attributed such dynamics to charge redistribution in the vicinity of the NCs—either from surfaces charges or from the environment. While sudden and discrete orientation changes, such as the polar angle transition discussed above, may be due to dramatic charge redistribution, the variance of the azimuthal angle may be due to smaller random fluctuations of the electrostatic environment of the NCs. The NCs in this study were deposited directly onto glass coverslips and exposed to air on the other side of the interface. Glass surfaces exhibit random charge fluctuations which may contribute to the broader azimuthal distributions. NC properties such as polycrystallinity may also play a role in some types of orientation dynamics.

Multiple non-interacting NCs produce features that need to be understood for context when later discussing NC clusters. Figure 7.8 shows the SR and orientation signatures of two NCs in close proximity. The medium intensity level (red) corresponds to the fluorescence intensity of individual single NCs. Between the two NCs is the high intensity (green) which

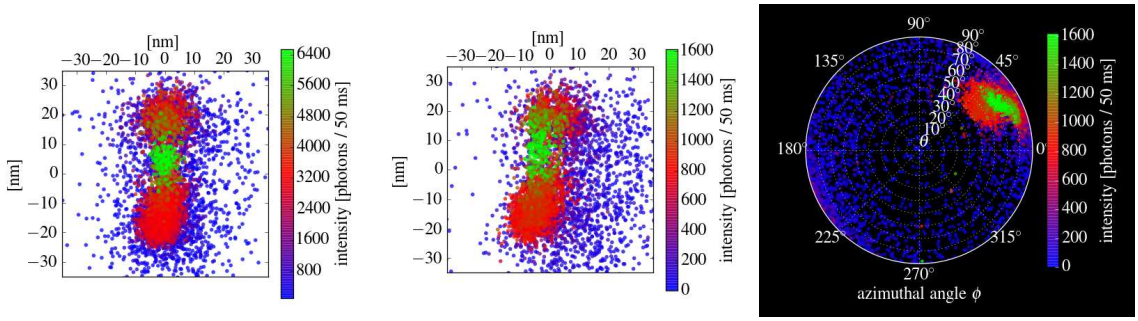

(A) ThunderSTORM (B) 2D dipole (C) 2D dipole orientations

FIGURE 7.8. Dipole results from multiple NCs compared with the results from ThunderSTORM. While both methods produce similar SR localizations, the additional orientation information from the dipole fitting illustrates the features associated with multiple NCs having unique orientations.

represents the configuration where both NCs are in their on-states, resulting in an averaged SR position. ThunderSTORM analysis corroborates and results in a nearly identical SR image. That the two NCs have similar intensities is an example of the fact that the sample has a narrow distribution of single NC QYs. The orientation distribution for these NCs, Figure 7.8C, depicts the same features. Two medium intensity regions with different polar and azimuthal angles appear and the high intensity orientations average the two features. Because the individual orientations of two NCs are relatively close, the effects of dipole emission do not bias the ThunderSTORM analysis significantly, explaining the good agreement of SR localizations between the two methods.

Orientation SR imaging of NC clusters yields the familiar results that were detailed in Chapter 6. Small clusters of NCs are shown in Figure 7.9 along with their orientation plots (bottom). The SR images (top) of these clusters show signs of ET. Localizations of the high intensity to regions off-center are clear in each of the small clusters. Such features identify the presence of acceptor NCs. As before, the low intensity regions localize to different positions within the clusters and indicate the presence of donor NCs. The dissimilar intensities between the regions is another indicator of ET. Non-interacting NCs would produce similar medium

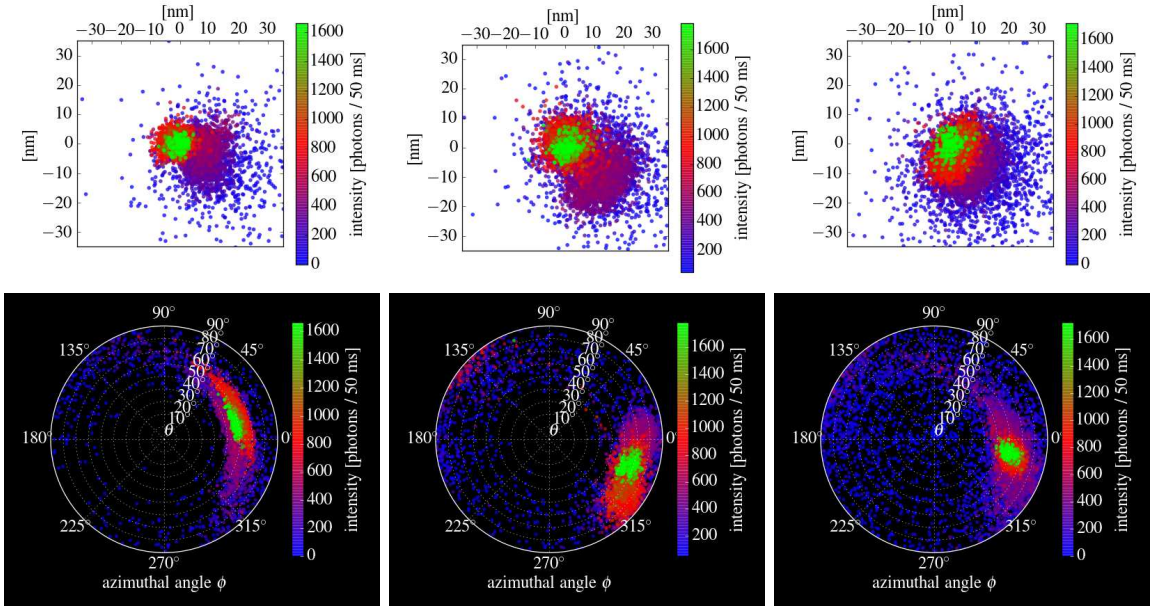

FIGURE 7.9. Dipole results from three examples of small clusters. SR localizations are depicted in the top row without denoising. The respective orientation plots for each cluster are displayed in the bottom row. Each cluster exhibits unique orientation features.

intensity levels at each NCs position due to the narrow distribution of QYs (as illustrated in the multiple NC SR images) and this is not observed for the small clusters in Figure 7.9. ET from donors reduces their intensity while enhancing the yield of the acceptors. These thick-shell NC clusters exhibit an ET efficiency significant enough to produce the dissimilar intensity levels between the donors and acceptors, but not so efficient that the donor emission is relegated to only the lowest intensities.

Orientation features of small NC clusters follow the same logic as the SR localizations with regards to donor/acceptor roles. The cluster in Figure 7.9A depicts two orientation features corresponding to donor NCs and acceptor NCs that have different polar orientations. The high intensity feature is the average of the individual orientations and represents the configuration where both donors and acceptors are emitting simultaneously. Angle traces of this cluster (not shown) also exhibit discrete changes of the polar angle between the various

features corresponding to the random configuration changes between two values and not simply a single broad distribution. Furthermore, there is a correlation of small azimuthal angle changes with the polar angle changes; however, the different orientations are primarily due to the polar angles.

Orientation features of a similar form—multiple unique polar orientations—were described for the single NC example in Figure 7.6A. The intensity distributions differentiate the rotations of individual NCs from multiple NCs with different orientations. Because of ET, the emission intensity is different for the two polar orientations of the cluster. The single NC maintained the same intensity between the two orientations. However, because the multiple orientation single NC was a rare occurrence, it is difficult to ascertain if the lack of an intensity change is a common feature. There is the possibility that such orientation changes in single NCs may correlate with grey states, which were also a rare occurrence in these measurements.

In contrast to the first NC cluster example, Figure 7.9B depicts a cluster where the orientation changes occur primarily in the azimuthal angle. The same arguments identifying donor and acceptor features apply, however, the transitions involve the azimuthal coordinate instead of the polar coordinate, which is also reflected in the angle traces of this cluster (not shown). Finally, where the first two small clusters were represented by multiple distinct orientation features, the orientation plot of the cluster in Figure 7.9C does not indicate signs of multiple features. Examination of the angle traces for this cluster indicates no discrete orientation steps. However, the traces do show sudden changes between broad and narrow distributions around the single orientation coordinates.

Described above were three different orientation behaviors that were observed for small clusters. While the orientation features were different, no indication that they would be was

given by the SR localizations alone. Indeed, the three clusters appear to exhibit similar ET efficiencies. Because the clusters are small—although no size verification could determine the true number of NCs in each—these examples likely represent the simplest types of clusters: dimers and trimers. This is further supported by the correlated study of thin-shell NCs in Chapter 6 that showed the slow clustering method, overwhelmingly resulted in monomers, dimers, and trimers.

Briefly, we present the orientation results from large clusters to demonstrate the various features that may appear and the difficulties that arise with more complex systems. Figure 7.10 depicts the SR localizations and orientation plots of several large clusters. Extending the arguments applied to orientation signatures of small clusters quickly becomes difficult when additional NCs are involved due to the rapidly increasing number of possible emission configurations, and the potential for multiple regions of the cluster to emit simultaneously. Orientation fitting is then complicated by multiple independent emitters that are not represented by the two independent 1D component approach. Fitting the data to two 1D dipoles is not applicable as there are insufficient independent PSFs to describe the emission pattern produced by multiple 2D emitters. Furthermore, large clusters may produce local environments through close proximity that may generate different representations of emission planes due to interactions breaking the degeneracy of the 2D planes.

7.4. Conclusions and Future Work

Using dipole model PSFs in SR image analysis can uncover orientation dynamics from interacting NC clusters. ET signatures in small clusters show straightforward mixing of the orientations from the participating NCs. The orientations of donors and acceptors generally produce unique and well-defined features that can be clearly identified. Discrete orientation

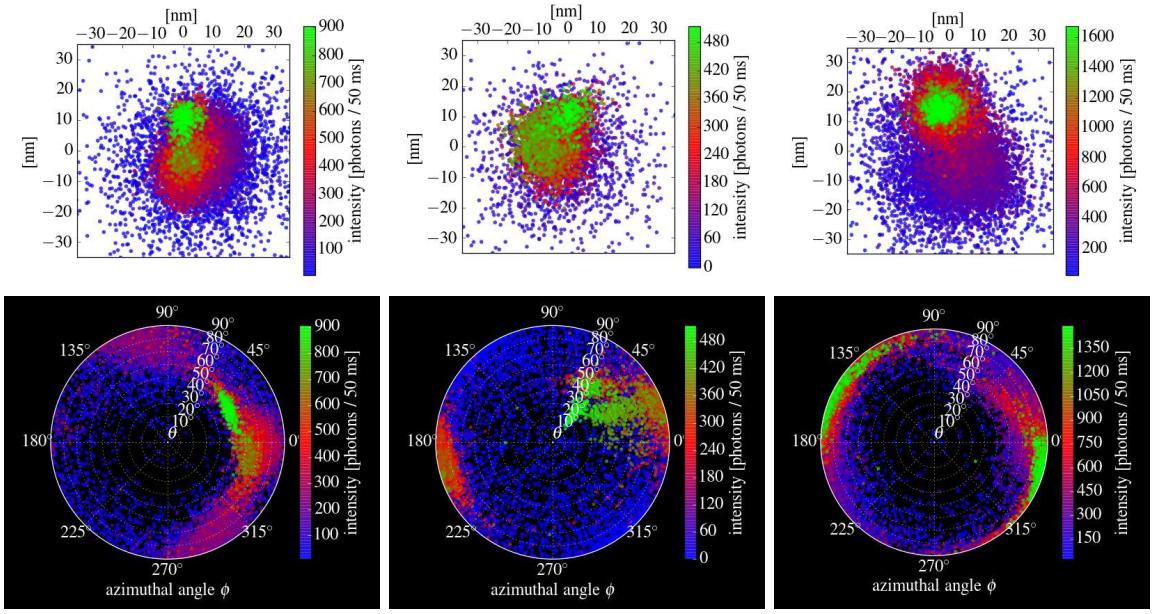

FIGURE 7.10. The variety of orientation features (bottom row) from large clusters (corresponding SR results shown in top row).

changes have been observed and are connected with emission configuration changes. Small clusters retain the 2D dipole characteristics of the individual emitters and the resulting dipole maps suggest simple mixing of the individual signals. Large clusters, in contrast, exhibit orientation features that do not fall cleanly into the categories of orientation signatures produced by single NCs.

While the dynamic orientation behavior could be measured, identifying the mechanisms responsible requires further investigation. Among the small clusters analyzed, the orientation features appear to be mixes of similar-type single NCs signatures: two azimuthally distributed features mix in Figure 7.9A and two variance-limited features mix in Figure 7.9B. A more comprehensive study of the orientation distributions from small clusters is necessary to identify trends and, where trends do appear, to study if interactions are responsible for the trends.

It is interesting to note that the mixed features in small clusters are generally between similar orientations. For example, the azimuthal difference between the two features in Figure 7.9B differ by less than 45°, and the polar features in Figure 7.9A by even less. An unresolved question about the slowly formed clusters is the possibility of oriented attachment. These orientation maps suggest small clusters may exhibit such correlation and correlated TEM measurements, if a suitable method can be found, could provide explanations for such trends.

Modified experimental and analysis approaches may help extract more accurate dynamics of orientation behaviors and reveal additional behaviors. Because dipole SR imaging depends on deviations from symmetric PSF patterns, deconvolving the microscope IRF may provide accuracy improvements and reduce bias introduced by the instrument. An interesting study could be done comparing the orientation distributions from linear and circularly polarized excitation. Such excitations conditions could drive particular ET pathways and the imaged PSF may have stronger contributions from 1D or 2D emission. Finally, splitting the image on the EMCCD into red and blue channels could provide simultaneous measurements of the spectral behavior, similar to the measurements in Chapter 5. Because it has been suggested that orientation changes and spectral diffusion share underlying mechanisms, the simultaneous measurements could reveal correlations.

CHAPTER 8

Conclusions and Perspective

Previous works studying the fluorescence properties of NC clusters established the fundamental differences of cluster behavior when ET is present. The enhanced blinking in NC clusters observed by Yu *et al.*[16] was attributed to electronic coupling. Shepherd *et al.*[84, 21] expanded the understanding of altered fluorescence behavior to introduce an ET model that effectively recreated the blinking and fluorescence lifetime signatures of similar NC clusters. An assumption of the model is that NCs retain their individual fluorescence and blinking properties in clusters and that ET serves to open alternative exciton relaxation pathways. The work of Whitecomb *et al.*[87, 85, 22] made detailed single-molecule studies to verify the assumptions of the model by establishing that blinking statistics are, indeed, unaltered when NCs are clustered. Furthermore, anti-bunching experiments—a measure of the independence of decay events—matched the expectations of the ET model without additional considerations.

The conclusions of these studies were determined without specific knowledge of the form or geometries of the NC clusters—vital pieces of information to describe the unique manifestations of ET pathways and to explain the broad range of fluorescence behaviors observed—nor place the fluorescence behavior in the context of individual NC characterization which may affect coupling efficiency. This work expands the understanding of collective effects by incorporating methods that determine cluster structure—either directly with EM imaging or indirectly through SR. Independent TEM characterization studies identified properties of NC clusters that affect ET which cannot be gleaned from fluorescence measurements. Specifically, the distributions of inter-particle spacing from a particular sample, the observations

concerning random NC orientations, and geometry types that clusters form are new pieces of information which carry implication about how NCs interact.

The various single-molecule studies described in this work further the understanding of the fluorescence behaviors of NC clusters in connection with their physical properties. Lifetime and spectral measurements of NC clusters (from clustered broadly batches characterized by TEM) affirmed the ET model with direct observations that the highest intensity originates from smaller band gap emitters serving as acceptors within a cluster. These studies also indicated spectral diffusion of individual NCs can be suppressed when the particles are incorporated into clusters, resulting in spectral dynamics that are correlated with intensity fluctuations.

As the first application of SR methods to NC clusters, the experiments in this work demonstrated the power of such an approach. SR experiments that correlate localization measurements with SEM information about the true structure of a NC cluster spatially resolve donor and acceptor emission near the precision limit of SR microscopy and matched the verified geometries. With an independent verification of the number of NCs within a cluster, it was further observed that the fluorescence yield of clusters that interact does not scale as expected with the number of absorbing particles, implicating an enhancement of loss mechanisms due to NC interactions. Finally, measurements that simultaneously provide orientation and SR localization information about single NCs and NC clusters open up a new approach to studying behaviors. The basic orientation signatures of single NCs were established using a custom implementation of a dipole SR algorithm. ET from small clusters and their orientation features were observed. Additional orientation studies may provide the means to identify if neighboring NCs produce local electronic environments that affect the emission behavior of the other NCs. A framework with which to interpret SR

results that incorporates position and intensity distributions was presented and applied to identify individual donor/acceptor roles within clusters. Small clusters produce signatures that can be easily interpreted; however, in general, large clusters contain too many emission configurations to indicate specific roles even with SEM geometry verification. Analysis of large clusters turns into the task of identifying hot-spots and regions of high fluorescence activity.

This research could be extended with improvements to samples and sample preparation, instrumentation and experimental considerations, and advanced analysis methods. Through the characterization of the NCs and clusters, it is clear that variations of fluorescence behavior due to random particle orientation can be obscured by broad distributions of other NC properties. Shell thickness and irregular shell growth contribute significantly to observing a broad distribution of ET rates. Using high-quality NCs could help narrow down the number of additional considerations that could contribute to the observed behaviors. If preparation methods were adopted that provided highly monodisperse cluster sizes, samples of each cluster type could be independently studied in detail, drawing from large numbers of examples of similar cluster types.

Instrumentation enables the types of measurements that can be obtained. Changes to the SR measurement to provide simultaneous spectral information by splitting the image into a red and blue channel has already been suggested. This approach mirrors the additional information provided in the time-resolved confocal measurements of Chapter 5 by applying the same principle to spatially resolved measurements. To enhance the correlated experiment, a second fluorescence measurement of the same NCs on a time-resolved microscope could be incorporated. The lifetime information, combined with the SR and EM results, could match ET rates with specific geometries or provide another measure to sort out the

various emission configurations from larger clusters. Finally, the correlation method could be improved such that TEM correlation of the samples is possible. This would enable the study of orientated attachment effects for both slowly clustered and rapidly clustered samples and relate additional structure properties such as polycrystallinity or polytypism back to fluorescence behavior.

Analysis methods that eliminate selection bias or remove judgment-based interpretation are gaining popularity in a variety of single-molecule fields. Statically rigorous approaches are already making their way into NC blinking analysis[58, 43]. Unbiased intensity level selection from CP analysis was applied in Section 2.2, yielding different blinking statistics than traditional thresholding methods, and demonstrating what such approaches can contribute to the study of NCs.

Single-molecule experiments provide a variety of measurements that can benefit from alternative analysis tools. Binned data from time-resolved studies can produce fluorescence intensity traces, lifetime traces, and spectral traces. SR measurements produce traces of each position coordinate, intensity, and, when using dipole PSFs, orientation. Hidden Markov models (HMMs) are natural approaches to further process multiple correlated signals from SR analysis or time-resolved data of NC clusters. A Bayesian inference method based on a HMM[60–62] could be constructed for correlated experiments where the positions of the NCs are known and each emission configuration, including variants with and without ET, is a representation of a unique Markov state. Although Markov chains do not by definition describe NC blinking, which are power-law distributed as opposed to exponentially distributed, semi-Markov approaches such as Dewar *et al.*[63] that utilize explicit state-duration formalism can accommodate such blinking mechanisms. Correct model selection may indicate

donor/acceptor roles where each position coordinate is drawn from a distribution of variance determined by the localization precision from single NCs, and centered at the known position determined by SEM imaging. A more general inference implementation may not require explicit knowledge of the positions *a priori*, which could be applied to measurements from non-correlated experiments. With multiple measurements from each position coordinate, the intensity, and the two orientation angles, HMMs have the potential to dramatically improve interpretation of the various signatures from SR microscopy. The interpretation approach presented for SR results combined spatial distributions with intensity information. With small clusters, these interpretations may be simple. However, large clusters are often too complex to directly apply such logic and HMMs may yield relationships that cannot otherwise be easily distilled by simple visual inspection of the distributions.

Bibliography

[1] Xu, X.; Stöttinger, S.; Battagliarin, G.; Hinze, G.; Mugnaioli, E.; Li, C.; Müllen, K.; Basché, T. Assembly and Separation of Semiconductor Quantum Dot Dimers and Trimers. *Journal of the American Chemical Society* **2011**, *133*, 18062–18065.

[2] Tang, Z.; Kotov, N. A.; Giersig, M. Spontaneous Organization of Single CdTe Nanoparticles into Luminescent Nanowires. *Science* **2002**, *297*, 237–240.

[3] Cho, K.-S.; Talapin, D. V.; Gaschler, W.; Murray, C. B. Designing PbSe Nanowires and Nanorings through Oriented Attachment of Nanoparticles. *Journal of the American Chemical Society* **2005**, *127*, 7140–7147.

[4] Pradhan, N.; Xu, H.; Peng, X. Colloidal CdSe Quantum Wires by Oriented Attachment. *Nano Letters* **2006**, *6*, 720–724.

[5] Koh, W.-k.; Bartnik, A. C.; Wise, F. W.; Murray, C. B. Synthesis of Monodisperse PbSe Nanorods: A Case for Oriented Attachment. *Journal of the American Chemical Society* **2010**, *132*, 3909–3913.

[6] Bernardo, C.; Moura, I.; Fernández, Y. N.; Nunes-Pereira, E. J.; Coutinho, P. J. G.; Garcia, A. M. F.; Schellenberg, P.; Belsley, M.; Costa, M. F.; Stauber, T.; Vasilevskiy, M. I. Energy Transfer via Exciton Transport in Quantum Dot Based Self-Assembled Fractal Structures. *The Journal of Physical Chemistry C* **2014**, *118*, 4982–4990.

[7] Miller, J. B.; Dandu, N.; Velizhanin, K. A.; Anthony, R. J.; Kortshagen, U. R.; Kroll, D. M.; Kilina, S.; Hobbie, E. K. Enhanced Luminescent Stability through Particle Interactions in Silicon Nanocrystal Aggregates. *ACS Nano* **2015**, *9*, 9772–9782.

[8] Murray, C. B.; Kagan, C. R.; Bawendi, M. G. Self-organization of CdSe nanocrystallites into three-dimensional quantum dot superlattices. *Science* **1995**, *270*, 1335.

[9] Talapin, D. V.; Shevchenko, E. V.; Murray, C. B.; Titov, A. V.; Král, P. Dipole-Dipole Interactions in Nanoparticle Superlattices. *Nano Letters* **2007**, *7*, 1213–1219.

[10] Coe, S.; Woo, W.-K.; Bawendi, M.; Bulović, V. Electroluminescence from single monolayers of nanocrystals in molecular organic devices. *Nature* **2002**, *420*, 800–803.

[11] Anikeeva, P. O.; Halpert, J. E.; Bawendi, M. G.; Bulović, V. Electroluminescence from a Mixed Red-Green-Blue Colloidal Quantum Dot Monolayer. *Nano Letters* **2007**, *7*, 2196–2200.

[12] Achermann, M.; Petruska, M. A.; Crooker, S. A.; Klimov, V. I. Picosecond Energy Transfer in Quantum Dot Langmuir-Blodgett Nanoassemblies. *The Journal of Physical Chemistry B* **2003**, *107*, 13782–13787.

[13] Franzl, T.; Koktysh, D. S.; Klar, T. A.; Rogach, A. L.; Feldmann, J.; Gaponik, N. Fast energy transfer in layer-by-layer assembled CdTe nanocrystal bilayers. *Applied Physics Letters* **2004**, *84*, 2904–2906.

[14] Osovsky, R.; Shavel, A.; Gaponik, N.; Amirav, L.; Eychmüller, A.; Weller, H.; Lifshitz, E. Electrostatic and Covalent Interactions in CdTe Nanocrystalline Assemblies. *The Journal of Physical Chemistry B* **2005**, *109*, 20244–20250.

[15] Lunz, M.; Bradley, A. L.; Gerard, V. A.; Byrne, S. J.; Gun'ko, Y. K.; Lesnyak, V.; Gaponik, N. Concentration dependence of Förster resonant energy transfer between donor and acceptor nanocrystal quantum dot layers: Effect of donor-donor interactions. *Physical Review B* **2011**, *83*, 115423.

[16] Yu, M.; Van Orden, A. Enhanced Fluorescence Intermittency of CdSe-ZnS Quantum-Dot Clusters. *Physical Review Letters* **2006**, *97*, 237402.

[17] Koberling, F.; Mews, A.; Philipp, G.; Kolb, U.; Potapova, I.; Burghard, M.; Basché, T. Fluorescence spectroscopy and transmission electron microscopy of the same isolated semiconductor nanocrystals. *Applied Physics Letters* **2002**, *81*, 1116–1118.

[18] Koberling, F.; Kolb, U.; Philipp, G.; Potapova, I.; Basché, T.; Mews, A. Fluorescence Anisotropy and Crystal Structure of Individual Semiconductor Nanocrystals. *The Journal of Physical Chemistry B* **2003**, *107*, 7463–7471.

[19] Orfield, N. J.; McBride, J. R.; Keene, J. D.; Davis, L. M.; Rosenthal, S. J. Correlation of Atomic Structure and Photoluminescence of the Same Quantum Dot: Pinpointing Surface and Internal Defects That Inhibit Photoluminescence. *ACS Nano* **2014**, *9*, 831–839.

[20] Orfield, N. J.; McBride, J. R.; Wang, F.; Buck, M. R.; Keene, J. D.; Reid, K. R.; Htoon, H.; Hollingsworth, J. A.; Rosenthal, S. J. Quantum Yield Heterogeneity among Single Nonblinking Quantum Dots Revealed by Atomic Structure-Quantum Optics Correlation. *ACS Nano* **2016**, *10*, 1960–1968.

[21] Shepherd, D. Extending Single Molecule Spectroscopic Techniques to Multi-particle Systems of Semiconductor Nanocrystals. Ph.D. thesis, Colorado State University, Fort Collins, CO, 2011.

[22] Whitcomb, K. J. Energy transfer interactions with single molecule phenomena in small clusters of quantum dots. Ph.D. thesis, Colorado State University, Fort Collins, CO, 2014.

[23] Bae, W. K.; Padilha, L. A.; Park, Y.-S.; McDaniel, H.; Robel, I.; Pietryga, J. M.; Klimov, V. I. Controlled Alloying of the Core–Shell Interface in CdSe/CdS Quantum Dots for Suppression of Auger Recombination. *ACS Nano* **2013**, *7*, 3411–3419.

[24] Bullen, C.; Mulvaney, P. The Effects of Chemisorption on the Luminescence of CdSe Quantum Dots. *Langmuir* **2006**, *22*, 3007–3013.

[25] Owen, J. S.; Park, J.; Trudeau, P.-E.; Alivisatos, A. P. Reaction Chemistry and Ligand Exchange at Cadmium-Selenide Nanocrystal Surfaces. *Journal of the American Chemical Society* **2008**, *130*, 12279–12281.

[26] Fritzinger, B.; Capek, R. K.; Lambert, K.; Martins, J. C.; Hens, Z. Utilizing Self-Exchange To Address the Binding of Carboxylic Acid Ligands to CdSe Quantum Dots. *Journal of the American Chemical Society* **2010**, *132*, 10195–10201.

[27] Knittel, F.; Gravel, E.; Cassette, E.; Pons, T.; Pillon, F.; Dubertret, B.; Doris, E. On the Characterization of the Surface Chemistry of Quantum Dots. *Nano Letters* **2013**, *13*, 5075–5078.

[28] Mahler, B.; Lequeux, N.; Dubertret, B. Ligand-Controlled Polytypism of Thick-Shell CdSe/CdS Nanocrystals. *Journal of the American Chemical Society* **2010**, *132*, 953–959.

[29] Ekimov, A. I.; Kudryavtsev, I. A.; Efros, A. L.; Yazeva, T. V.; Hache, F.; Schanne-Klein, M. C.; Rodina, A. V.; Ricard, D.; Flytzanis, C. Absorption and intensity-dependent photoluminescence measurements on CdSe quantum dots: assignment of the first electronic transitions. *Journal of the Optical Society of America B* **1993**, *10*, 100.

[30] Norris, D. J.; Bawendi, M. G. Measurement and assignment of the size-dependent optical spectrum in CdSe quantum dots. *Physical Review B* **1996**, *53*, 16338–16346.

[31] Empedocles, S.; Bawendi, M. Spectroscopy of Single CdSe Nanocrystallites. *Accounts of Chemical Research* **1999**, *32*, 389–396.

[32] Neuhauser, R. G.; Shimizu, K. T.; Woo, W. K.; Empedocles, S. A.; Bawendi, M. G. Correlation between Fluorescence Intermittency and Spectral Diffusion in Single Semiconductor Quantum Dots. *Physical Review Letters* **2000**, *85*, 3301.

[33] van Sark, W. G. J. H. M.; Frederix, P. L. T. M.; Van den Heuvel, D. J.; Gerritsen, H. C.; Bol, A. A.; van Lingen, J. N. J.; de Mello Donegá, C.; Meijerink, A. Photooxidation and Photobleaching of Single CdSe/ZnS Quantum Dots Probed by Room-Temperature Time-Resolved Spectroscopy. *The Journal of Physical Chemistry B* **2001**, *105*, 8281–8284.

[34] van Sark, W. G. J. H. M.; Frederix, P. L. T. M.; Bol, A. A.; Gerritsen, H. C.; Meijerink, A. Blueing, Bleaching, and Blinking of Single CdSe/ZnS Quantum Dots. *ChemPhysChem* **2002**, *3*, 871–879.

[35] Nirmal, M.; Norris, D. J.; Kuno, M.; Bawendi, M. G.; Efros, A. L.; Rosen, M. Observation of the "Dark Exciton" in CdSe Quantum Dots. *Physical Review Letters* **1995**, *75*, 3728–3731.

[36] Nirmal, M.; Dabbousi, B. O.; Bawendi, M. G.; Macklin, J. J.; Trautman, J. K.; Harris, T. D.; Brus, L. E. Fluorescence intermittency in single cadmium selenide nanocrystals. *Nature* **1996**, *383*, 802–804.

[37] Kuno, M.; Fromm, D. P.; Hamann, H. F.; Gallagher, A.; Nesbitt, D. J. Nonexponential "blinking" kinetics of single CdSe quantum dots: A universal power law behavior. *The Journal of Chemical Physics* **2000**, *112*, 3117–3120.

[38] Kuno, M.; Fromm, D. P.; Hamann, H. F.; Gallagher, A.; Nesbitt, D. J. "On"/"off" fluorescence intermittency of single semiconductor quantum dots. *The Journal of Chemical Physics* **2001**, *115*, 1028–1040.

[39] Cichos, F.; von Borczyskowski, C.; Orrit, M. Power-law intermittency of single emitters. *Current Opinion in Colloid & Interface Science* **2007**, *12*, 272–284.

[40] Heyes, C. D.; Kobitski, A. Y.; Breus, V. V.; Nienhaus, G. U. Effect of the shell on the blinking statistics of core-shell quantum dots: A single-particle fluorescence study. *Physical Review B* **2007**, *75*, 125431.

[41] Sher, P. H.; Smith, J. M.; Dalgarno, P. A.; Warburton, R. J.; Chen, X.; Dobson, P. J.; Daniels, S. M.; Pickett, N. L.; O'Brien, P. Power law carrier dynamics in semiconductor nanocrystals at nanosecond timescales. *Applied Physics Letters* **2008**, *92*, 101111.

[42] Rabouw, F. T.; Kamp, M.; van Dijk-Moes, R. J. A.; Gamelin, D. R.; Koenderink, A. F.; Meijerink, A.; Vanmaekelbergh, D. Delayed Exciton Emission and Its Relation to Blinking in CdSe Quantum Dots. *Nano Letters* **2015**, *15*, 7718–7725.

[43] Riley, E. A.; Hess, C. M.; Whitham, P. J.; Reid, P. J. Beyond power laws: A new approach for analyzing single molecule photoluminescence intermittency. *The Journal of Chemical Physics* **2012**, *136*, 184508.

[44] Gómez, D. E.; van Embden, J.; Jasieniak, J.; Smith, T. A.; Mulvaney, P. Blinking and Surface Chemistry of Single CdSe Nanocrystals. *Small* **2006**, *2*, 204–208.

[45] Kim, Y.; Song, N. W.; Yu, H.; Moon, D. W.; Lim, S. J.; Kim, W.; Yoon, H.-J.; Shin, S. K. Ligand-dependent blinking of zinc-blende CdSe/ZnS core/shell nanocrystals. *Physical Chemistry Chemical Physics* **2009**, *11*, 3497–3502.

[46] Shimizu, K. T.; Neuhauser, R. G.; Leatherdale, C. A.; Empedocles, S. A.; Woo, W. K.; Bawendi, M. G. Blinking statistics in single semiconductor nanocrystal quantum dots. *Physical Review B* **2001**, *63*, 205316.

[47] Verberk, R.; Chon, J. W. M.; Gu, M.; Orrit, M. Environment-dependent blinking of single semiconductor nanocrystals and statistical aging of ensembles. *Physica E: Low-dimensional Systems and Nanostructures* **2005**, *26*, 19–23.

[48] Bharadwaj, P.; Novotny, L. Robustness of Quantum Dot Power-Law Blinking. *Nano Letters* **2011**, *11*, 2137–2141.

[49] Issac, A.; Krasselt, C.; Cichos, F.; von Borczyskowski, C. Influence of the Dielectric Environment on the Photoluminescence Intermittency of CdSe Quantum Dots. *ChemPhysChem* **2012**, *13*, 3223–3230.

[50] Knappenberger, K. L.; Wong, D. B.; Romanyuk, Y. E.; Leone, S. R. Excitation Wavelength Dependence of Fluorescence Intermittency in CdSe/ZnS Core/Shell Quantum Dots. *Nano Letters* **2007**, *7*, 3869–3874.

[51] Goushi, K.; Yamada, T.; Otomo, A. Excitation Intensity Dependence of Power-Law Blinking Statistics in Nanocrystal Quantum Dots. *The Journal of Physical Chemistry C* **2009**, *113*, 20161–20168.

[52] Amecke, N.; Heber, A.; Cichos, F. Distortion of power law blinking with binning and thresholding. *The Journal of Chemical Physics* **2014**, *140*, 114306.

[53] Crouch, C. H.; Sauter, O.; Wu, X.; Purcell, R.; Querner, C.; Drndic, M.; Pelton, M. Facts and Artifacts in the Blinking Statistics of Semiconductor Nanocrystals. *Nano Letters* **2010**, *10*, 1692–1698.

[54] Clauset, A.; Shalizi, C. R.; Newman, M. E. J. *Power-law distributions in empirical data*; arXiv e-print 0706.1062, 2007; SIAM Review 51, 661-703 (2009).

[55] Pelton, M.; Grier, D. G.; Guyot-Sionnest, P. Characterizing quantum-dot blinking using noise power spectra. *Applied Physics Letters* **2004**, *85*, 819–821.

[56] Pelton, M.; Smith, G.; Scherer, N. F.; Marcus, R. A. Evidence for a diffusion-controlled mechanism for fluorescence blinking of colloidal quantum dots. *Proceedings of the National Academy of Sciences* **2007**, *104*, 14249–14254.

[57] Houel, J.; Doan, Q. T.; Cajgfinger, T.; Ledoux, G.; Amans, D.; Aubret, A.; Dominjon, A.; Ferriol, S.; Barbier, R.; Nasilowski, M.; Lhuillier, E.; Dubertret, B.; Dujardin, C.; Kulzer, F. Autocorrelation Analysis for the Unbiased Determination of Power-Law Exponents in Single-Quantum-Dot Blinking. *ACS Nano* **2014**,

[58] Zhang, K.; Chang, H.; Fu, A.; Alivisatos, A.; Yang, H. Continuous Distribution of Emission States from Single CdSe/ZnS Quantum Dots. *Nano Letters* **2006**, *6*, 843–847.

[59] Schmidt, R.; Krasselt, C.; Göhler, C.; von Borczyskowski, C. The Fluorescence Intermittency for Quantum Dots Is Not Power-Law Distributed: A Luminescence Intensity Resolved Approach. *ACS Nano* **2014**, *8*, 3506–3521.

[60] Hines, K. E.; Bankston, J. R.; Aldrich, R. W. Analyzing Single-Molecule Time Series via Nonparametric Bayesian Inference. *Biophysical Journal* **2015**, *108*, 540–556.

[61] van de Meent, J.-W.; Bronson, J. E.; Wood, F.; Gonzalez Jr., R. L.; Wiggins, C. H. Hierarchically-coupled hidden Markov models for learning kinetic rates from single-molecule data. *ArXiv e-prints* **2013**, arXiv: 1305.3640.

[62] van de Meent, J.-W.; Bronson, J. E.; Wiggins, C. H.; Gonzalez Jr., R. L. Empirical Bayes Methods Enable Advanced Population-Level Analyses of Single-Molecule FRET Experiments. *Biophysical Journal* **2014**, *106*, 1327–1337.

[63] Dewar, M.; Wiggins, C.; Wood, F. Inference in Hidden Markov Models with Explicit State Duration Distributions. *IEEE Signal Processing Letters* **2012**, *19*, 235–238.

[64] Watkins, L. P.; Yang, H. Detection of Intensity Change Points in Time-Resolved Single-Molecule Measurements. *The Journal of Physical Chemistry B* **2005**, *109*, 617–628.

[65] Terentyeva, T. G.; Engelkamp, H.; Rowan, A. E.; Komatsuzaki, T.; Hofkens, J.; Li, C.-B.; Blank, K. Dynamic Disorder in Single-Enzyme Experiments: Facts and Artifacts. *ACS Nano* **2012**, *6*, 346–354.

[66] Frantsuzov, P.; Kuno, M.; Jankó, B.; Marcus, R. A. Universal emission intermittency in quantum dots, nanorods and nanowires. *Nature Physics* **2008**, *4*, 519–522.

[67] Cordones, A. A.; Leone, S. R. Mechanisms for charge trapping in single semiconductor nanocrystals probed by fluorescence blinking. *Chemical Society Reviews* **2013**, *42*, 3209–3221.

[68] Schmidt, R.; Krasselt, C.; von Borczyskowski, C. Change point analysis of matrix dependent photoluminescence intermittency of single CdSe/ZnS quantum dots with intermediate intensity levels. *Chemical Physics* **2012**, *406*, 9–14.

[69] Verberk, R.; van Oijen, A. M.; Orrit, M. Simple model for the power-law blinking of single semiconductor nanocrystals. *Physical Review B* **2002**, *66*, 233202.

[70] Verberk, R.; Orrit, M. Photon statistics in the fluorescence of single molecules and nanocrystals: Correlation functions versus distributions of on- and off-times. *The Journal of Chemical Physics* **2003**, *119*, 2214–2222.

[71] Kuno, M.; Fromm, D. P.; Johnson, S. T.; Gallagher, A.; Nesbitt, D. J. Modeling distributed kinetics in isolated semiconductor quantum dots. *Physical Review B* **2003**, *67*, 125304.

[72] Tang, J.; Marcus, R. A. Mechanisms of fluorescence blinking in semiconductor nanocrystal quantum dots. *The Journal of Chemical Physics* **2005**, *123*, 054704.

[73] Tang, J.; Marcus, R. A. Diffusion-Controlled Electron Transfer Processes and Power-Law Statistics of Fluorescence Intermittency of Nanoparticles. *Physical Review Letters* **2005**, *95*, 107401.

[74] Jha, P. P.; Guyot-Sionnest, P. Trion Decay in Colloidal Quantum Dots. *ACS Nano* **2009**, *3*, 1011–1015.

[75] Zhao, J.; Nair, G.; Fisher, B. R.; Bawendi, M. G. Challenge to the Charging Model of Semiconductor-Nanocrystal Fluorescence Intermittency from Off-State Quantum Yields and Multiexciton Blinking. *Physical Review Letters* **2010**, *104*, 157403.

[76] Frantsuzov, P. A.; Marcus, R. A. Explanation of quantum dot blinking without the long-lived trap hypothesis. *Physical Review B* **2005**, *72*, 155321.

[77] Frantsuzov, P. A.; Volkán-Kacsó, S.; Jankó, B. Model of Fluorescence Intermittency of Single Colloidal Semiconductor Quantum Dots Using Multiple Recombination Centers. *Physical Review Letters* **2009**, *103*, 207402.

[78] Galland, C.; Ghosh, Y.; Steinbruck, A.; Sykora, M.; Hollingsworth, J. A.; Klimov, V. I.; Htoon, H. Two types of luminescence blinking revealed by spectroelectrochemistry of single quantum dots. *Nature* **2011**, *479*, 203–207.

[79] Volkán-Kacsó, S.; Frantsuzov, P. A.; Jankó, B. Correlations between Subsequent Blinking Events in Single Quantum Dots. *Nano Letters* **2010**, *10*, 2761–2765.

[80] Bryant, G. W.; Jaskolski, W. Surface Effects on Capped and Uncapped Nanocrystals. *The Journal of Physical Chemistry B* **2005**, *109*, 19650–19656.

[81] Chen, Y.; Vela, J.; Htoon, H.; Casson, J. L.; Werder, D. J.; Bussian, D. A.; Klimov, V. I.; Hollingsworth, J. A. "Giant" Multishell CdSe Nanocrystal Quantum Dots with Suppressed Blinking. *Journal of the American Chemical Society* **2008**, *130*, 5026–5027.

[82] Smith, A. M.; Nie, S. Semiconductor Nanocrystals: Structure, Properties, and Band Gap Engineering. *Accounts of Chemical Research* **2009**, *43*, 190–200.

[83] Yoshikawa, N.; Hirori, H.; Watanabe, H.; Aoki, T.; Ihara, T.; Kusuda, R.; Wolpert, C.; Fujiwara, T. K.; Kusumi, A.; Kanemitsu, Y.; Tanaka, K. Biexciton state causes photoluminescence fluctuations in CdSe/ZnS core/shell quantum dots at high photoexcitation densities. *Physical Review B* **2013**, *88*, 155440.

[84] Shepherd, D. P.; Whitcomb, K. J.; Milligan, K. K.; Goodwin, P. M.; Gelfand, M. P.; Van Orden, A. Fluorescence Intermittency and Energy Transfer in Small Clusters of Semiconductor Quantum Dots. *The Journal of Physical Chemistry C* **2010**, *114*, 14831–14837.

[85] Whitcomb, K. J.; Geisenhoff, J. Q.; Ryan, D. P.; Gelfand, M. P.; Van Orden, A. Photon Antibunching in Small Clusters of CdSe/ZnS Core/Shell Quantum Dots. *The Journal of Physical Chemistry B* **2015**, *119*, 9020–9028.

[86] Tovstun, S. A.; Razumov, V. F. Theoretical analysis of nonradiative energy transfer in nanoclusters of quasi-monodisperse colloidal quantum dots. *High Energy Chemistry* **2015**, *49*, 352–360.

[87] Whitcomb, K. J.; Ryan, D. P.; Gelfand, M. P.; Van Orden, A. Blinking Statistics of Small Clusters of Semiconductor Nanocrystals. *The Journal of Physical Chemistry C* **2013**, *117*, 25761–25768.

[88] Kagan, C. R.; Murray, C. B.; Nirmal, M.; Bawendi, M. G. Electronic Energy Transfer in CdSe Quantum Dot Solids. *Physical Review Letters* **1996**, *76*, 1517.

[89] Kagan, C. R. Long-range resonance transfer of electronic excitations in close-packed CdSe quantum-dot solids. *Physical Review B* **1996**, *54*, 8633–8643.

[90] Crooker, S. A. Spectrally Resolved Dynamics of Energy Transfer in Quantum-Dot Assemblies: Towards Engineered Energy Flows in Artificial Materials. *Physical Review Letters* **2002**, *89*.

[91] Förster, T. Zwischenmolekulare Energiewanderung und Fluoreszenz. *Annalen der Physik* **1948**, *437*, 55–75.

[92] Dexter, D. L. A Theory of Sensitized Luminescence in Solids. *The Journal of Chemical Physics* **1953**, *21*, 836–850.

[93] Curutchet, C.; Franceschetti, A.; Zunger, A.; Scholes, G. D. Examining Förster Energy Transfer for Semiconductor Nanocrystalline Quantum Dot Donors and Acceptors. *The Journal of Physical Chemistry C* **2008**, *112*, 13336–13341.

[94] Mork, A. J.; Weidman, M. C.; Prins, F.; Tisdale, W. A. Magnitude of the Förster Radius in Colloidal Quantum Dot Solids. *The Journal of Physical Chemistry C* **2014**, *118*, 13920–13928.

[95] Hoffman, J. B.; Choi, H.; Kamat, P. V. Size-Dependent Energy Transfer Pathways in CdSe Quantum Dot–Squaraine Light-Harvesting Assemblies: Förster versus Dexter. *The Journal of Physical Chemistry C* **2014**, *118*, 18453–18461.

[96] Scholes, G. D.; Andrews, D. L. Resonance energy transfer and quantum dots. *Physical Review B* **2005**, *72*, 125331.

[97] Allan, G.; Delerue, C. Energy transfer between semiconductor nanocrystals: Validity of Förster's theory. *Physical Review B* **2007**, *75*, 195311.

[98] Baer, R.; Rabani, E. Theory of resonance energy transfer involving nanocrystals: The role of high multipoles. *The Journal of Chemical Physics* **2008**, *128*, 184710.

[99] Samosvat, D. M.; Chikalova-Luzina, O. P.; Zegrya, G. G. Nonradiative resonance energy transfer between semiconductor quantum dots. *Journal of Experimental and Theoretical Physics* **2015**, *121*, 76–95.

[100] Efros, A. L. Luminescence polarization of CdSe microcrystals. *Physical Review B* **1992**, *46*, 7448–7458.

[101] Efros, A. L.; Rosen, M.; Kuno, M.; Nirmal, M.; Norris, D. J.; Bawendi, M. Band-edge exciton in quantum dots of semiconductors with a degenerate valence band: Dark and bright exciton states. *Physical Review B* **1996**, *54*, 4843–4856.

[102] Cyphersmith, A.; Early, K.; Maksov, A.; Graham, J.; Wang, Y.; Barnes, M. Disentangling the role of linear transition dipole in band-edge emission from single CdSe/ZnS quantum dots: Combined linear anisotropy and defocused emission pattern imaging. *Applied Physics Letters* **2010**, *97*, 121915.

[103] Kagan, C. R.; Murray, C. B. Charge transport in strongly coupled quantum dot solids. *Nature Nanotechnology* **2015**, *10*, 1013–1026.

[104] Li, H.; Zhitomirsky, D.; Dave, S.; Grossman, J. C. Toward the Ultimate Limit of Connectivity in Quantum Dots with High Mobility and Clean Gaps. *ACS Nano* **2016**, *10*, 606–614.

[105] Klokkenburg, M.; Houtepen, A. J.; Koole, R.; de Folter, J. W. J.; Erné, B. H.; van Faassen, E.; Vanmaekelbergh, D. Dipolar Structures in Colloidal Dispersions of PbSe and CdSe Quantum Dots. *Nano Letters* **2007**, *7*, 2931–2936.

[106] Shim, M.; Guyot-Sionnest, P. Permanent dipole moment and charges in colloidal semiconductor quantum dots. *The Journal of Chemical Physics* **1999**, *111*, 6955–6964.

[107] Rabani, E. Structure and electrostatic properties of passivated CdSe nanocrystals. *The Journal of Chemical Physics* **2001**, *115*, 1493–1497.

[108] Nann, T.; Schneider, J. Origin of permanent electric dipole moments in wurtzite nanocrystals. *Chemical Physics Letters* **2004**, *384*, 150–152.

[109] Sommer, C.; Straehle, C.; Koethe, U.; Hamprecht, F. A. "ilastik: Interactive Learning and Segmentation Toolkit". 8th IEEE International Symposium on Biomedical Imaging (ISBI 2011). 2011.

[110] Tinnefeld, P.; Herten, D.-P.; Sauer, M. Photophysical Dynamics of Single Molecules Studied by Spectrally-Resolved Fluorescence Lifetime Imaging Microscopy (SFLIM). *The Journal of Physical Chemistry A* **2001**, *105*, 7989–8003.

[111] Yildiz, A.; Forkey, J. N.; McKinney, S. A.; Ha, T.; Goldman, Y. E.; Selvin, P. R. Myosin V Walks Hand-Over-Hand: Single Fluorophore Imaging with 1.5-nm Localization. *Science* **2003**, *300*, 2061–2065.

[112] Thompson, R. E.; Larson, D. R.; Webb, W. W. Precise Nanometer Localization Analysis for Individual Fluorescent Probes. *Biophysical Journal* **2002**, *82*, 2775–2783.

[113] Betzig, E.; Patterson, G. H.; Sougrat, R.; Lindwasser, O. W.; Olenych, S.; Bonifacino, J. S.; Davidson, M. W.; Lippincott-Schwartz, J.; Hess, H. F. Imaging Intracellular Fluorescent Proteins at Nanometer Resolution. *Science* **2006**, *313*, 1642–1645.

[114] Rust, M. J.; Bates, M.; Zhuang, X. Sub-diffraction-limit imaging by stochastic optical reconstruction microscopy (STORM). *Nature Methods* **2006**, *3*, 793–796.

[115] Deschout, H.; Zanacchi, F. C.; Mlodzianoski, M.; Diaspro, A.; Bewersdorf, J.; Hess, S. T.; Braeckmans, K. Precisely and accurately localizing single emitters in fluorescence microscopy. *Nature Methods* **2014**, *11*, 253–266.

[116] Small, A.; Stahlheber, S. Fluorophore localization algorithms for super-resolution microscopy. *Nature Methods* **2014**, *11*, 267–279.

[117] Han, J. J.; Kunde, Y. A.; Hong-Geller, E.; Werner, J. H. Actin restructuring during Salmonella typhimurium infection investigated by confocal and super-resolution microscopy. *Journal of Biomedical Optics* **2014**, *19*, 016011.

[118] Smith, C. S.; Joseph, N.; Rieger, B.; Lidke, K. A. Fast, single-molecule localization that achieves theoretically minimum uncertainty. *Nature Methods* **2010**, *7*, 373–375.

[119] Aguet, F.; Geissbühler, S.; Märki, I.; Lasser, T.; Unser, M. Super-resolution orientation estimation and localization of fluorescent dipoles using 3-D steerable filters. *Optics Express* **2009**, *17*, 6829.

[120] Aguet, F. Super-Resolution Fluorescence Microscopy Based on Physical Models. Ph.D. thesis, École Polytechnique Fédéral de Lausanne, Lausanne, 2009.

[121] Mortensen, K. I.; Churchman, L. S.; Spudich, J. A.; Flyvbjerg, H. Optimized localization analysis for single-molecule tracking and super-resolution microscopy. *Nature Methods* **2010**, *7*, 377–381.

[122] Enderlein, J.; Toprak, E.; Selvin, P. R. Polarization effect on position accuracy of fluorophore localization. *Optics Express* **2006**, *14*, 8111.

[123] Engelhardt, J.; Keller, J.; Hoyer, P.; Reuss, M.; Staudt, T.; Hell, S. W. Molecular Orientation Affects Localization Accuracy in Superresolution Far-Field Fluorescence Microscopy. *Nano Letters* **2011**, *11*, 209–213.

[124] Richards, B.; Wolf, E. Electromagnetic Diffraction in Optical Systems. II. Structure of the Image Field in an Aplanatic System. *Proceedings of the Royal Society of London A: Mathematical, Physical and Engineering Sciences* **1959**, *253*, 358–379.

[125] Stetson, P. B. DAOPHOT: A computer program for crowded-field stellar photometry. *Publications of the Astronomical Society of the Pacific* **1987**, *99*, 191–222.

[126] Holden, S. J.; Uphoff, S.; Kapanidis, A. N. DAOSTORM: an algorithm for high-density super-resolution microscopy. *Nature Methods* **2011**, *8*, 279–280.

[127] Erdélyi, M.; Sinkó, J.; Kákonyi, R.; Kelemen, A.; Rees, E.; Varga, D.; Szabó, G. Origin and compensation of imaging artefacts in localization-based super-resolution microscopy. *Methods* **2015**, *88*, 122–132.

[128] Myung, I. J. Tutorial on maximum likelihood estimation. *Journal of Mathematical Psychology* **2003**, *47*, 90–100.

[129] Hynecek, J.; Nishiwaki, T. Excess noise and other important characteristics of low light level imaging using charge multiplying CCDs. *IEEE Transactions on Electron Devices* **2003**, *50*, 239–245.

[130] Hirsch, M.; Wareham, R. J.; Martin-Fernandez, M. L.; Hobson, M. P.; Rolfe, D. J. A Stochastic Model for Electron Multiplication Charge-Coupled Devices—From Theory to Practice. *PLoS ONE* **2013**, *8*, e53671.

[131] Chao, J.; Sally Ward, E.; Ober, R. J. Fisher information theory for parameter estimation in single molecule microscopy: tutorial. *Journal of the Optical Society of America A* **2016**, *33*, B36.

[132] Huang, F.; Schwartz, S. L.; Byars, J. M.; Lidke, K. A. Simultaneous multiple-emitter fitting for single molecule super-resolution imaging. *Biomedical Optics Express* **2011**, *2*, 1377–1393.

[133] Krull, A.; Steinborn, A.; Ananthanarayanan, V.; Ramunno-Johnson, D.; Petersohn, U.; Tolić-Nørrelykke, I. M. A divide and conquer strategy for the maximum likelihood localization of low intensity objects. *Optics Express* **2014**, *22*, 210.

[134] Ruckebusch, C.; Bernex, R.; Allegrini, F.; Sliwa, M.; Hofkens, J.; Dedecker, P. Mapping Pixel Dissimilarity in Wide-Field Super-Resolution Fluorescence Microscopy. *Analytical Chemistry* **2015**,

[135] Dertinger, T.; Colyer, R.; Iyer, G.; Weiss, S.; Enderlein, J. Fast, background-free, 3D super-resolution optical fluctuation imaging (SOFI). *Proceedings of the National Academy of Sciences* **2009**, *106*, 22287–22292.

[136] Kouskousis, B. P.; van Embden, J.; Morrish, D.; Russell, S. M.; Gu, M. Super-resolution imaging and statistical analysis of CdSe/CdS Core/Shell semiconductor nanocrystals. *Journal of Biophotonics* **2010**, *3*, 437–445.

[137] Chien, F.-C.; Kuo, C. W.; Chen, P. Localization imaging using blinking quantum dots. *The Analyst* **2011**, *136*, 1608.

[138] Mukamel, E. A.; Babcock, H.; Zhuang, X. Statistical Deconvolution for Superresolution Fluorescence Microscopy. *Biophysical Journal* **2012**, *102*, 2391–2400.

[139] Wang, Y.; Fruhwirth, G.; Cai, E.; Ng, T.; Selvin, P. R. 3D Super-Resolution Imaging with Blinking Quantum Dots. *Nano Letters* **2013**, *13*, 5233–5241.

[140] Hyvarinen, A. Fast and robust fixed-point algorithms for independent component analysis. *IEEE Transactions on Neural Networks* **1999**, *10*, 626–634.

[141] Lidke, K. A.; Rieger, B.; Jovin, T. M.; Heintzmann, R. Superresolution by localization of quantum dots using blinking statistics. *Optics Express* **2005**, *13*, 7052.

[142] Barsic, A.; Piestun, R. Super-resolution of dense nanoscale emitters beyond the diffraction limit using spatial and temporal information. *Applied Physics Letters* **2013**, *102*, 231103.

[143] Mandula, O. Super-resolution methods for fluorescence microscopy. Ph.D. thesis, The University of Edinburgh, 2013.

[144] Mandula, O.; Šestak, I. Š.; Heintzmann, R.; Williams, C. K. I. Localisation microscopy with quantum dots using non-negative matrix factorisation. *Optics Express* **2014**, *22*, 24594.

[145] Geissbuehler, S.; Bocchio, N. L.; Dellagiacoma, C.; Berclaz, C.; Leutenegger, M.; Lasser, T. Mapping molecular statistics with balanced super-resolution optical fluctuation imaging (bSOFI). *Optical Nanoscopy* **2012**, *1*, 4.

[146] Ware, W. R.; Doemeny, L. J.; Nemzek, T. L. Deconvolution of fluorescence and phosphorescence decay curves. Least-squares method. *J. Phys. Chem.* **1973**, *77*, 2038–2048.

[147] O'Connor, D. V.; Ware, W. R.; Andre, J. C. Deconvolution of fluorescence decay curves. A critical comparison of techniques. *The Journal of Physical Chemistry* **1979**, *83*, 1333–1343.

[148] Miyazaki, J.; Kinoshita, S.; Jin, T. Non-radiative exciton recombination through excitation energy transfer in quantum dot clusters. *Journal of Luminescence* **2011**, *131*, 539–542.

[149] Fernée, M. J.; Plakhotnik, T.; Louyer, Y.; Littleton, B. N.; Potzner, C.; Tamarat, P.; Mulvaney, P.; Lounis, B. Spontaneous Spectral Diffusion in CdSe Quantum Dots. *The Journal of Physical Chemistry Letters* **2012**, *3*, 1716–1720.

[150] Beyler, A. P.; Marshall, L. F.; Cui, J.; Brokmann, X.; Bawendi, M. G. Direct Observation of Rapid Discrete Spectral Dynamics in Single Colloidal CdSe-CdS Core-Shell Quantum Dots. *Physical Review Letters* **2013**, *111*, 177401.

[151] Braam, D.; Mölleken, A.; Prinz, G.; Notthoff, C.; Geller, M.; Lorke, A. Role of the ligand layer for photoluminescence spectral diffusion of CdSe/ZnS nanoparticles. *Physical Review B* **2013**, *88*, 125302.

[152] Türck, V.; Rodt, S.; Stier, O.; Heitz, R.; Engelhardt, R.; Pohl, U. W.; Bimberg, D.; Steingrüber, R. Effect of random field fluctuations on excitonic transitions of individual CdSe quantum dots. *Physical Review B* **2000**, *61*, 9944–9947.

[153] Yalcin, S. E.; Labastide, J. A.; Sowle, D. L.; Barnes, M. D. Spectral Properties of Multiply Charged Semiconductor Quantum Dots. *Nano Lett.* **2011**, *11*, 4425–4430.

[154] Empedocles, S. A.; Norris, D. J.; Bawendi, M. G. Photoluminescence Spectroscopy of Single CdSe Nanocrystallite Quantum Dots. *Physical Review Letters* **1996**, *77*, 3873–3876.

[155] Seufert, J.; Obert, M.; Scheibner, M.; Gippius, N. A.; Bacher, G.; Forchel, A.; Passow, T.; Leonardi, K.; Hommel, D. Stark effect and polarizability in a single CdSe/ZnSe quantum dot. *Applied Physics Letters* **2001**, *79*, 1033–1035.

[156] Wen, G. W.; Lin, J. Y.; Jiang, H. X.; Chen, Z. Quantum-confined Stark effects in semiconductor quantum dots. *Physical Review B* **1995**, *52*, 5913–5922.

[157] Ihara, T.; Kanemitsu, Y. Spectral diffusion of neutral and charged exciton transitions in single CdSe/ZnS nanocrystals due to quantum-confined Stark effect. *Physical Review B* **2014**, *90*, 195302.

[158] Wang, S.; Querner, C.; Fischbein, M. D.; Willis, L.; Novikov, D. S.; Crouch, C. H.; Drndic, M. Blinking Statistics Correlated with Nanoparticle Number. *Nano Letters* **2008**, *8*, 4020–4026.

[159] Wang, S.; Querner, C.; Dadosh, T.; Crouch, C. H.; Novikov, D. S.; Drndic, M. Collective fluorescence enhancement in nanoparticle clusters. *Nature Communications* **2011**, *2*, 364.

[160] Weber, M. L.; Willets, K. A. Correlated Super-Resolution Optical and Structural Studies of Surface-Enhanced Raman Scattering Hot Spots in Silver Colloid Aggregates. *The Journal of Physical Chemistry Letters* **2011**, *2*, 1766–1770.

[161] Ryan, D. P.; Goodwin, P. M.; Sheehan, C. J.; Whitcomb, K. J.; Gelfand, M. P.; Van Orden, A. Correlating structure and fluorescence dynamics of quantum dot clusters using super-resolution imaging. SPIE BiOS. 2016; pp 97140T–97140T.

[162] Ovesný, M.; Křížek, P.; Borkovec, J.; Svindrych, Z.; Hagen, G. M. ThunderSTORM: a comprehensive ImageJ plug-in for PALM and STORM data analysis and super-resolution imaging. *Bioinformatics (Oxford, England)* **2014**, *30*, 2389–2390.

[163] Brokmann, X.; Coolen, L.; Hermier, J.-P.; Dahan, M. Emission properties of single CdSe/ZnS quantum dots close to a dielectric interface. *Chemical Physics* **2005**, *318*, 91–98.

[164] Brokmann, X.; Ehrensperger, M.-V.; Hermier, J.-P.; Triller, A.; Dahan, M. Orientational imaging and tracking of single CdSe nanocrystals by defocused microscopy. *Chemical Physics Letters* **2005**, *406*, 210–214.

[165] Schuster, R.; Barth, M.; Gruber, A.; Cichos, F. Defocused wide field fluorescence imaging of single CdSe/ZnS quantum dots. *Chemical Physics Letters* **2005**, *413*, 280–283.

[166] Chen, X.-J.; Xu, Y.; Lan, S.; Dai, Q.-F.; Lin, X.-S.; Guo, Q.; Wu, L.-J. Rotation of defocused wide-field fluorescence images after blinking in single CdSe/ZnS core-shell quantum dots. *Physical Review B* **2009**, *79*, 115312.

[167] Taylor, J. N.; Makarov, D. E.; Landes, C. F. Denoising Single-Molecule FRET Trajectories with Wavelets and Bayesian Inference. *Biophysical Journal* **2010**, *98*, 164–173.

[168] Taylor, J. N.; Landes, C. F. Improved Resolution of Complex Single-Molecule FRET Systems via Wavelet Shrinkage. *The Journal of Physical Chemistry B* **2011**, *115*, 1105–1114.

[169] Vaxenburg, R.; Rodina, A.; Lifshitz, E.; Efros, A. L. Biexciton Auger Recombination in CdSe/CdS Core/Shell Semiconductor Nanocrystals. *Nano Letters* **2016**, *16*, 2503–2511.

[170] Kurzmann, A.; Ludwig, A.; Wieck, A. D.; Lorke, A.; Geller, M. Auger Recombination in Self-Assembled Quantum Dots: Quenching and Broadening of the Charged Exciton Transition. *Nano Letters* **2016**,

[171] Park, Y.-S.; Malko, A. V.; Vela, J.; Chen, Y.; Ghosh, Y.; García-Santamaría, F.; Hollingsworth, J. A.; Klimov, V. I.; Htoon, H. Near-Unity Quantum Yields of Biexciton Emission from CdSe/CdS Nanocrystals Measured Using Single-Particle Spectroscopy. *Physical Review Letters* **2011**, *106*, 187401.

[172] Li, Q.; Chen, X.-J.; Xu, Y.; Lan, S.; Liu, H.-Y.; Dai, Q.-F.; Wu, L.-J. Photoluminescence Properties of the CdSe Quantum Dots Accompanied with Rotation of the Defocused Wide-Field Fluorescence Images. *The Journal of Physical Chemistry C* **2010**, *114*, 13427–13432.

[173] Enderlein, J. Theoretical study of detection of a dipole emitter through an objective with high numerical aperture. *Optics Letters* **2000**, *25*, 634.

[174] Böhmer, M.; Enderlein, J. Orientation imaging of single molecules by wide-field epifluorescence microscopy. *Journal of the Optical Society of America B* **2003**, *20*, 554–559.

[175] Patra, D.; Gregor, I.; Enderlein, J. Image Analysis of Defocused Single-Molecule Images for Three-Dimensional Molecule Orientation Studies. *The Journal of Physical Chemistry A* **2004**, *108*, 6836–6841.

[176] Goodwin, E. D.; Diroll, B. T.; Oh, S. J.; Paik, T.; Murray, C. B.; Kagan, C. R. Effects of Post-Synthesis Processing on CdSe Nanocrystals and Their Solids: Correlation between Surface Chemistry and Optoelectronic Properties. *The Journal of Physical Chemistry C* **2014**,

[177] Yu, W. W.; Qu, L.; Guo, W.; Peng, X. Experimental Determination of the Extinction Coefficient of CdTe, CdSe, and CdS Nanocrystals. *Chemistry of Materials* **2003**, *15*, 2854–2860.

[178] Leatherdale, C. A.; Woo, W.-K.; Mikulec, F. V.; Bawendi, M. G. On the Absorption Cross Section of CdSe Nanocrystal Quantum Dots. *J. Phys. Chem. B* **2002**, *106*, 7619–7622.

APPENDIX A

Sample Preparation Methods

For the studies detailed in this work, commercial NCs purchased from Ocean Nanotech were used (thick shell NCs: QSR-560 lot #101813, thin shell NCs: QSP-560 lot #031713). Many details about the synthesis process contribute to the fluorescence and ET properties of any NC and proper diligence in characterizing the particles should be undertaken for new batches of NCs. TEM characterization is ideal for identifying the basic distributions of particle size and shell thickness for a given batch as well as identifying systemic growth characteristics such as polycrystallinity and irregular shells.

A.1. Clustering Nanocrystals

There are a variety of methods to produce NC clusters from solutions of nominally monodisperse NCs (polydisperse solutions of NCs, as if engineering a driven ET experiment, are notoriously difficult to cluster as mixed species clusters due to the differing interaction rates between NCs of dissimilar size). In one approach that parallels the washing step used after synthesis, clustering is induced by adding a bad solvent to a solution of NCs. The details of the attachment mechanism are somewhat unknown; however, the ligands play a key role. It has been shown that the types of solvent and bad-solvent influence ligand coverage[176]. NCs suspended in hexane exhibit more stable ligand attachment compared to suspensions in toluene. Additionally, the bad solvent acetone is less effective at stripping away ligands than MeOH. Different ligands will also respond in subtly different ways. While clusters can be created with many combinations of good/bad solvent and ligand type, we focus on NCs suspended in toluene with octadecylamine ligands and clustered with MeOH.

The final state of attached NCs could potentially span from indirect attachment where the ligands are entangled to direct attachment where NC shells are in physical contact. The former is understandable if the bad solvent merely drives NCs into close proximity with one another and the latter occurs if significant numbers of ligand are stripped away by the bad solvent, leaving uncovered surfaces where attachment can occur. An evolution from entanglement to direct contact is also possible as ligands are known to diffuse across a NC surface, suggesting a cluster may "ripen" after formation. EM measurements could potentially characterize the final form of attachment. However, no strong evidence for a preferential attachment mode was found in the EM imaging of the cluster samples prepared in this study.

In addition to the types of solvents used to induce clustering, the conditions in which they are applied can affect the resulting clusters. Specifically, the NC concentration in the solvent and the relative concentrations of the good/bad solvents are two factors explored over the course of this work which produced similar clusters. Described in detail below are two methods applied here and the implications they may have on the resulting structures.

Slow clustering at low concentration: 5–10 μL of MeOH is mixed with 1000 μL of well-separated (single), nM concentrations of NCs in toluene for 15–20 mins. The relatively small amount of bad solvent and low NC particle density means that ligands are stripped away slowly (over several minutes) and/or the inter-particle interaction rate is small. Harvesting 50–100 μL of the in-process clustering solution and depositing onto a measurement substrate (glass or SiN grid) halts the clustering by changing the environment from solution, which contains the bad solvent, to a surface where the NCs become immobilized. Small clusters, comprised of 2–4 NCs, are obtained via this simple method while single NCs remain with good probability given these processing durations and MeOH concentrations. Clusters

of stable size cannot be produced with this approach since the clustering process is ongoing. Furthermore, because the starting concentrations must be in the nM range, EM imaging for characterization is difficult. Typically, μM–mM concentrations are ideal in EM imaging particles of this size because they are concentrated enough to easily locate within the limited field of view of an EM at the magnification required to visualize such small objects. However, clustering at these higher concentrations was not effective. While not explored in great detail, variations to this method at higher NC concentrations were found to either produce no significant clustering even after long soaking durations or resulted in massive clusters too large for single-molecule use.

Rapid clustering at high concentration: By using a high NC concentration solution and a high relative concentration of bad solvent, rapid precipitation can produce clusters. Because this approach actually precipitates the NCs out of solution, they can be dried and resuspended at high concentrations as clusters of stable size. The resulting cluster solutions have long shelf-lives (months) and can be easily imaged in EM without correlated measurements, making cluster characterization possible.

Following a clustering procedure similar to Xu *et al.*[1], stable clusters were formed by processing a batch of NCs through multiple crash cycles. Each crash cycle strips away an increasing number of ligands that are not replenished and, as the NCs settle, permanent attachments form. A crash cycle involves adding 800 μL of MeOH to 500 μL of NCs suspended in toluene. This mixture immediately becomes turbid. The NCs are then separated from the MeOH/toluene solvents by centrifuging the turbid mixture for 30 mins, removing the top mixed liquid layer, and resuspending the NCs in 500 μL of pure toluene. This process is done three times and, after a fourth and final cycle, the NCs—now fully formed clusters—are suspended in 500 μL of cyclohexane instead of toluene in preparation for matching the

top layer of the density gradient for ultra-centrifuge separation. 10 μL of a concentrated ligand/toluene solution was added to the final suspension to provide the NCs a saturated environment where ligands could reattach and passivate the surfaces depleted of covering ligand by the clustering process. This was done with the aim of suppressing additional clustering.

A.2. Ultra-centrifuge Separation

The rapid, high concentration clustering process produces a distribution of cluster sizes. Each rapidly clustered batch was further purified using density gradient ultra-centrifugation. This procedure involves setting up layers of variable density mixture in a centrifuge tube and carefully topping the stack with the solution to be separated. Spun at very high speeds to generate a large force on the suspended particles, the particles diffuse through the gradient layers at different rates according to their size. For the clusters in this work, the gradient layers were varying ratios of a cyclohexane/CCl_4 mixture. In 1/2 in. diameter thick-walled polyallomer centrifuge tubes, six 450 μL layers of cyclohexane/CCl_4 mixtures were deposited on top of one another. The gradient started at 90% CCl_4 on the bottom and decreased linearly to 40% CCl_4 at the top (90%, 80%, 70%, 60%, 50%, and 40%). 200 μL of the NCs, suspended in pure cyclohexane, would initially float on top of the denser gradient mixtures. The centrifuge tubes were spun at $45,000$ rpm for 15 mins. at 15° C.

The results from ultra-centrifugation are shown in Figure 2.7. In Figure 2.7A the dispersion of NCs after one cycle shows no clearly grouped bands. To improve purification, a second cycle was done by collecting 500 μL from the top (T), middle (M), and bottom (B) of the centrifuge tube and dried under vacuum to remove the particles from the density layer from which they were harvested. The NCs should not form larger clusters in dried form

because of the excess ligand added to the suspension earlier. Each of the dried solids (T, M, and B) were then separately resuspended in 250 μL of cyclohexane and the three solutions centrifuged again. Figure 2.7B shows the dispersions of each solution after the second ultra-centrifugation. While clearer separations appear to match the regions from which they were drawn in the previous purification. A third cycle was done in attempt to obtain better purification by combining the tops, middles, and bottoms of each into three separate solutions. Each solution was dried, resuspended, and centrifuged as before. The resulting dispersions, shown in Figure 2.7C, do not indicate significant improvement, so no further purification steps were done despite not achieving the clear banding demonstrated by other groups. To examine the purify of the various regions in each centrifuge tube, 450 μL was collected from the top of the top solution (TT), top of the middle solution (MT), middle of the middle solution (MM), and bottom of the bottom solution (BB), and 250 μL from the middle of the bottom solution (BM), this time keeping the solutions separate. These solutions were dried a final time to remove them from the gradient mixtures and then suspended in toluene with additional ligand to stabilize their fluorescence properties.

Each of the solutions (TT, MT, MM, BM, and BB) should consist of the same general cluster sizes. When examined on the confocal microscope, the TT and MT solutions were almost exclusively single NCs, as judged by their strict binary blinking, QYs consistent with single NCs from the original batch, and mono-exponential decay histograms. The BB solution was primarily very large clusters, similar to what is observed by letting the slow clustering method run for a long time. The solutions MM and BM were the most valuable because they consisted of small to moderate sized clusters. TEM characterization revealed a broad distribution of cluster sizes and shapes, ranging from dimers to heptamers. This indicates that while the centrifugation could separate medium sized clusters from singles

and very large clusters, for the samples produced for this study, it was not as effective at distilling dimers from trimers as was reported by Xu *et al.* The separation method likely could be optimized to obtain better purified cluster sizes by adjusting the concentrations and using more centrifuge cycles. Perhaps the clustering steps produced too broad an initial distribution of cluster sizes and separating such highly mixed solutions cannot be done at the high concentrations needed to visualize the bands under ultra-violet light after separation. While variations to both the clustering and separation methods were tried, a more concerted effort aiming at extracting purer sizes could produce samples of only dimers and trimers, which could be used to perform a more statistically comprehensive study of each type of cluster.

Figure A.1 shows the results after two ultra-centrifuge separation cycles on an acetone clustered batch. The bands are much better defined and comparable to what is reported by Xu *et al.* Because acetone removes fewer ligands than MeOH, smaller clusters are formed and the distribution of cluster sizes is likely much narrower. Using acetone would be an interesting approach to obtain high purity samples of dimers and trimers for future studies.

A.3. Fluorescence Microscopy Preparation

NCs were deposited onto two different substrates, depending on the type of measurement that was done. Confocal time-resolved and dipole orientation super-resolution imaging used untreated #1 glass coverslips. The correlated SEM/super-resolution measurements utilized SiN windowed grids (TEMwindows, SN100-A10Q33).

Glass coverslips: A solution of NCs or NC clusters was diluted in toluene to nM concentrations from a stock solution. Typically, this was $\sim 1 : 10^6$ for single NCs and

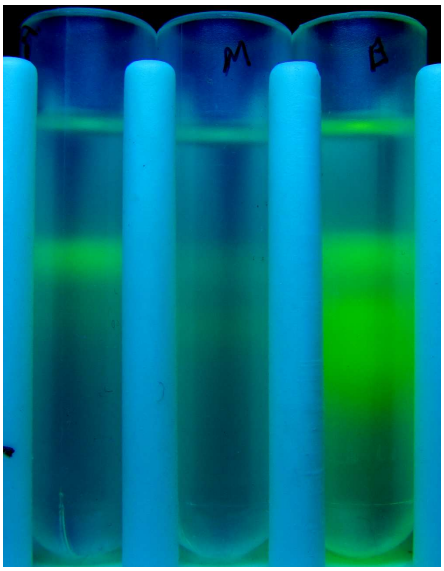

FIGURE A.1. Ultra-centrifuge separation of acetone clustered NCs after a single crashing cycle. Clearer separation bands appear compared to the same procedure in MeOH.

$\sim 1 : 10^3$ for the solutions from ultra-centrifugation. From a diluted solution, 100 μL was spin coated by dripping the solution slowly over a coverslip spinning at 5,000 rpm. The final coverslip samples were dried and kept in a vacuum environment until ready for fluorescence measurements.

SiN grids: NCs do not adhere well to bare SiN. To prepare the grids for NC deposition, a grid was placed in a vacuum desiccator alongside a small glass cap containing 50 μL of APTES and left under vacuum for at least two hours. Heating the glass slightly until the APTES began to wick up the sides of the cap before sealing it in the desiccator helped start the treatment process. NCs and NC clusters were diluted exactly as for the coverslip preparation and 100 μL of the final dilution was dripped onto a SiN grid spinning at 5,000 rpm. The grid was then dried and kept under vacuum until ready for measurement.

A blank #1 glass coverslip was first mounted on the fluorescence microscope and then the SiN grid placed directly on top with the coated surface facing the coverslip. This introduces a small air gap between the fluorescent NCs and the ideal imaging location at the surface

of the coverslip. This arrangement reduces collection efficiency, but a comparable camera integration time and excitation power as coverslip measurements could be used to obtain adequate photon rates for super-resolution imaging.

APPENDIX B

Exciton Generation Rate Calculations

The probability of generating an exciton in a NC is an important experimental condition to have knowledge about for comparing against excitation other studies, particularly when addressing charging, grey states, and multi-exciton generation. Many publications report this calculation in lieu of the power measurement because pulsed excitation and CW excitation result in different excitation conditions. Because both pulsed and CW sources were used in these studies, direct comparison is best addressed using the average excited state occupancy rate. The works of Yu *et al.*[177] and Leatherdale *et al.*[178] outline the procedure for determining the excitation cross section $\sigma(\lambda)$ for semiconductor NCs. Measurement of the absorption spectrum gives the extinction coefficient for the NCs studied here. From Beer's law

$$\epsilon(\lambda) = \frac{A(\lambda)}{cL}$$

where A is the absorbance, c the concentration of the fluorophores associated with the absorbance and L is the path length for the measurement. The single-molecule absorption cross section (in cm^2) for CdSe NCs is then given by[177]

$$\sigma(\lambda) = \frac{2303\ \epsilon(\lambda)}{N_\mathrm{A}}$$

where N_A is Avogadro's number. From the cross section, the average excited state occupancy rate is given by

$$k_\mathrm{ex} = \sigma(\lambda)\ j = \frac{\sigma(\lambda)\ I}{E(\lambda)}$$

where I is the excitation intensity and E is the photon energy.

B.1. 488 nm CW Excitation

From the absorption data shown in Figure 2.2, the extinction coefficient at 488 nm is

$$\epsilon_{488\text{ nm}} = \frac{0.0525}{(3.32 \times 10^{-6}\text{ mol})\,(0.1\text{ cm})} = 1.58 \times 10^{5}\text{ mol}^{-1} \cdot \text{cm}^{-1}$$

The absorption cross section at 488 nm follows as

$$\sigma_{488\text{ nm}} = \frac{2303 \times \left(1.58 \times 10^{5}\text{ mol}^{-1} \cdot \text{cm}^{-1}\right)}{6.022 \times 10^{23}\text{ mol}^{-1}} = 6.05 \times 10^{-16}\text{ cm}^{2}$$

Finally, the average excited state occupancy rate at the 488 nm CW excitation used for the SR experiments is

$$k_{\text{ex}} = \frac{(6.05 \times 10^{-16}\text{ cm}^{2})\left(185\text{ W/cm}^{2}\right)}{4.07 \times 10^{-19}\text{ J}} = 2.75 \times 10^{6}\text{ s}^{-1}$$

In CW excitation, this is often compared against the fluorescence lifetime of the exciton to determine the average excited state occupancy

$$\langle \text{N} \rangle_{488\text{ nm}} = \frac{k_{\text{ex}}}{k_{\text{rad}}} = \frac{2.75 \times 10^{6}\text{ s}^{-1}}{5 \times 10^{7}\text{ s}^{-1}} = 0.055$$

where the radiative lifetime of a cluster is the result of non-radiative and radiative decay processes and estimated to be ~ 20 ns given the FLID in Figure 5.1C. Hence, a NC cluster does not have a high probability of multiple excitons being generated within the lifetime of a single exciton given the excitation conditions of the SR experiments.

The extinction coefficient at 450 nm is

$$\epsilon_{450\text{ nm}} = \frac{0.1077}{(3.32 \times 10^{-6}\text{ mol})\,(0.1\text{ cm})} = 3.24 \times 10^{5}\text{ mol}^{-1} \cdot \text{cm}^{-1}$$

The absorption cross section at 450 nm follows as

$$\sigma_{450\text{ nm}} = \frac{2303 \times \left(3.24 \times 10^{5}\text{ mol}^{-1} \cdot \text{cm}^{-1}\right)}{6.022 \times 10^{23}\text{ mol}^{-1}} = 1.24 \times 10^{-15}\text{ cm}^{2}$$

which leads to the average excited state occupancy rate at the 450 nm pulsed excitation used for the time-resolved experiments

$$k_{\text{ex}} = \frac{(1.24 \times 10^{-15}\text{ cm}^{2})\left(5.89\text{ W/cm}^{2}\right)}{4.39 \times 10^{-19}\text{ J}} = 1.67 \times 10^{4}\text{ s}^{-1}$$

In pulsed excitation, the average excited state occupancy rate is typically compared against the repetition rate of the laser to give an average number of excitons generated per pulse

$$\langle \text{N} \rangle_{450\text{ nm}} = \frac{k_{\text{ex}}}{\text{rep. rate}} = \frac{1.67 \times 10^{4}\text{ s}^{-1}}{10^{6}\text{ pulses/s}} = 1.67 \times 10^{-3}\text{ excitons/pulse}$$

This indicates that a single NC in a cluster will, on average, not be excited by a pulse ($\langle \text{N} \rangle_{450\text{ nm}} \ll 1$) and, thus, a cluster with multiple NCs will still have a low probability of having multiple excitons given the excitation conditions of the time-resolved measurements, provided the cluster is relatively small.

APPENDIX C

Additional FLID and SID Examples

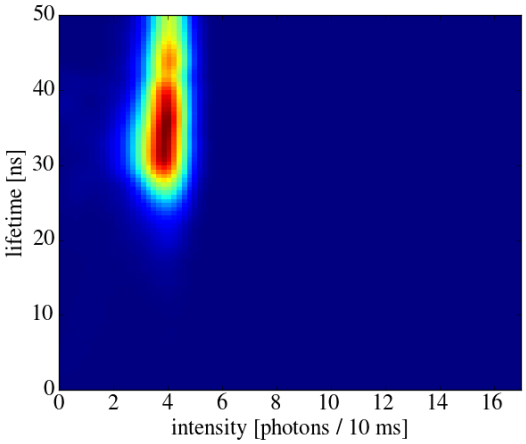

(A) Single NC #1

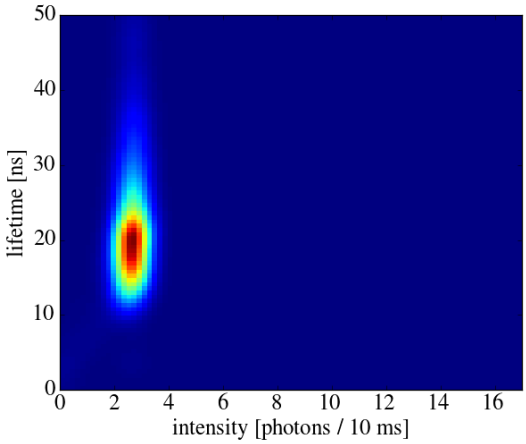

(B) Single NC #2

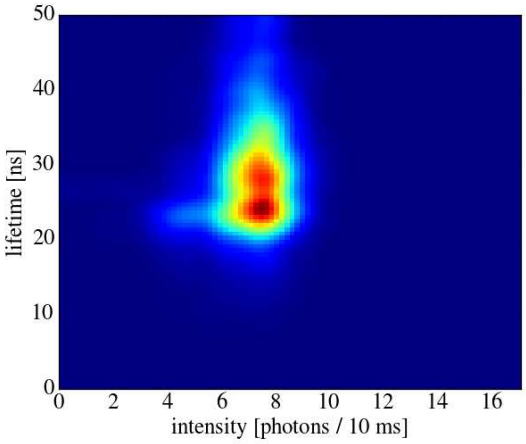

(C) Single NC #3

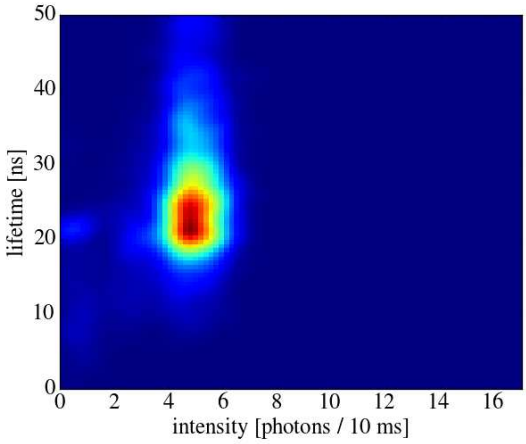

(D) Single NC #4

FIGURE C.1. Example FLIDs from several single NCs. Generally,individual NCs have a single lifetime associated with a single intensity level that corresponds to the on-state. The CdSe/ZnS NCs of this work typically had lifetimes of 20–30 ns and these example NCs show the degree of lifetime variation within a batch of NCs.

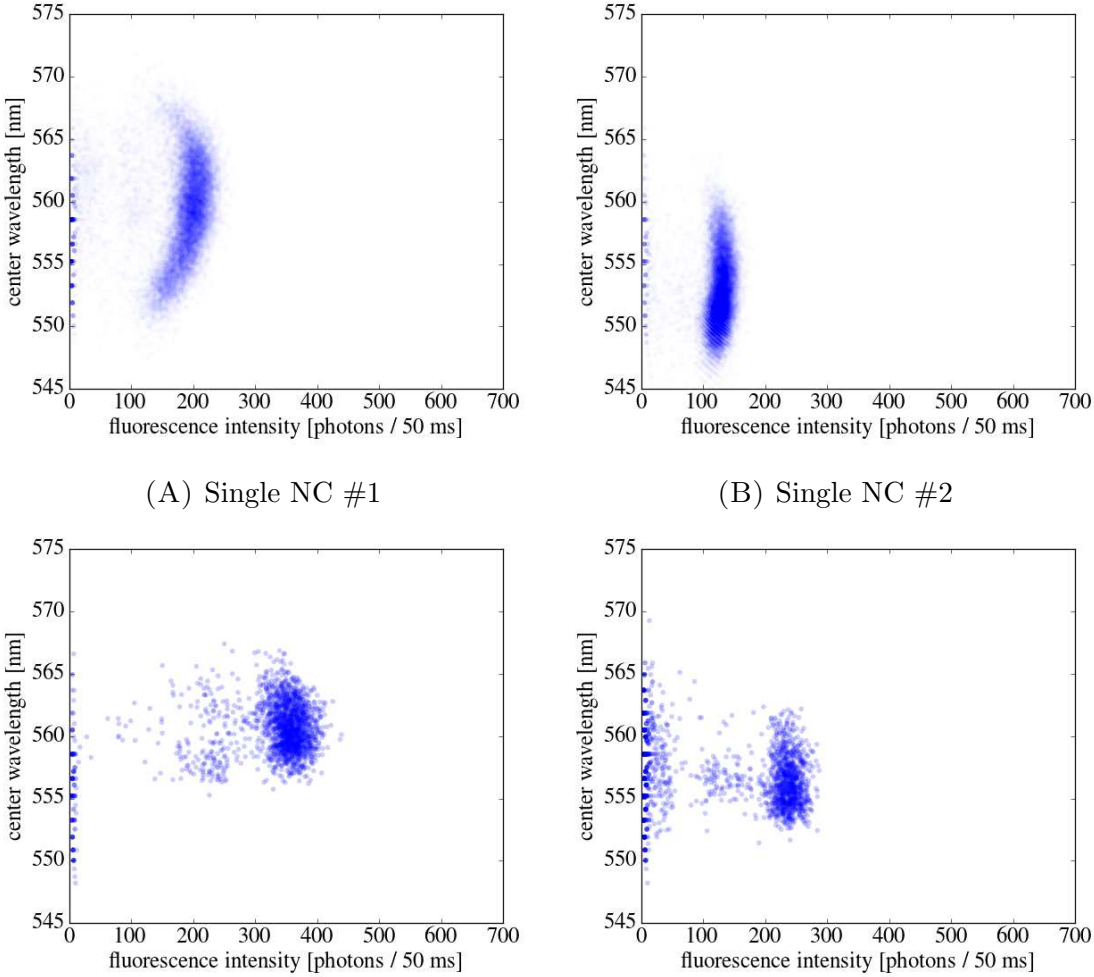

(A) Single NC #1

(B) Single NC #2

(C) Single NC #3

(D) Single NC #4

FIGURE C.2. SIDs corresponding to the same single NCs depicted in Figure C.1. Single NC SIDs typically have a single feature corresponding to their on-state intensity and center emission wavelength. Examples #1 and #2 exhibit a significant amount of spectral drift which is evident by the broadness of the single feature. NCs #3 and #4 were measured with a better microscope alignment, which is the reason for the higher intensities. Furthermore, they are the result of shorter measurement times compared to NCs #1 and #2, which can explain the smaller degree of spectral drift observed during the limited acquisition time. In #3 and #4, grey states clearly present additional features of intermediate intensities.

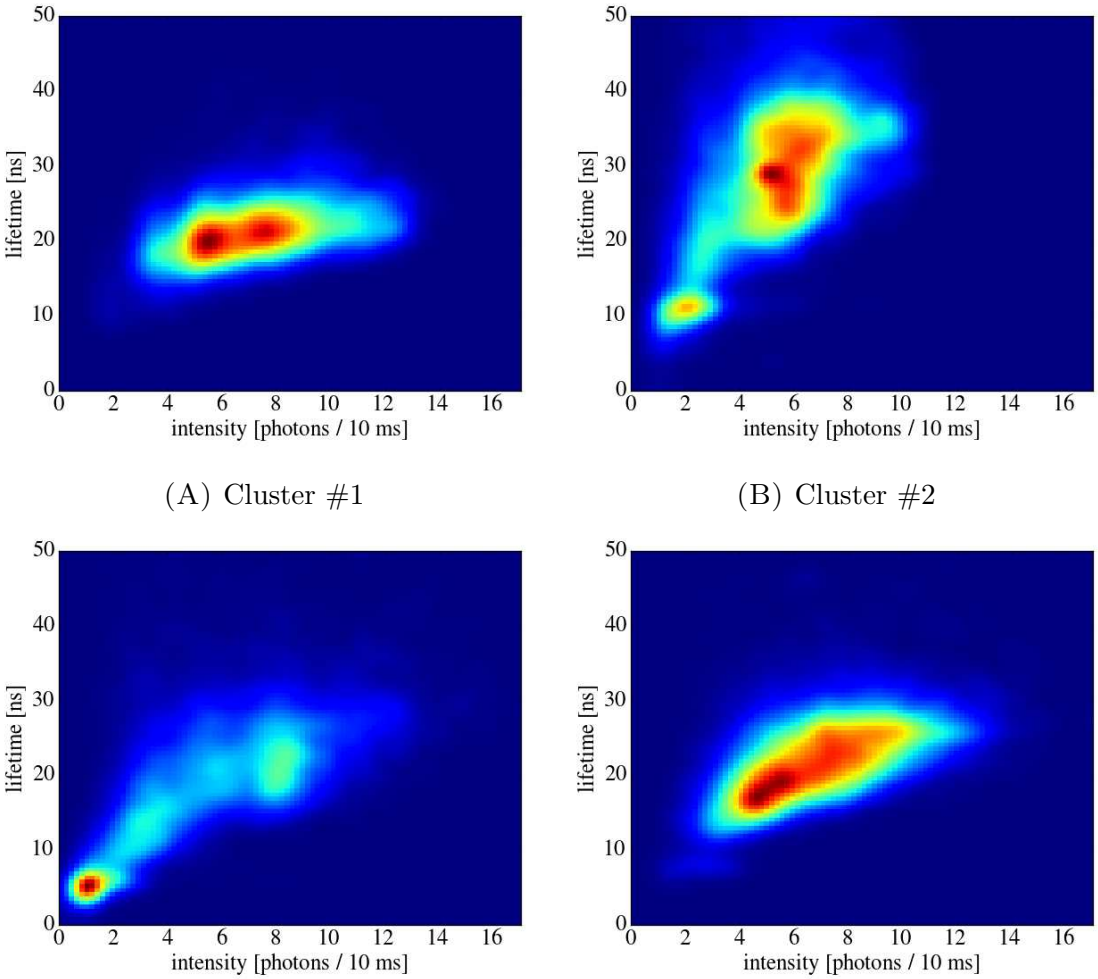

(A) Cluster #1

(B) Cluster #2

(C) Cluster #3

(D) Cluster #4

FIGURE C.3. Four example FLIDs demonstrating the variations observed between different NC clusters. All exhibit a lifetime-intensity relationship that indicates ET: shorter lifetime features corresponding to lower intensity that are due to donor emission.

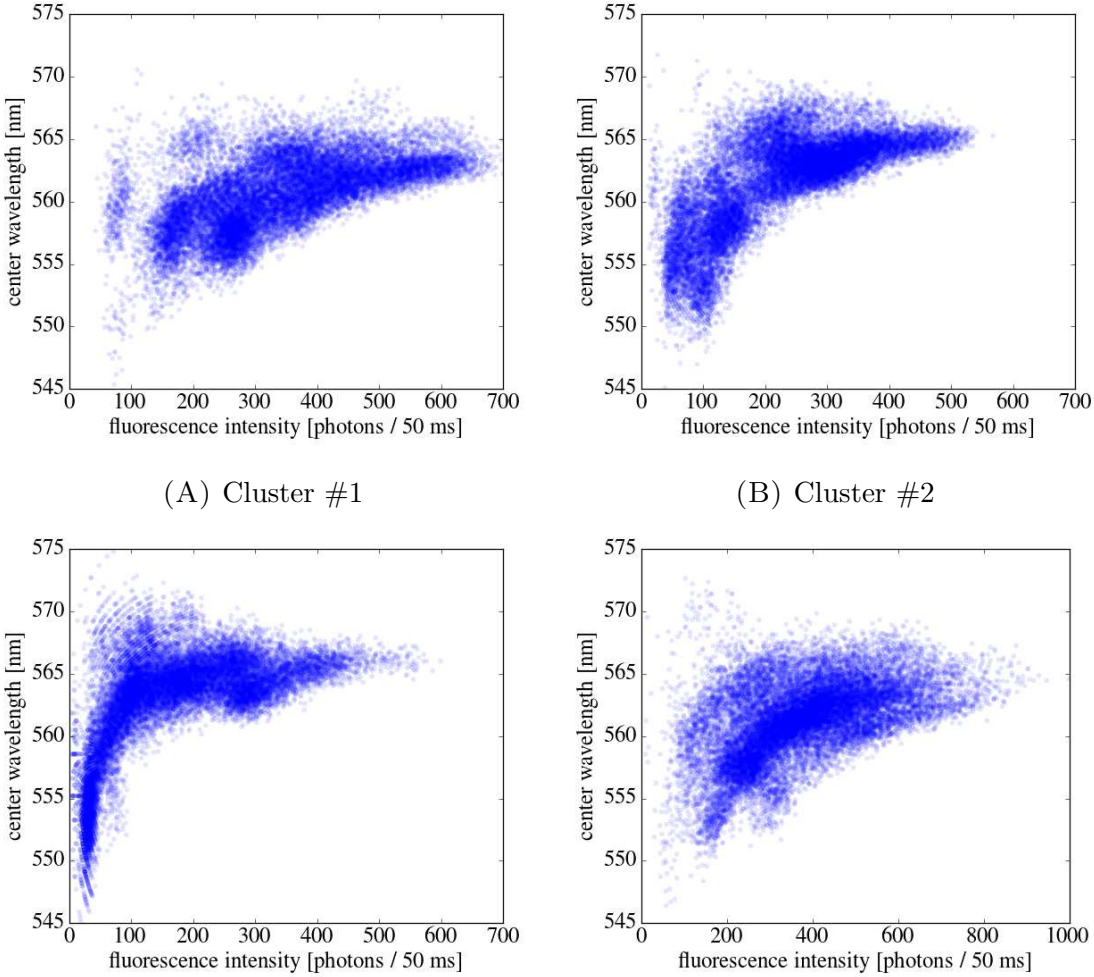

(A) Cluster #1

(B) Cluster #2

(C) Cluster #3

(D) Cluster #4

FIGURE C.4. SIDs that correspond to the same NC clusters in Figure C.3. From the FLIDs it is already known that these clusters demonstrate strong ET. These observations are further supported given the spectral signatures that show high intensity features corresponding to longer wavelength emission (from acceptor NCs) and low intensity features corresponding to shorter wavelength emission (from donors). The variation between SIDs indicates each NC cluster has unique spectral and lifetime signatures, emphasizing the need to perform single-molecule investigations.

APPENDIX D

Super-resolution Artifacts

Beyond the conditions a set of measurements are taken with, maximizing the SR localization accuracy is a factor of selecting an appropriate PSF model and noise model. The former depends on the imaging system and sample emission characteristics and the latter is determined primarily by the detection components. In the case of scientific CMOS cameras, some forms of instrument bias can be accommodated because the noise and response of every pixel is characterized independently (in CMOS detectors, each pixel has its own amplification circuit with unique characteristics). EMCCDs read out the information of each pixel through the same amplification register in a serial process and constructing a noise model is largely characterizing the gain and various noise sources for the device as a whole, which averages out senor defects or inhomogeneities. Hence, EMCCDs are less accommodating for some types of instrument response biases than sCMOSs.

PSF modeling can rectify some of the non-noise related IRF issues. The method DAOSTORM takes to perform SR fitting—tabulating experimentally determined correction factors to an analytical PSF—also provides a means to study the severity of dipole effects in the correlated experiment of Chapter 6 and justify the use of simpler SR tools that do not consider such effects. In the process that DAOSTORM characterizes the deviations, the algorithm compares PSFs of multiple stars in the field of view—to borrow the terminology of the astronomy software DAOPHOT on which DAOSTORM is based. It is assumed that each star in the field of view will share a common IRF effect (an assumption valid in astronomy) and by comparing the deviations from a fundamental Gaussian model between several stars, the shared IRF can be deconvolved from the image data with the influence of random noise

largely removed. This pre-processing step to SR localization is typically performed on a single representative frame. Because of dipole emission effects, each NC or NC cluster may have a unique fundamental PSF and this approach will average out those discrepancies as noise. Applying a set of residuals with these deviations averaged out to all stars in the field of view may bias localizations. However, a synthetic image can be constructed from multiple images of the same star over the duration of the experiment. Using this image as the source for characterizing the PSF and applying it to only the source star that generated it can accommodate unique dipole effects. It has been observed that NCs can undergo random rotations of the dipole orientation[166, 172]. While such rotations can occur, resulting in a different PSF shape, these rotations occupy small durations of the entire movie sequence and it is likely that the images sampled come from the primary dipole orientation, particularly when the PSFs appear similar by inspection.

Figure D.1 shows the residuals from two sample types: a single NC deposited onto a glass coverslip and imaged in ideal TIRF conditions (Figure D.1A) and a single NC, as determined through SEM imaging, that was deposited onto a SiN grid for correlation (Figure D.1B). In the coverslip example, a clearly asymmetric pattern is present and there are strong deviations from the Gaussian function that is the first approximation of the PSF. However, the SiN grid example is essentailly flat across the area of the fit. The noise due to the poorer imaging conditions for SiN grid samples is the primary source of deviations from the Gaussian PSF and they are appear random. If strong dipole effects were present in the correlated experiments that made use of SiN grids, these residuals would indicate so; no such effect is observed.

To further demonstrate the type of bias that can be brought about through dipole effects, we examine one type of artifact that presents in SR measurements done on glass coverslips.

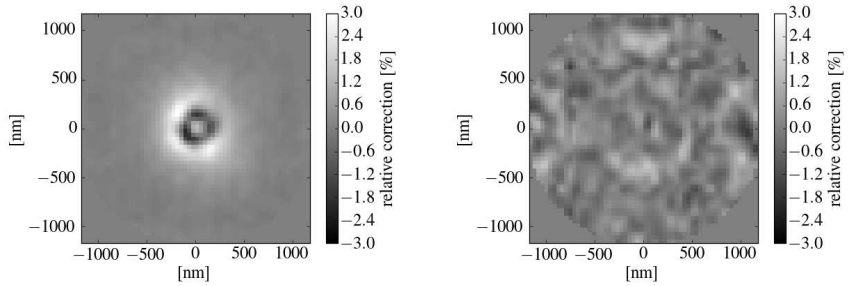

(A) Glass coverslip (B) SiN TEM grid

FIGURE D.1. Gaussian PSF residuals for NC on glass and on a TEM grid. DAOSTORM was used to compile the residuals from a single image that contained multiple images of the same NC from different times during the measurements.

Figure D.2 illustrates the halo effect that was observed for some particles. Halo features only appeared in DAOSTORM analyzed data sets because ThunderSTORM applies a symmetric analytical PSF, which introduces a different manifestation of the bias. The halo occurs for lower intensity frames where the SNR is small (blue circles in the scatter plot). Five regions are indicated by dashed boxes. Using frames from only one of the regions at a time, the residuals were determined from a synthetic image (as outlined above). Residuals from each of the five regions are shown next to the SR image. It is clear that residuals from regions (a) and (e) match each other, but residuals from regions (b) and (d) form a different matching pair. The former exhibit strong deviations in the upper left and lower right areas while the latter exhibit deviations in only the lower left areas. Residuals compiled from only the center region, (c), appear to be the sum of all the regions. These halo features are understood as the spontaneous changing of the emission dipole orientation in the NC. This may be another observation of the rotations Chen *et al.*[166] and Li *et al.*[172] reported (with the defocused imaging technique); however, these orientation jumps occur more frequently in our data and such artifacts are correlated with low intensity emission. Without SEM verification it is difficult to assess the size of the cluster, but it is possible the two halo features represent two

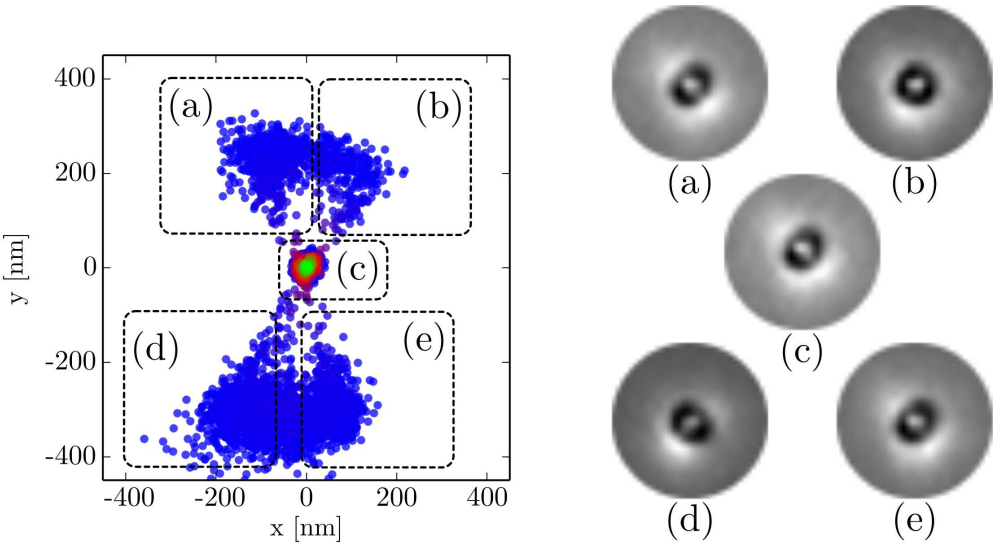

FIGURE D.2. DAOSTORM halo features. The residuals from regions (a) and (e) match while (b) and (d) form a different matching pair. The mirror symmetry of the residual pairs may be a result of the relative symmetry within each pair.

primary emitters—multiple acceptors registered as hot-spots if from an efficient ET cluster, or from two relatively non-interacting NCs—because of the number of unique residuals found in the halo regions. While the halo features from DAOSTORM are large, the manifestation of these artifacts in other SR algorithms can result in small features on the size of 5–25 nm, comparable to the localization shifts that are necessary to elucidate individual NCs within clusters, which is problematic if not recognized and addressed properly.

As a final verification that dipole effects are not present in the image data from the correlated experiments, several of the NCs and NC clusters were analyzed with a custom implementation of a dipole emission algorithm[120]. To fit image data from SiN grids, movies were cropped down to a single spot and fit to two 1D dipoles located at the same origin. Rather than impose a strict 2D formation pattern, treating each 1D dipole as a separate emitter orientation provides more degrees of freedom. Figure D.3 depicts the results of fitting a single NC and fitting a NC cluster. The representation of the results are explained in detail in Chapter 7. To construct the angle that defines the 2D emission plane, the

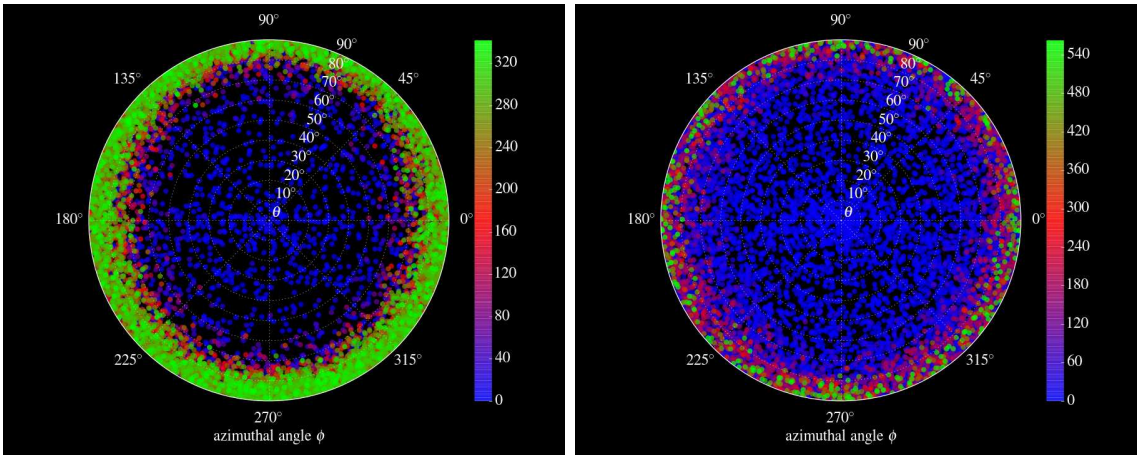

(A) Single NC (B) NC cluster

FIGURE D.3. Dipole orientation fitting of a single and cluster deposited on a SiN TEM grid.

orientation of the cross product of the two orientation vectors, each from one of the fitted 1D dipole terms, is used. The magnitude of the cross product also describes the eccentricity and degree of linear independence each dipole contributes. In all dipole fits of SiN grid data, the vectors were consistently perpendicular, so the illustration in Figure 7.1 is an accurate depiction of the constituent angles. In Figure D.3A, the dipole orientations present in the single NC are uniformly distributed in a ring, representing one 1D dipole oriented along the optical axis ($\theta = 0$) and the other taking on all rotations within a plane perpendicular to the imaging axis ($\theta = \pi/2$). This pattern was observed for all single NCs analyzed with dipole PSFs. Because all single NCs have the same presentation of orientation, none can be said to produce a PSF containing unique orientation information and SR biases originating from dipole effects are not expected. Furthermore, the orientations of a NC cluster, depicted in Figure D.3B, exhibit the exact same pattern. It appears that no orientation information can be obtained from data taken with SiN grids. The sources of localization bias that could be introduced by the asymmetries of dipole PSFs are absent.

List of Abbreviations

APD	avalanche photodiode
CP	change-point
CW	continuous wave (laser)
DET	Dexter energy transfer
EM	electron microscopy
ET	energy transfer
FLID	fluorescence lifetime-intensity distribution
FRET	Förster resonant energy transfer
FWHM	full width at half maximum
HAADF	high-angle annular dark-field imaging
hpc	hexagonal close packed (crystal structure)
ICA	independent component analysis
IRF	instrument response function
MLE	maximum likelihood estimation
NA	numerical aperture
NC	nanocrystal
PID	position-intensity distribution
PSF	point spread function
QD	quantum dot
QY	quantum yield
SEM	scanning electron microscope
STEM	scanning transmission electron microscopy

SID	spectral-intensity distribution
SNR	signal-to-noise ratio
SR	super-resolution
TEM	transmission electron microscopy
TIRF	total internal reflection microscopy
UC	ultra-centrifuge